University of Nevada, Reno

Application of Synthetic Aperture Radar Interferometry (InSAR) in Defining Groundwater-Withdrawal-Related Subsidence, Diamond Valley, Nevada

A thesis submitted in partial fulfillment of the
requirements for the degree of Master of Science in
Geological Engineering

By

Rei Arai

Dr. Robert J. Watters/Thesis Advisor

August, 2009

University of Nevada, Reno
Statewide • Worldwide

THE GRADUATE SCHOOL

We recommend that the thesis
prepared under our supervision by

REI ARAI

entitled

Application Of Synthetic Aperture Radar Interferometry (InSAR) In Defining Groundwater-Withdrawal-Related Subsidence, Diamond Valley, Nevada

be accepted in partial fulfillment of the
requirements for the degree of

MASTER OF SCIENCE

Robert J. Watters, Ph. D., Advisor

John W. Bell, Committee Member

Jaak J.K. Daemen, Ph. D., Graduate School Representative

Marsha H. Read, Ph. D., Associate Dean, Graduate School

August, 2009

Abstract

Interferometric Synthetic Aperture Rader (InSAR) technique has been recently used in detecting and monitoring ground displacements such as volcanic activities, earthquakes, landslides and surface deformations caused by fluid extraction. Ground subsidence related to groundwater withdrawal has occurred in many places such as urban areas and large scale agricultural areas. This study utilizes interferometry to detect ground subsidence in an agricultural field, where a large volume of groundwater has been pumped for decades, in Diamond Valley, Nevada. InSAR has proven to have great potential to detect and quantify ground subsidence caused by aquifer system compaction. It mapped ground deformation signals with high spatial detail and resolution of displacement, developed in a groundwater basin in the area, using radar data collected from the ERS-1/ERS-2 and Envisat satellites. The subsidence signal at the south part of the valley, where irrigation wells exist, shows a minimum of 37.6 cm of cumulative subsidence between July 17, 1992 and November 27, 1999 and a 17.5 cm of cumulative subsidence between October 16, 2004 and December 15, 2007.

The profile views of the subsidence signals assist in visualizing the deformation geometry which indicates that the subsurface lithology can increase or decrease the deformation. The subsurface model estimated from the history of water table decline and the subsurface lithology distribution approximately correlate with the subsidence signals. Poor correlation occurred where limited availability of good subsurface data and limited spatial coverage of well logs existed.

Acknowledgement

It is a pleasure to thank all those who gave me the possibility to complete this thesis. First, I would like to thank the member of my committee.

To my advisor, Bob Watters, with his enthusiasm, his inspiration, and his great efforts to explain things clearly and simply, he helped to make geological engineering interesting for me. Throughout my thesis-writing period, he provided encouragement with his bottomless positive attitude, sound advice, good teaching, and good grammar fix. I would have been lost without him.

To John Bell, I would like to thank the opportunity he gave me to work as an assistant of your InSAR projects. It provided me lots of radar remote sensing knowledge and interests, and made me successfully achieved my goal, this thesis project.

To Jaak Daemen, from his rock mechanics class I learned the principles and the nature of dealing with natural materials, and it would be fundamental to my career. It was valuable that I had his lectures learning his extensive knowledge of rock mechanics.

I also thank the General Moly, Inc. for having me working as a part of their project and their willingness to share data. This study would not have been possible without their support.

To all my friends I made here in school, I will not forget the times that we have shared together. Especially, to Asako, a person who has the same love towards rocks as I do and speaks Japanese, I cannot thank you enough here in English but four years of school with you were extremely cheerful and valuable.

Lastly, and most importantly, I wish to thank my family, especially my parents, for their continuous support, and understanding what I am willing to do. To them I dedicate this thesis.

Table of Contents

List of Tables

List of Figures

Chapter 1

Introduction

The vertical ground movements of subsidence, collapse, and heave are often the results of human activities that change the natural environment. Natural occurrences, such as earthquakes and tectonic movements, also cause surface displacements. The Interferometric Synthetic Aperture Rader (InSAR) technique has been recently used in detecting and monitoring ground displacements such as volcanic activity (Massonnet et al., 1995), earthquakes (Massonnet et al., 1993 and Ozawa et al., 1997), landslides (Burgmann, 2006; Signghroy, 1998 and 2004) and surface deformations caused by fluid extraction (Bell, et al., 2002; Raucoules, et al., 2007; Weeks, et al.). Ground subsidence has been recognized as a geologic hazard though less disastrous than either slope failures or earthquakes in terms of lives lost, but results in total property damage that each year probably exceeds that of all other hazards (Hunt, 2007).

In order to conduct an effective risk management, monitoring techniques are required to better understand of ground deformation phenomena and their possible causes. Important tasks of this study include: detection of ground deformation, where and when subsidence occurred or is occurring, assessment of the deformation, and the evolution (past and future) of the deformation.

1.1 Ground Subsidence

Ground subsidence can occur as a natural phenomenon such as naturally generated compaction and dissolution of limestone aquifers (sinkholes), as well as anthropogenic phenomenon such as aquifer-system compaction (extraction of fluids), drainage or oxidation of organic soils, and underground mining (excavated subsurface cavities) (Leake, 2004).

The most common cause of ground subsidence in almost every part of the world is caused by the withdrawal of large volumes of groundwater. Documented locations include areas near San Jose, California; Phoenix, Arizona; Houston, Texas; and Las Vegas, Nevada (Figure 1.1), as well as Mexico City, Venice and London.

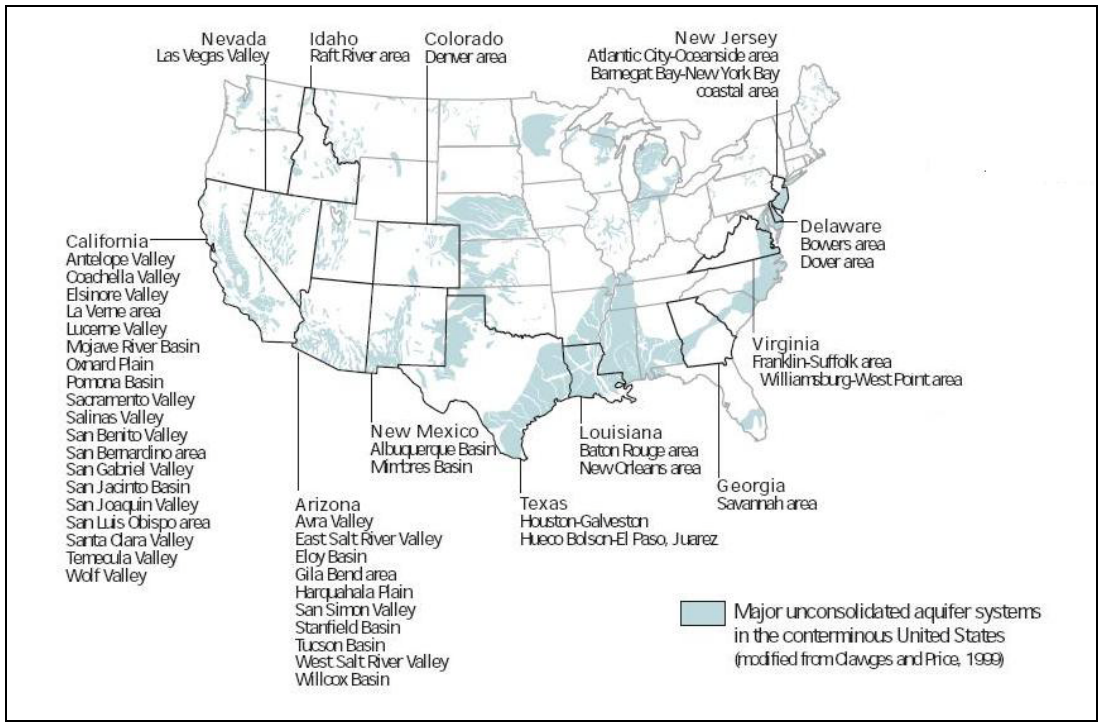

Figure 1.1 Areas where subsidence has been attributed to the compaction of aquifer systems caused by groundwater withdrawal. (modified from Galloway et al, 1999)

1.1.1 Examples of Ground Subsidence due to Groundwater Pumping

Santa Clara Valley, California. The city of San Jose has subsided about 4 m (14 ft.) since 1910 with the majority of that occurring before 1969 when groundwater regulations were put in place (Galloway et al, 1999 and Poland and Ireland, 1988). Intense groundwater pumping over long periods resulted in a lowering of the local groundwater table by approximately 60 m (200 ft.). Figure 1.2 shows water table and subsidence records for a well in San Jose between 1912 and 1967. The damages including buckling of water-well castings, lost capacity of sanitary and storm drainage sewers as a result of change in the natural slope, and flooding of roads, railroads, and developed areas from the San Francisco Bay, which required construction of levees and other protective works. The overall damages in Santa Clara were estimated at $100 million (Fowler, 1981).

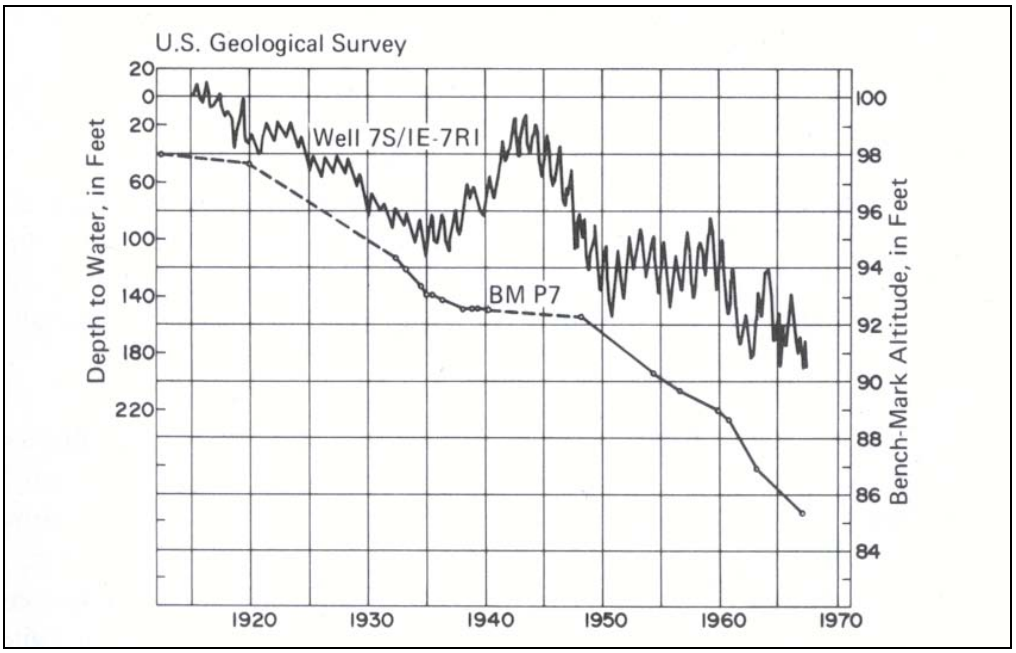

Figure 1.2 Ground subsidence data for San Jose, California between 1912 and 1967 (Poland, 1981).

Las Vegas Valley, Nevada. Due to heavy groundwater pumping in order to supply the demand for the fast growing city of Las Vegas, the area has experienced ground subsidence, and was recognized in 1948 by Maxey and Jameson. According to Bell (1981) the annual groundwater withdrawals, as the city rapidly was growing, reached approximately 111 cubic hectometer/yr. The groundwater level decline of the area in the northwest part of the valley was estimated as much as 90 m (300 ft.) (Burbey, 1995). Three major subsidence bowls were identified and delineated by Bell and Price (1991) and the largest subsidence was delineated as 1.7 m as of 2000 from GPS and InSAR data (Bell et al, 2008).

Other ground subsidence examples include; *Houston, Texas* where a decline in the water table of about 90 m since 1906 has caused as much as 1.5 m of subsidence with serious surface effects; *Phoenix, Arizona* where approximately 310 km^2 of land southeast of the city has subsided more than 3 m between 1952 and 1979; *San Joaquin Valley, California* where at least 11.000 km^2 of the agricultural area has subsided, an area 113 km long has subsided more than 3 m with a maximum of 8.5 m (Rahn, 1996).

1.1.2 Damages Caused by Ground Subsidence

Since causes of ground subsidence are mostly human activities, a change in land surface triggers many problems (as discussed in examples in the previous section). Typically problems occurring from subsidence include (1) changes in elevation and slope of streams, canals, and drains; (2) damage to bridges, roads, railroads, storm drains, sewer pipes, canals, and levees; (3) damage to private and public buildings; and (4) failure of well casings from forces generated by compaction of fine-grained materials in

aquifer systems. In some coastal areas, subsidence has resulted in tides moving into low-lands that were previously above high-tide levels (Galloway et al., 1999).

1.2 Groundwater Usage in Diamond Valley, Nevada

Water levels in the Diamond Valley have changed over time as a result of groundwater withdrawals for irrigation. According to Arteaga et al. (1995), the irrigated area expanded from 3,200 acres in 1961 to 22,200 acres in 1990. In the early development, Harrill (1968) estimated total pumpage to be 12,000 acre-ft in 1965 and 50,000 acre-ft for 1950–65. Between 1972 and 1990, annual pumpage of ground water for irrigation increased from 23,000 to 64,000 acre-ft (Arteaga et al, 1995). The total annual groundwater extraction has been measured from 1965 to present and the average pumpage for the last couple of decades is approximately 70,000 acre-feet/year (Figure 1.3).

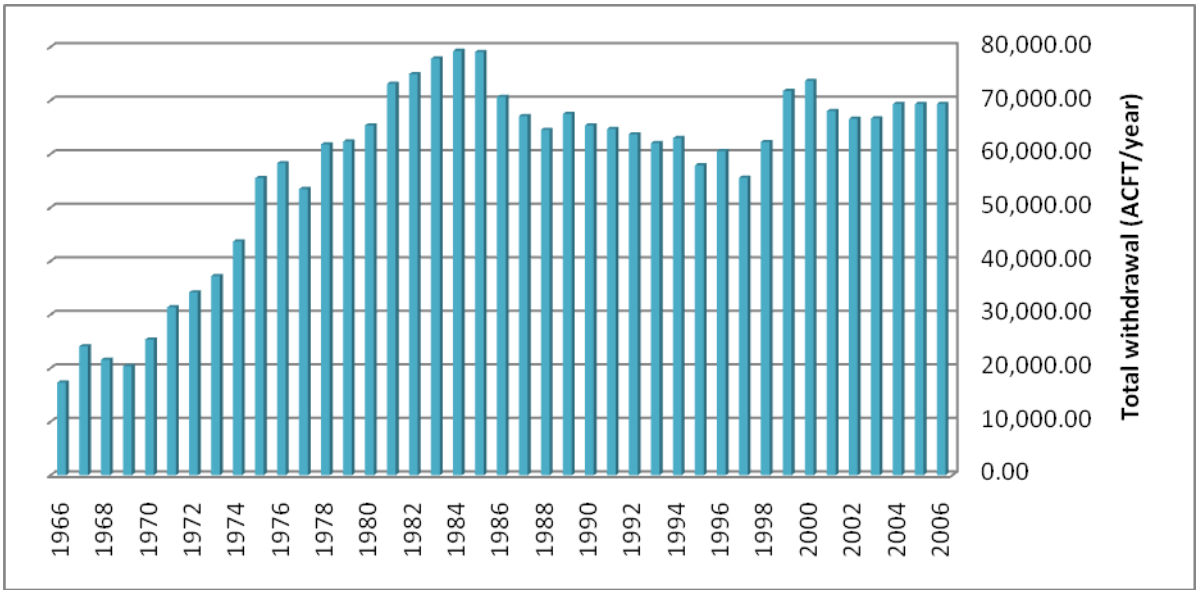

Figure 1.3 Groundwater extraction history from 1965 to 2006 of irrigation wells in the southern Diamond Valley.

1.3 Methods for Detecting Ground Surface Displacements

The Global Positioning System (GPS) and optical leveling are two field techniques that have been widely used with high accuracy for ground deformation detection and measurement. Compared to the optical leveling the use of GPS makes it possible to perform subsidence monitoring much more efficiently and at reduced costs by revisiting ground-based benchmarks. However, these two methods only measure the surface deformation at a small scale and at a few locations. Therefore, it is very difficult to measure a wide-area or assess regional coverage without increasing a high cost.

The Interferometric Synthetic Aperture Rader (InSAR) technique is based on the comparison of the radar phases of two SAR images acquired at two different times and was first applied as a scientific tool in 1974 using data supplied by the first civilian remote sensing satellite, Seasat. In the early 1990's the European Space Agency (ESA) launched ERS-1 satellite and the more widespread application of InSAR data began to evolve. This rapid-spreading movement was followed by the launchings of ERS-2, a Japanese prototype (JERS-1), the Canadian Radarsat, and ESA's Envisat.

Detecting ground subsidence is one of the most recent applications of InSAR. The technique provides very high resolution and precise measurements and allows regional scale monitoring and mapping. Historical assessment of deformation by using the existing SAR image archives, dates back to the beginning of 1992 for the ERS-1/ERS-2 satellite sensors (detailed discussions in Chapter 5). InSAR analysis allowed the identification of not only the complex aerial extent but also the deformation magnitude

and possible assessment for quantification of the relationship between groundwater withdrawal and the ground deformation at a very high spatial resolution.

1.4 Background of the Study

The major part of this study is the development of a detailed InSAR time-series delineating on-going aquifer subsidence in Diamond Valley. This InSAR study was conducted as a part of hydrogeologic research in the Diamond-Kobeh Valley area (Bell, 2009), conducted a research contract with General Moly, Inc. The scope of this hydrogeologic research was to evaluate the future potential for land subsidence due to groundwater pumping associated with the proposed Mount Hope project in Kobeh Valley. The complete InSAR results of Diamond Valley was utilized to estimate hydraulic storage coefficients to model aquifer-system response in Kobeh Valley, where the hydrogeologic characteristics is very similar to that of Diamond Valley, for long-term heavy groundwater pumping.

1.5 Objective of the Study

This study utilizes the InSAR technique to detect the ground subsidence signals from the Diamond Valley in east-central Nevada where groundwater has been heavily used for agriculture for a long time. The InSAR identified deformation signals are unique because most signals are observed in an area far from the heavy pumping irrigation area in the very south of the valley. The aerial extent and the magnitude of deformation were also successfully delineated with time. The spatially and temporally high resolution image by InSAR technique allowed the mechanism of aquifer compaction due to

groundwater withdrawal to be studied by correlating subsurface geology (mostly lithologic distribution) and the water table change over the pumping history.

The objective of this study includes:

- Determination of the aerial extent and the magnitude of the ground deformation with time by using the InSAR technique.
- Determination of the water table drawdown history and the subsurface lithology.
- The correlation between the alluvial compaction observed and the subsurface conditions including stress transfer due to the water table decline and the aquitard distribution within the aquifer.

Chapter 2

Description of Study Area

This chapter will provide a brief description of the study area, including site location, climate, generalized geology from previous works, and the anthropogenic history.

2.1 Location and Physiography

Diamond Valley is an intermountain valley and is part of the Great Basin physiographic province in east-central Nevada. The valley is elongated from north to south and is about 50 miles long and 15 miles wide at its widest and lies within an area bounded by lat 39°27’ and 40°15’ N. and long 115°47’ and 116°12 W. The valley is bounded on the east by the Diamond Mountains and on the west by the Sulphur Spring Range, Whistler Mountains and the Mountain Boy Range (Figure 2.1). The southern boundary is formed by the Fish Creek Range and the northern boundary by the Diamond Hills. These surface boundaries form a closed basin except for Devil’s Gate, which permits surface and subsurface inflow from Antelope, Kobeh, and Monitor Valleys.

The lowest part of Diamond Valley, altitude about 1,759 m, is a playa which covers most of the northern part of the valley floor. The highest part of the valley is 1,890 m at the south end, where the valley floor rises southward from the playa at a gradient of about 9 feet per mile. The highest elevations above 2,743 m are found only in the Fish Creek Range and Diamond Mountains. The highest point is South Diamond Peak in the Diamond Mountain at an altitude of 3,235 m (Harrill, 1968).

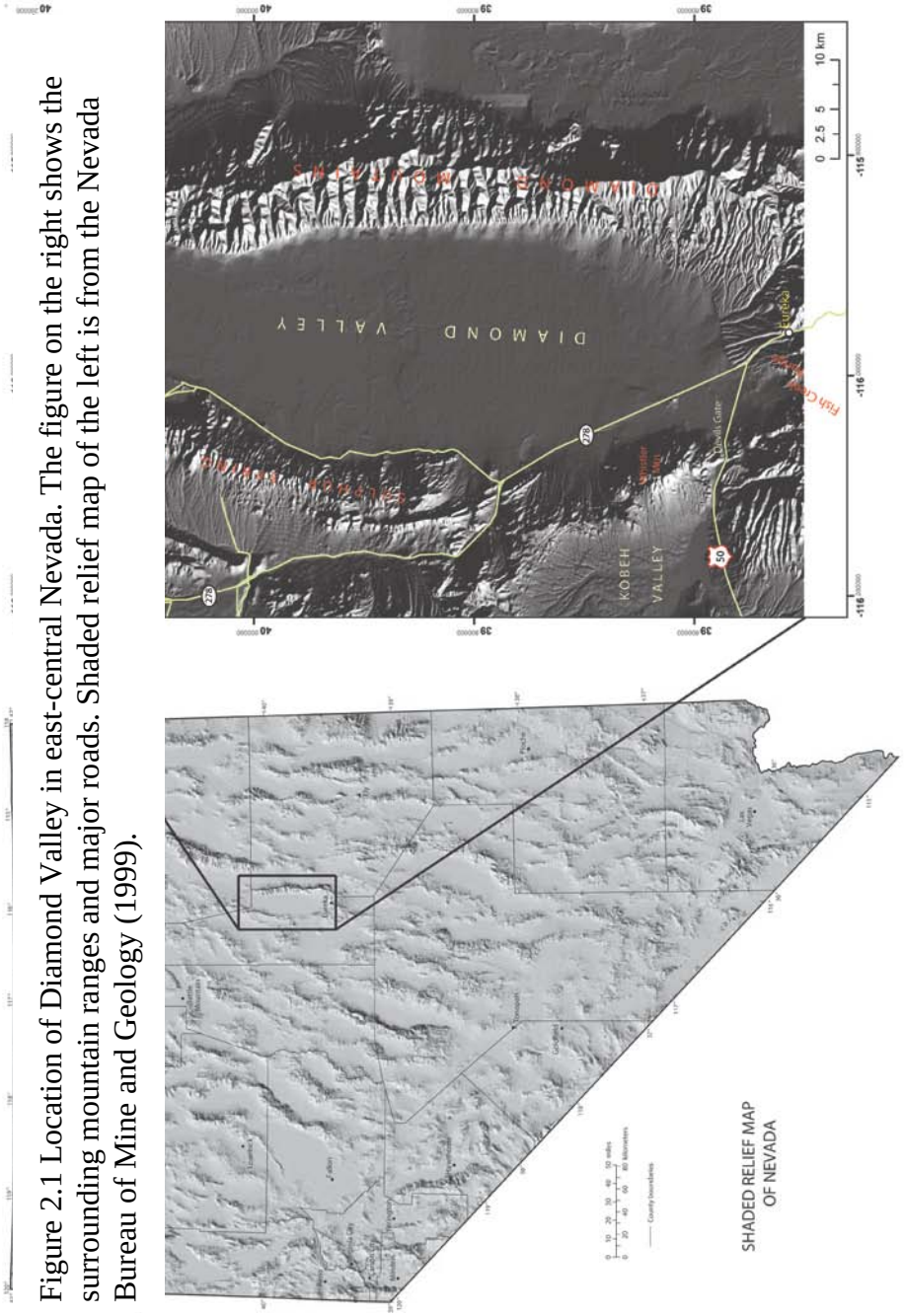

Figure 2.1 Location of Diamond Valley in east-central Nevada. The figure on the right shows the surrounding mountain ranges and major roads. Shaded relief map of the left is from the Nevada Bureau of Mine and Geology (1999).

The climate in Diamond Valley is similar to that of most valleys in east-central Nevada. Areas at low elevations commonly receive less moisture than areas at higher elevations. This results in semiarid conditions in the valley and sub-humid conditions in the surrounding mountains (Harrill, 1968). The mid-latitude steppe zone is semiarid, with warm to hot summers and cold winters. The sub-humid continental zone has cool to mild summers and cold winters with annual precipitation occurring mostly as snow (Houghton et.al, 1975). Most precipitation in the area comes from regional snow storms during winter. During the summer season thunderstorms can produce large amounts of precipitation as rain in a short time at high intensity. Average annual precipitation from the Diamond Valley weather station is 25 cm. and annual precipitation totals have ranged from 12 cm. to more than 38 cm. Average annual precipitation at the Eureka station is approximately 30 cm. and annual precipitation ranged from 18 cm. to 58 cm. (Tumbusch and Plume, 2006).

2.2 Generalized Geology

2.2.1 Physiographic Descriptions

The landforms in Diamond Valley are typical of those which occur in the Great Basin. The valley is a structural depression which is partly filled by unconsolidated and semi-consolidated sub-areal and lacustrine deposits (Harrill, 1968). Harrill (1968) describes that the valley can be divided into three parts based on physiographic features; the mountains, the alluvial fans, and the playa. The alluvial fans and playa form the valley floor.

The mountains that border Diamond Valley are principally composed of heavily faulted and folded Paleozoic sedimentary rocks. The overall shape and size of the mountains is the result of regional uplifting and down-dropping associated with normal faulting, and are generally deeply dissected, with prominent fault scarps and ridges formed by relatively resistant beds. Areas underlain by volcanic rocks typically have smooth convex upper surfaces and steep slopes.

The alluvial fan is an area of intermediate slope between the mountains and the flat playa in the valley floor. According to Harrill (1968) the slopes on the alluvial fan deposits decrease from about 100 feet per mile near the mountain fronts to only a few feet per mile near the playa. Local relief may be as much as 25 feet, as a result of stream erosion on the higher slopes, and bars, spits and beach deposits are formed on the intermediate and lower slopes.

In the northern part of the valley floor playa covers an area of approximately 50,000 acres. Fine-grained wind-eroded material from the playa and lower slopes of the alluvial fans form low profile dunes locally along the margins of the playa (Harrill, 1968).

2.2.2 Principal Lithologic Units

Lithologic units, ranging from Paleozoic carbonate rocks, quartzites, shales, sandstones, and conglomerates comprise the mountain ranges and structural basins with Tertiary and Quaternary basin-fill deposits. These rocks and deposits were grouped into five hydrogeologic units by Tumbusch and Plume (2006) based on lithology, which affects the permeability and water-bearing properties of the units. The five units are (1) carbonate rocks consisting of limestones and dolomites of Middle Cambrian to Devonian

age and of Pennsylvanian age, (2) siliciclastic sedimentary rocks consisting of shales, siltstones, sandstones, and conglomerates of Upper Cambrian to Cretaceous age, (3) igneous intrusive rocks of Jurassic, Cretaceous and Tertiary age, (4) volcanic rocks of Tertiary age, and (5) basin-fill deposits of Tertiary and Quaternary age. Lehner and others (1961) identified three types of Quaternary alluvial deposits: (1) older alluvium as alluvial fans along basin margins, (2) younger alluvium in basin and low lands, and (3) playa deposits. Principal lithologic units and distribution of the units are summarized in Table 2.1, which was compiled from the work of Lehner and others (1961), Harrill (1968), and Tumbusch and Plume (2006) and is shown on Figure 2.2.

Table 2.1 Lithology, thickness, locality, and general hydrologic properties of principal hydrogeologic units in Diamond Valley. Data from Lehner and others (1961), Harrill (1968), and Tumbusch and Plume (2006).

Geologic age and thickness	Lithology and geologic formation	Occurrence	General hydrologic properties
Playa Deposits			
Quaternary: Pleistocene and Recent 0 - 100± feet	Silt, clay, and evaporates. Includes some dune sand.	Occurs beneath playa in north-central diamond Valley	High interstitial porosity and low permeability.
Younger Alluvial Deposits			
Quaternary: Pleistocene and Recent 0 - 200± feet	Unconsolidated alluvial and colluvial deposits of interbedded sand, gravel, silt and clay. Materials generally moderately to well sorted and form lenticular bodies.	Occurs primarily as Lake Diamond and associated deposits. Includes some slope wash, flood-plain, and channel deposits formed during and after the lake receded. Fine-grained, lake-bottom deposits predominate near the center of the valley; coarse-grained beach-gravel and bar deposits predominate along edges and southern end of the valley.	Sand and gravel deposits highly permeable and capable of yielding large quantities of water to wells. Buried beach gravels are the highest yielding deposits of the valley fill. Lake-bottom deposits of fine-grained sand, silt, and clay are less capable of yielding water to wells.
Older Alluvial Deposits			
Quaternary: Pleistocene 0 - 1500± feet consolidated materials (the maximum of 7,500 feet near the axis of the valley)	Alluvial and colluvial deposits of sand, gravel, silt and clay. Materials range from well sorted to poorly sorted. Partially consolidated (cemented in localized areas and at depth. Deposits at depth in the center of the valley generally moderately to well sorted.	Occurs principally as alluvial fan deposits, also slope wash, talus deposits, upland alluvial surfaces, and high-level shore-line deposits. Locally includes some surficial recent alluvilal fan deposits and channel deposits. Fan deposits locally have been uplifted, faulted, dissected by erosion, and marked by shore-line features of various lake stages. Occurs at depth in the center of the valley as lake deposits with overlie valley-fill deposits of Tertiary age.	Permeability ranges from low to high. Zone of high permeability generally associated with buried channel deposits.

Table 2.1 continued.

Geologic age and thickness	Lithology and geologic formation	Occurrence	General hydrologic properties
	Volcanic Rocks		
Tertiary 0 - 700+ feet exposed. ~6,300 feet in subsurface	Ash-flow and air-fall tuffs of rhyolitic composition. Lava flows and shallow intrusive of rhyolitic and andesitic composition. Basaltic lave flows.	Northeast end of Fish Creek range, northeast flank Sulphur Spring range, Table Mountain. Greatest thickness probably preserved in basins beneath and interbedded with older basin-fill deposits.	Mostly impede ground-water flow because tuffs weather to clay and because of interbedded fine-grained lake deposits. May transmit small amounts of water through joints and zones between flows.
	Igneous Intrusive Rocks		
Tertiary, Cretaceous, and Jurassic Extend to great depths	Mostly quartz monzonite, granodiorite, and mafic dikes.	Exposed at Whistler Mountain on the southwest side of the valley and in the southern Fish Creek Range.	No interstitial porosity and permeability; may transmit small amounts of water trough near-surface fractures and weathered zones.
	Siliciclastic Sedimentary Rocks		
Cretaceous to Cambrian 9,000± feet	Primarily sandstone, quartzite, shale, of conglomerate. Includes: Newark Canyon Formation, Garden Valley Formation, Carbon Ridge Formation, Diamond Peak Formation, Chainman Shale, Pilot Shale, Eureka Quartzite, Vinini Formation, Dunderberg Shale, Secret Canyon Shale, Pioche Shale, Prospect Mountain Quartzite.	Exposed in parts of the Diamond Mountains, Fish Creek Range, Mountain Boy Range, Sulphur Springs Range, and Roberts Mountains.	Do not readily transmit water, except in areas of intense structural deformation where some water may be transmitted along fractures.

Table 2.1 continued.

Geologic age and thickness	Lithology and geologic formation	Occurrence	General hydrologic properties
Pennsylvanian to Cambrian 22,000± feet	Primarily limestone or dolomite with some interbedded sand and shale. Includes: Ely limestone, Joana Limestone, Devils Gate Limestone, Nevada Formation, Lone Mountain Formation, Hanson Creek Formation, Pogonip Group, Windfall Formation, Hamburg Dolomite Geddes Limestone, Eldorado Dolomite	Principal exposures in Sulphur Springs Range, Fish Creek Range, Mountain Boy Range, and west flank Diamond Mountains.	Comprise carbonate-rock aquifers generally beneath basin-fill aquifers. High permeability due to solution openings and fracture zones.

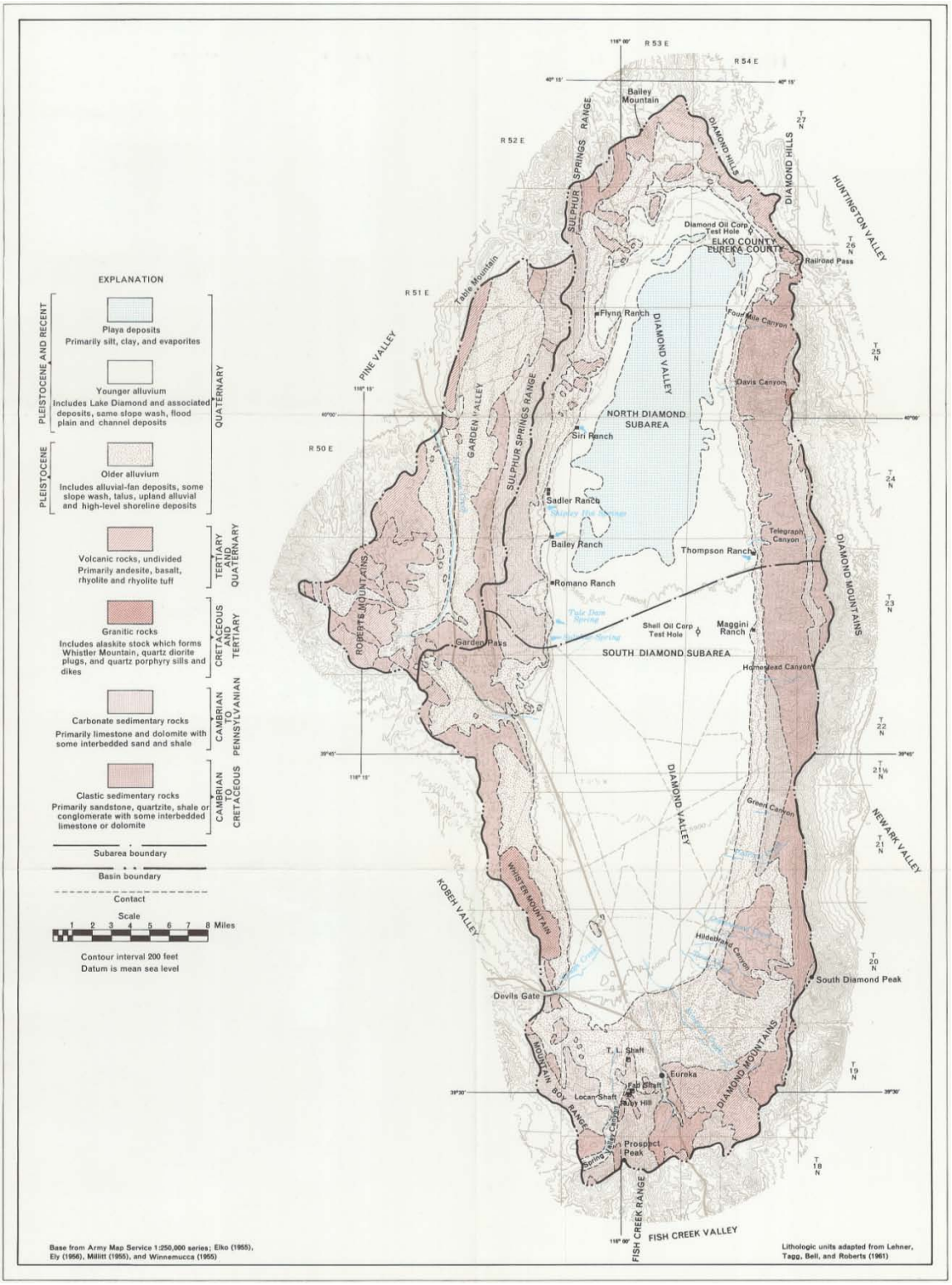

Figure 2.2 Map of distribution of principal lithologic units, subareas, and geographic features, Diamond Valley, Nevada. (Harrill, 1968)

2.2.3 Subsurface Geology of the Basin-Fill Deposits

Thickness of basin-fill deposits range from a few tens of feet near basin margins to thousands of feet in the deepest parts of the basins of Diamond Valley. Six oil exploration wells have been drilled—two in the central part and four in the southern part (Figure 2.3). Wells #1 and #2 are near the axis of the valley where the thickness of basin-fill deposits is 1,070 and 7,500 ft, respectively, and four wells from #3 to #6 were drilled closed to each other in the central and eastern parts of the valley where the thickness of the basin-fill deposits ranges from 1,070 to 4,250 ft (Figure 2.4).

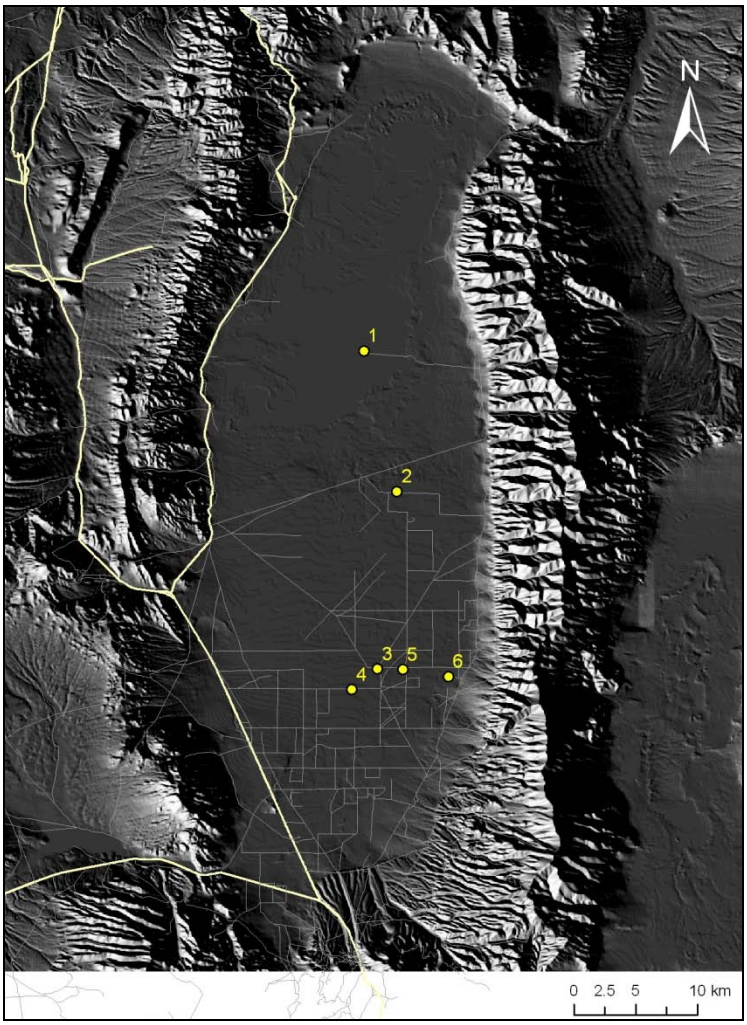

Figure 2.3 Map showing the location of the oil exploration wells.

Well number (fig. 1)	American Petroleum Institute Number	Altitude (feet)	Total depth (feet)	Depth (feet)	Unit	Thickness (feet)	Latitude (degrees, minutes, seconds)	Longitude (degrees, minutes, seconds)
					Diamond Valley			
1	27-011-05206	5,780	8,900	0	Basin-fill deposits	1,070	395711	1155724
				1,070	Volcanic rocks	6,285		
				7,355	Carbonate rocks			
2	27-011-05056	5,800	8,042	0	Basin-fill deposits	7,500	395102	1155557
				7,500	Carbonate rocks			
3	27-011-05204	5,881	10,600	0	Basin-fill deposits	1,070	394316	1155648
				1,070	Volcanic rocks	6,285		
				7,355	Carbonate rocks			
4	27-011-05224	5,880	6,552	0	Basin-fill deposits	2,248	394222	1155756
				2,248	Volcanic rocks	2,132		
				4,380	Clastic sedimentary rocks	1,830		
				6,210	Carbonate rocks			
5	27-011-05251	5,893	8,600	0	Basin-fill deposits	4,242	394314	1155542
				4,242	Volcanic rocks	530		
				4,773	Carbonate rocks			
6	27-011-05287	5,900	4,055	0	Basin-fill deposits	3,850	394256	1155342
				3,850	Carbonate rocks			

Figure 2.4 Hydrogeologic units penetrated by six oil exploration wells in Diamond Valley. Modified from Tumbusch and Plume (2006).

The lithology and hydrologic properties of basin-fill deposits in the valley (Harrill, 1968), include an estimation of the thickness of deposits in various areas using gravity data (Mabey, 1964) and information from an oil-test well log (Well #2, drilled in 1959). Harrill used water well driller's logs to estimate the distribution of sand, gravel, and finer-grained materials such as silt and clay for the upper 100 feet of saturated materials. He analyzed the water well logs of 117 wells selected on the basis of their location and clarity and developed a map showing the subsurface distribution of sand and gravel in southern part of the valley (Figure 2.5).

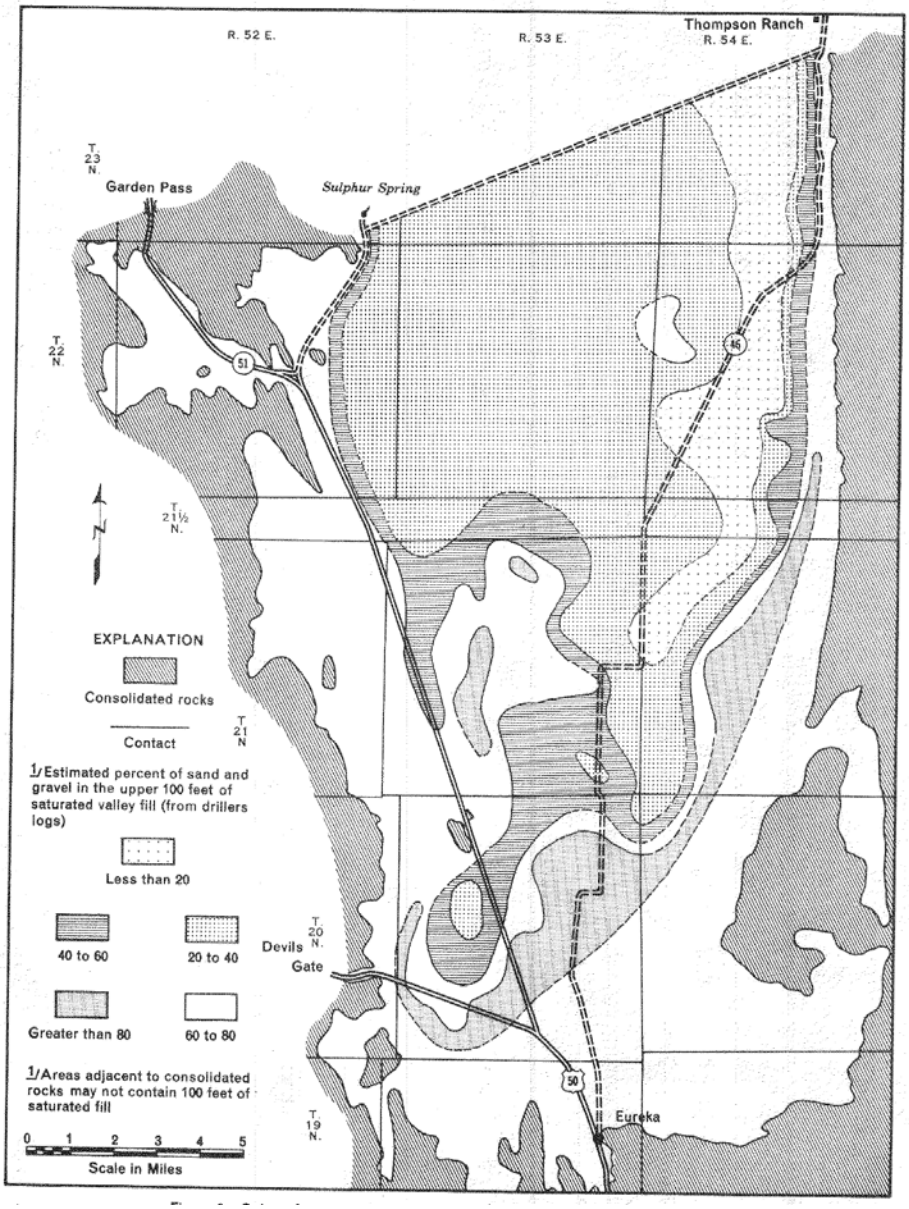

Figure 2.5 Subsurface distribution of sand and gravel (Harrill, 1968)

Chapter 3

Radar and InSAR Theory

This chapter discusses the general principle of radar theory, and how it relates to the development of the InSAR method.

3.1 Radar Theory –Microwave Sensors

InSAR, an acronym for Interferometric Synthetic Aperture Radar, is a method of combining imagery collected by imaging radar systems from on satellite platforms to map the elevations, movements, and changes of the Earth's surface. InSAR detects movements of the Earth's surface that including natural phenomena such as earthquakes, volcanoes, glaciers, landslides, or anthropogenic phenomena such as groundwater and petroleum extraction, watering of farms, or underground explosions. InSAR applications include mitigation and assessment of natural and man-made hazards and the quantification of the impact of human interaction with natural resources.

3.1.1 Radar Spectral Principle

Radar is an acronym for Radio Detection And Ranging. Radar waves exist in the electromagnetic spectrum range 1 mm to 1.0 m wavelength, which is designated as a microwave (Figure 3.1). In the context of terrestrial remote sensing, this spectral region is marked by an excellent atmospheric window. Therefore, this spectral range is excellent for remote sensing applications (Gupta, 2003). Within the microwave portion of the

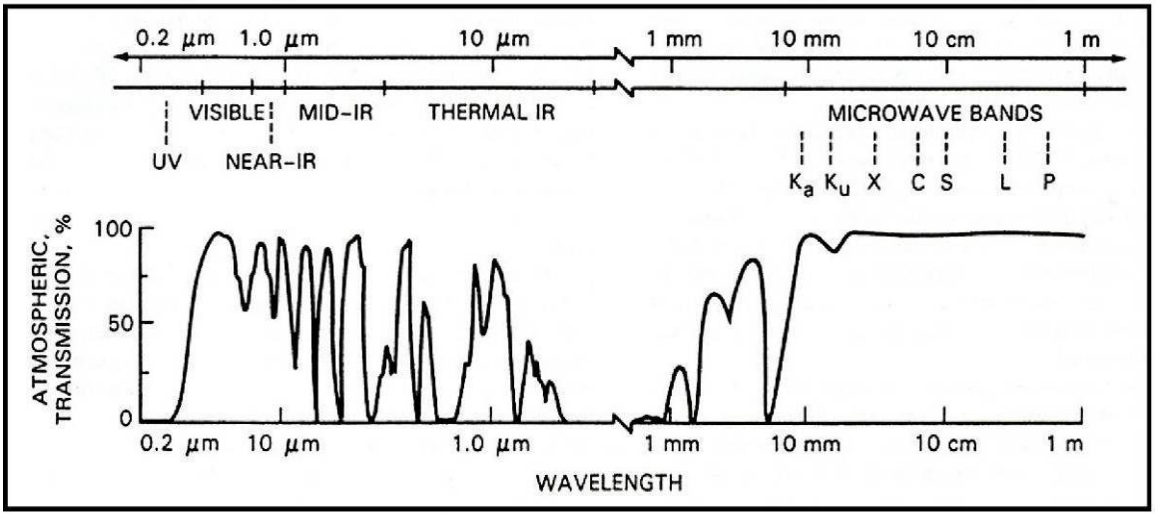

Figure 3.1 Electromagnetic spectrum showing atmospheric transmission from ultraviolet through microwave wavelengths. (Henderson and Lewis, 1998)

electromagnetic spectrum, the microwave spectrum is divided into several bands that refer to a specific wavelength and frequency range. Ranges of wavelength used in radar remote sensing are listed in Table 3.1. They were coded alphabetically during the early classified stages of radar development, and are now generally accepted. The radar band this study utilized is C-band and the wavelength is 5.7 cm. Wavelength and frequency have an inverse relationship:

$$\lambda = \frac{c}{f} \tag{3.1}$$

Where λ is wavelength (in m), c is the speed of light (3×10^8 m/s), and f is frequency (in Hz).

The techniques and sensors for Earth observation in the microwave region can be divided into two broad types, passive and active microwaves. The passive microwave sensors, called radiometers, measure the naturally available radiation, while the active microwave sensors illuminate the ground scene by an artificial source of energy and measures the

back-scattered radiation. Space borne radar sensors are active instruments, and are therefore independent of sunlight and the time of data acquisition whether it is day or night. Because these sensors operate in the microwave region, they are also independent of the atmospheric conditions such as cloud cover or rain.

Radar band	Wavelength (cm)	Frequency (gigahertz, i.e. 10^9 cycles s^{-1}
Ka	0.8 – 1.1 (0.86)[a]	40.0 – 26.5
Ks	1.1 – 1.7	26.5 – 18.0
Ku	1.7 – 2.4	18.0 – 12.5
X	2.4 – 3.8 (3.1)	12.5 – 8.0
C	3.8 – 7.5 (5.7)	8.0 – 4.0
S	7.5 – 15.0 (15)	4.0 – 2.0
L	15.0 – 30.0 (23.5)	2.0 – 1.0
P	30.0 – 100.0 (50)	1.0 – 0.3

[a] Parentheses = commonly used radar wavelength.

Table 3.1 Imaging radar bands and corresponding wavelengths and frequencies. (Gupta, 2003).

3.1.2 Radar Systems –Real and Synthetic Aperture Radar

There are two types of radar systems for detecting the physical attributes of remotely located objects. They are distinguished by antenna (aperture) length. Real Aperture Radar (RAR) is defined as having fixed antennas mounted on the bottom of an aircraft, whereas Synthetic Aperture Radar (SAR) has a longer, synthetic antenna mounted on a spacecraft. Basically, radar operates on the principle that artificially generated microwaves in a particular direction collide with objects and are scattered. The back-scattered wave is received, amplified and analyzed to determine location, electrical properties, and surface configuration of the objects.

From radar data, the position of objects is estimated from the distance along two orthogonal directions, the range direction and the azimuth direction. The range direction is the horizontal direction in which the aircraft/spacecraft-mounted antenna looks. It is generally perpendicular to the flight direction. The azimuth direction is the horizontal direction of aircraft/spacecraft flight. The azimuth and the range directions are generally mutually perpendicular.

3.1.3 Radar Ground Resolutions

For the Real Aperture Radar (RAR) system, since aircraft can only carry an antenna of limited length, the resolution in the azimuth direction (direction perpendicular to the flight direction) is much coarser to that of the range direction (the flight direction) (Hanssen, 2001). Radar sensor operating at hundreds of kilometers of altitude would require antenna dimensions between several hundred meters to kilometers (depending on the operating wavelength) to achieve resolution on the order of magnitude of meters. Later the azimuth resolution of radar image was increased by the development of Synthetic Aperture Radar (SAR); a very long antenna is synthesized by moving a small one along the flight direction path and then properly processing the received signal (Franceschetti and Lanari, 1999). Two different operation systems are illustrated in Figure 3.2.

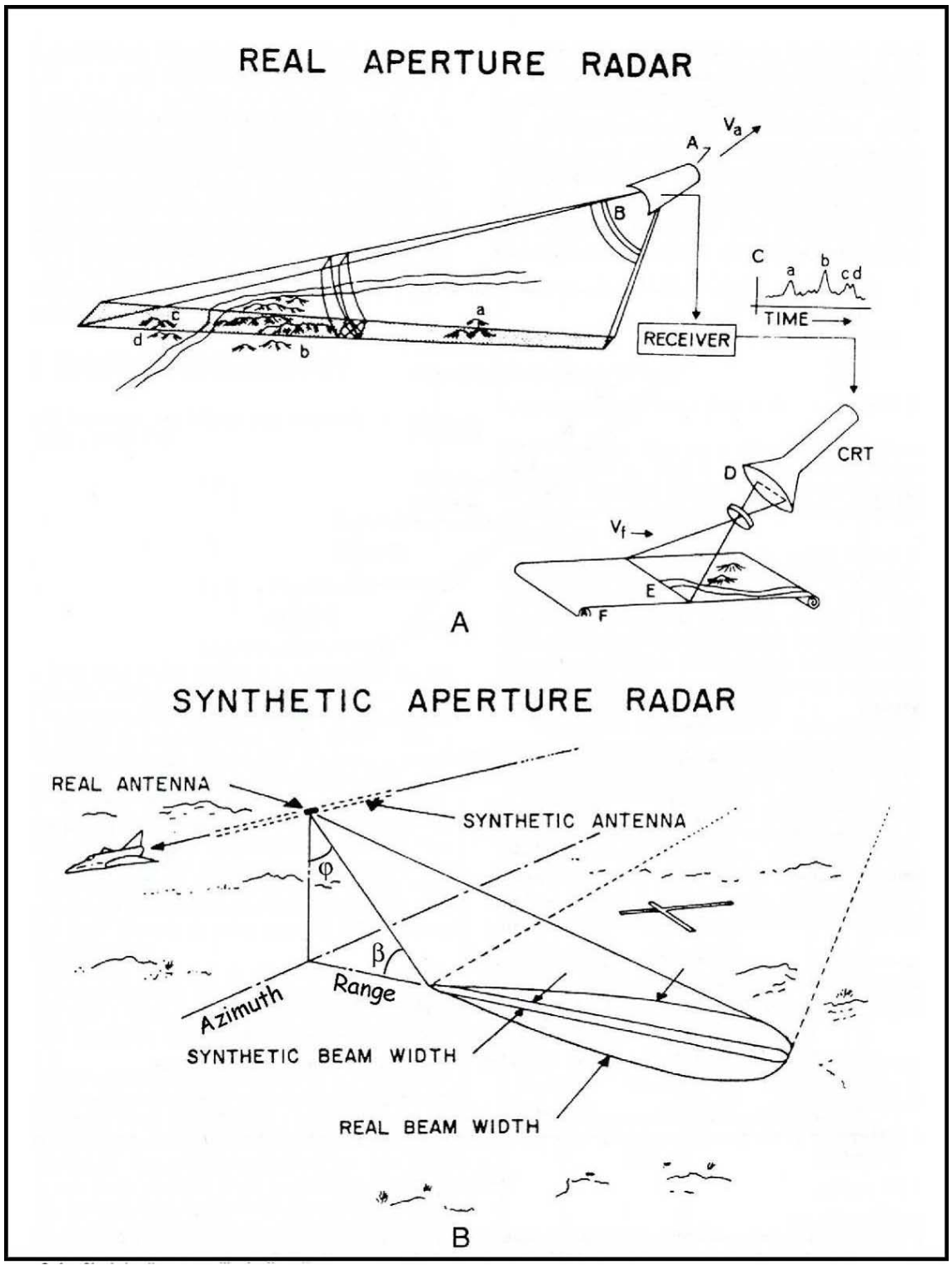

Figure 3.2. Working principle of a Real Aperture Radar (A) and a Synthetic Aperture Rader (B). Azimuth and Range directions and projections of look angle (φ) and depression angle (β). Modified from Henderson and Lewis (1998).

The ground range distance and resolution of both RAR and SAR system can be determined by very simple equations. The ground range distance, R, can be computed as

$$R = \frac{ct}{2\cos} \tag{3.2}$$

and the ground range resolution is calculated using the equation:

$$R_r = \frac{c\tau}{2\sin\varphi} = \frac{c\tau}{2\cos\beta} \tag{3.3}$$

Where c is the speed of light (3 x 10^8 m/sec), t is the time interval between transmitted and received pluses, τ is the pulse duration, φ is the look angle of the satellite, and β is the depression angle of the radar energy at the ground surface (Gupta, 2003).

The range resolution is dependent on depression and/or look angles. For a smaller depression angle it is finer, and for a larger depression angle it is coarser. Ground resolutions are not constant from the near to far range. Hence, the range resolution varies depending upon the area of interest within any given scene.

Generally, azimuth location is determined from the position of the aircraft/spacecraft in the azimuth direction. Azimuth resolution is a very important factor in evaluating the performance of a radar system. The azimuth resolution is determined differently for RAR and SAR systems. RARs possess coarser azimuth resolution (A_{RAR}), and it can be calculated using:

$$A_{RAR} = \left(\frac{H}{\cos\varphi}\right) \cdot \frac{\lambda}{l} = \left(\frac{H}{\sin\beta}\right) \cdot \frac{\lambda}{l} \tag{3.4}$$

where H is the altitude of the sensor, λ is the wavelength of the sensor, l is the physical length of the antenna, and φ and β are look and depression angles respectively as before. As with the range resolution, the azimuth resolution decreases (larger resolution cell) towards the far range as φ and β increase and decrease respectively.

For SAR sensor systems, the azimuth resolution (A_{SAR}) can be determined using a simple equation:

$$A_{SAR} = \frac{l}{2} \tag{3.5}$$

where l is the physical length of the antenna. The equation simply expresses that the azimuth resolution for airborne and space-borne SAR sensors with the same antenna length will be constant regardless of the altitude of the sensor. It is one of advantage of SAR system over RAR system which the altitude of the sensor is a function of the azimuth resolution.

3.1.4 Radar Image Characteristics

The interaction of the radar signal (energy) with matter is governed by the wave nature of light. Both geometrical characteristics (shape, roughness, and surface orientation) and electrical properties (complex dielectric constant) are important. Basically, the radar return is sensitive to decameter-scale to centimeter-scale in surface slope and surface roughness, respectively. The dielectric properties of the ground materials, such as surface moisture and mineralogical composition, also influence the radar return (Gupta, 2003). Therefore, it is important to discuss some radar image

characteristics to interpret a radar image look at the ground. Two types of characteristics will be discussed; radiometric and geometric characteristics.

Radar return, also called back-scatter at the radar, is received by the antenna, amplified and recorded (Figure 3.3). On a radar image, the intensity of radar return is shown in shades of gray such that areas of higher back-scatter appear brighter. The most common types of radiometric characteristics on a radar image include diffused scattering, hard targets, corner reflector effect, specular reflection, and radiometric irregularities.

Diffused scattering is intermediate radar return and dominates most of the area on a radar image which is caused by rough ground surfaces and vegetation. Metallic objects and corner reflectors produce very strong radar responses. These objects such as bridges and railway tracks, called hard targets, have a high dielectric constant and generally are easily identified on a radar image.

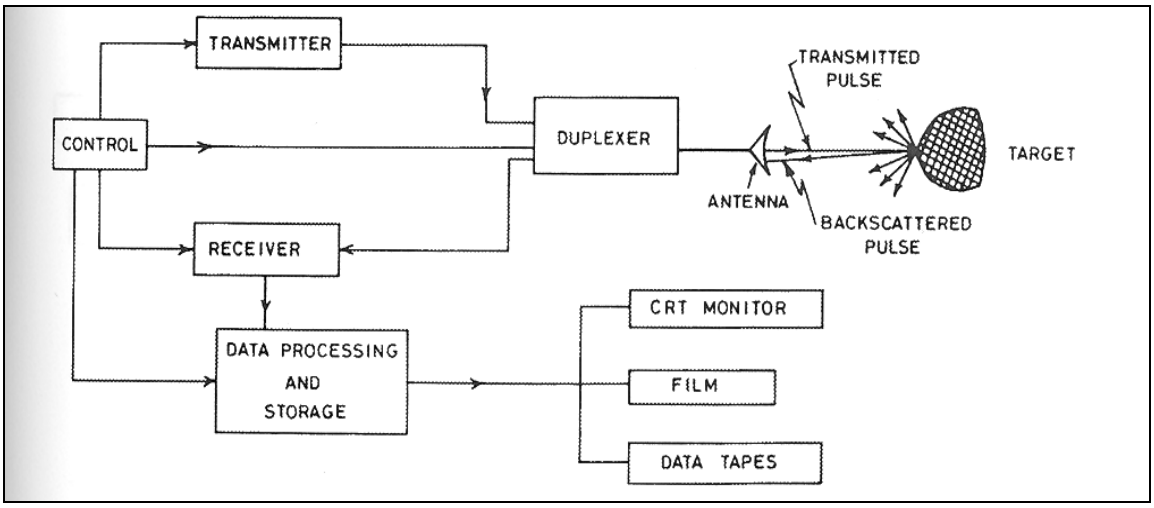

Figure 3.3 Basic structure of a radar system (Gupta, 2003)

Corner reflector effect is produced when the object has a rectangular shape, such as a vertical wall joining with the ground, leading to echoes and a high radar return. Artificial corner reflectors are often installed to calibrate radar backscatter as well as to

create ground control points for image geocoding. Specular reflection effect is produced by smooth surfaces, such as a quiet water body, playa lake, and tidal flat. These objects produce little or no return at the antenna by reflecting in a very small angular zone given by Snell's Law, resulting in a dark tone. Radiometric irregularities include side-lobe banding and speckle noise. Side-lobe banding is the presence of brighter and darker bands, parallel to the azimuth direction. Speckle noise accompanies data processing for higher azimuth resolution in the SAR system, and occurs due to the coherency of the radar signal and the presence of a statistically distributed reflecting target inside the resolution cell. Therefore, higher azimuth resolution leads to greater image speckle noise (Gupta, 2003).

The geometry of imaging radar systems is fundamentally different for most of the optical and infrared systems because of its side looking operation and its principal characteristic of measuring the traveling time of signals. A few important types of geometric distortions which affect the interpretation and application of radar imagery, and those include foreshortening, layover effects, radar shadow and speckle.

Relief displacements in radar images are one dimensional and perpendicular to the line of flight. When a vertical feature on the ground is encountered by a radar pulse the top (point b in Figure 3.4) of the feature A may be reached before the base (point a in Figure 3.4), thus the backscatter from the top of the feature (point b_1) returns to the radar before that of the bottom (point a_1). As a result the feature will appear to shorten toward the sensor in the image, and this phenomenon is generally called "foreshortening." For feature B, the radar pulse reaches the base of he feature (point c in Figure 3.4) before the

top (point d in Figure 3.4). As a result the feature will not be represented in its true size on the image (point c_1 and d_1), but will be compressed in the image, and is called layover.

Radar shadow is another effect of the side-looking operation of radars. For feature A the right side of the slope faces away from the incident radar wave, but less steep than the depression angle and will be illuminated weakly by the radar. Feature B shows a slope on the right side that is steeper than the depression angle. As a result the area of non-illumination extends beyond the sloped area masking down-range features in a radar shadow.

It is important to note that the depression look angle changes across the swath, and that this will have an effect on the degree of radar shadow that will occur. Thus a feature that shows an extensive shadowing at far range can be illuminated at near range.

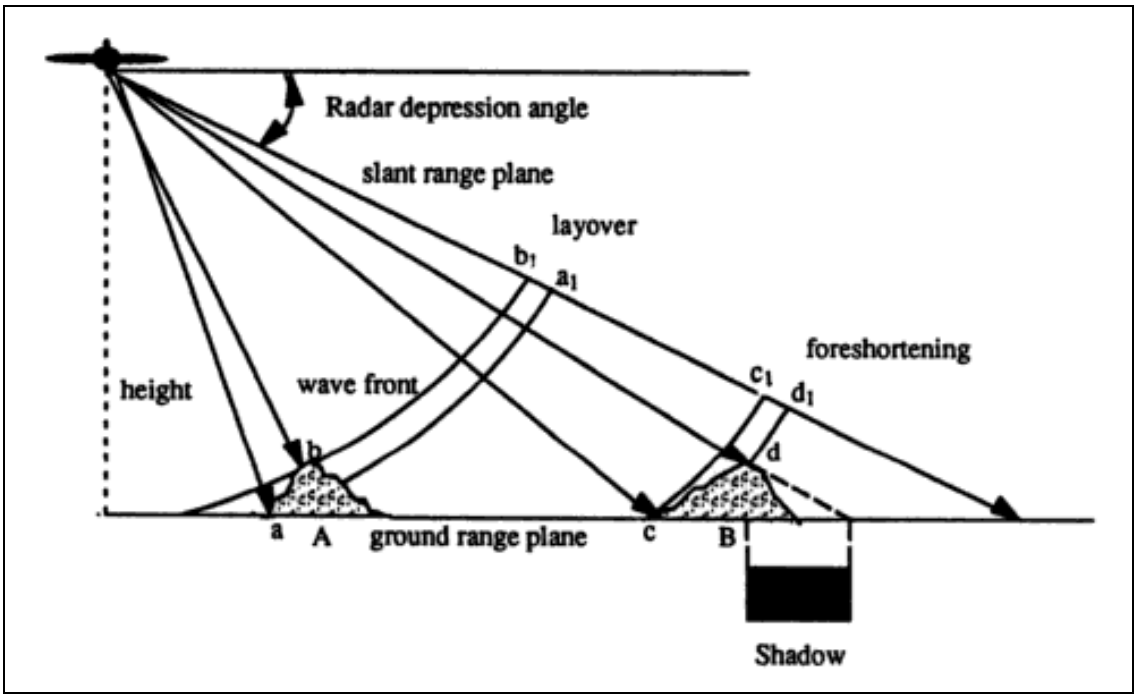

Figure 3.4 Effects on terrain relief of radar image showing layover in feature A and foreshortening and shadowing in feature B. (Belward and Valenzuela, 1991)

Speckle noise is another feature needing consideration for radar imaging, which accompanies data processing for higher azimuth resolution in SAR systems. The speckle noise occurs due to the coherency of the radar signal and the presence of statistically distributed reflecting targets inside a one resolution cell. It appears as a grainy “salt and pepper” texture in an image. Processing for higher azimuth resolution leads to greater image speckle noise, and can be reduced by going through multi-looking processing or spatial filtering.

3.1.5 Rader Return

The backscattered signal received at the radar antenna is called radar return. It is important to quantify the amount of transmitted energy that is reflected and recorded by the radar system. For SAR analysis radar return is a response to factors described in this section, therefore it can be used to determine the types of environment or conditions which are not favorable for InSAR analysis. The radar equation describes the dependence of radar return on various parameters, and is given as follows (see the description of the radar equation by Henderson and Lewis, 1998);

$$P_r = \left(\frac{P_t G^2 \lambda^2}{4\pi^3 R_s^4}\right)\sigma \tag{3.5}$$

where P_r is the power received (or radar return) by the radar antenna, P_t is the power transmitted, G is the antenna gain, λ is the radar wavelength, R_s is the slant range distance between antenna and target, and σ is the effective backscatter of the target.

The magnitude of power transmitted (P_r), which can be generally taken as a constant during a particular operation, directly affects radar return. The antennal gain (G) is a measure of current losses within the antenna material, therefore it is taken into the equation for the transmitted power which is energy transmitted in all directions.

The radar return is also directly related to the wavelength at which it operates and is also constant because a particular radar imagery is acquired at a fixed wavelength. The magnitude of the wavelength has to be taken into account while interpreting the imagery. The various radar wavelengths used are listed in Table 3.1. The slant range distance depends on the altitude of the sensor-craft and the look angle. For space-borne SAR systems, it may of the order of 250-800 km. The radar return intensity decreases as the fourth power of slant range.

Effective backscatter of the target, σ, depends upon local incidence angle, surface roughness, dielectric constant and wavelength. Local angle of incidence, which is an angle between the direction of the incident beam and the local normal to the surface, is one of the most important factors in radar return. Figure 3.5 shows that a small incident angle leads to higher backscatter and as the incident angle increases (a), the amount of backscattered energy at the radar antenna decreases (b and c). Roughness is directly related to the wavelength of the sensor,

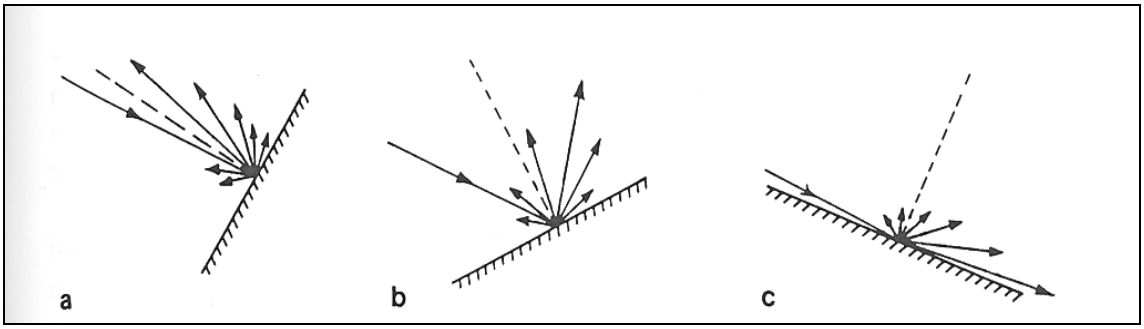

Figure 3.5 Variation in incidence angle caused by local topography, the orientation of the imcoming radar beam held constant. a. Low incidence angle, b. moderate incidence angle, c. highincidence angle. From Gupta (2003).

and criteria to quantify smoothness or roughness of a surface have been developed. The Raleigh criterion classifies a surface as rough if the root mean square of surface roughness (h_{rms}) has the following relation;

$$h_{rms} > \frac{\lambda}{8\cos\theta} \tag{3.6}$$

where h_{rms} is the average height variation of the asperities on the surface, λ is the wavelength and θ is the incident angle. Peake an Oliver (1971) modified the Raleigh criterion and qualified that a targeted surface is considered smooth (specular reflector) when:

$$h_{rms} < \frac{\lambda}{25\cos\theta} \tag{3.7}$$

and rough (diffused scattered) when:

$$h_{rms} > \frac{\lambda}{4.4\cos\theta} \tag{3.8}$$

Therefore, if an entire resolution cell is smooth such as quiet water surface, all of the energy will be reflected away from the sensor; conversely, if an entire resolution cell is rough, some of the energy will be reflected back to the sensor and will be received.

3.2 Principle of Interferometric Synthetic Aperture Radar (InSAR)

Interferometric Synthetic Aperture Radar (InSAR) is a method to generate an image which displays surface deformation by combining and comparing an initial SAR image, called a master image, acquired at a known location or a point in time with a

second SAR image, called a slave image, acquired at the same location later in time using complex algorithms. SAR interferometry permits determination of differences in the three dimensional location of objects at subcentimeter resolution by precisely comparing the radar data of the two SAR scenes. This section will discuss the principle and the basic process of SAR interferometry.

3.2.1 Space-Borne SAR Data

SAR data from a number of satellite sensor systems have been used for interferometric processing such as Seasat, ERS-1/-2, Radasat, JERS-1, ENVISAT and more recently ALOS. Table 3.2 summarizes the most important space-borne SAR missions and important design parameters of each mission. When multiple satellite data are available, the parameters to be considered to depend on the objective of the study, that is to generate interferograms. The repeat period of the satellite is a key consideration for the smallest temporal resolution possible of any interferometric pairs. The altitude, incidence (look) angle, and swath width are all geometric considerations that will impact range resolution, magnitude of reflected energy, and the severity of the distortions. Wavelength is related to the satellite's line of sight (LOS) resolution, penetration potential (both soil and vegetation), and magnitude of reflected energy (Gupta, 2003).

In this study, SAR data from three European Space Agency (ESA) satellites; (1) European Remote-Sensing satellite 1 (ERS-1), (2) European Remote-Sensing satellite 2 (ERS-2), and (3) Environmental Satellite (Envisat) were utilized. The spatial resolution for the SAR sensors on these satellites are approximately 30 m (100 ft), and the orbit repeat cycle is 35 days (ENVISAT and ERS-1/2 for the majority of the mission time).

	Seasat	SIR-A	SIR-B	SIRC/ X-SAR	Almaz-1	JERS-1	ERS-1/ ERS-2	Radasat	Envisat	ALOS (Fine)	ALOS (ScanSAR)
Lanch	1978	1981	1984	1994	1991	1992	1991/1995	1995	2002	2006	2006
Repeat Period (day)	3	-	-	-	-	44	35	35	35	46	46
Altitude (km)	795	259	225	225	300	568	777	~800	777	690	690
Wavelength (cm)	23.5 L-band	23.5 L-band	23.5 L-band	23.5 L-band	10 S-band	23.5 L-band	5.7 C-band	5.7 C-band	5.7 C-band	23.5 L-band	23.5 L-band
Incident angle (deg.)	23	50	15-64	15-55	30-60	39	23	20-50	20-50	8-60	18-43
Swath width (km)	100	50	10-60	15-60	20-45	75	100	10-500	100	40-70	250-350
Azimuth resolution(m)	25	40	17-58	30	15	18	28	9-100	25		
Range resolution(m)	25	40	25	10-30	15-30	18	26	10-100	25	14-88	100

Table 3.2 List of space-borne SAR missions and important design parameters. Modified from Gupta 2003

The ERS-1/2 satellites were also operated in a tandem mode, with a 24-hour difference between the orbits of ERS-1 and ERS-2. Since there is only 24 hours between these tandem mode image acquisitions, there is generally good coherence. ERS-1/2 and Envisat SAR systems all use a radar wavelength of 56 mm corresponding to a frequency of 5.3 GHz, which is within the C-band radio spectrum.

3.2.2 Generation of Interferometric Synthetic Aperture Radar (InSAR)

The SAR interferometry (InSAR) technique relies on the processing of two SAR images of the same portion of the Earth's surface. This study utilizes a repeat-pass interferometry method and it makes an image from SAR data from two different times taken by the same spacecraft. In the repeat-pass interferometry method, the detection and the quantification of the ground displacement that occurred between the two acquisitions can be achieved. It is also called Differential InSAR (DInSAR). The phase signal, which is the transmitted and received signal, recorded in each resolution pixel represents the sum of all backscatter from within a resolution pixel boundary (Hanssen, 2001). The processing steps in SAR interferometry creation are the following (Figure 3.6)

1. Selection of datasets (3.2.3)
2. Co-registration of the images (3.2.4)
3. Generation of interferogram (3.2.5)
4. Topographic Phase Removal and Filtering (3.2.6)
5. Phase unwrapping (3.2.7)
6. Geocoding (3.2.8)

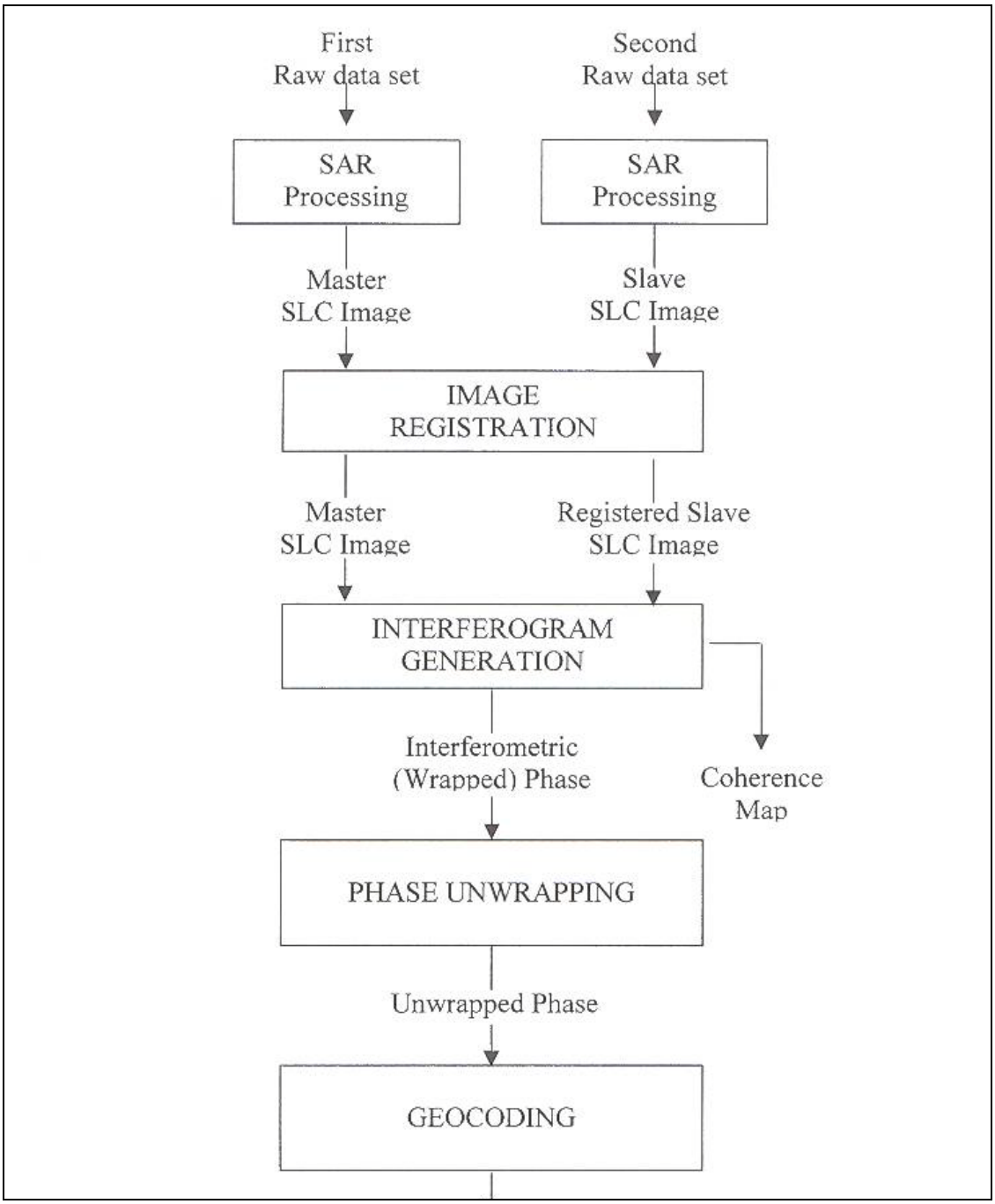

Figure 3.6 Block diagram of the InSAR processing (Franceschetti and Lanari, 1999)

3.2.3 Selection of Datasets

Data selection comes first and is the most important step in the generation of a successful interferogram. There are several factors to be considered. These include climate and vegetation of the area, time length between two data acquisitions, and spatial separation of the satellite position at two acquisitions.

Climate and vegetation factors are considered as a “temporal decorrelation”, which comes from surface changes that occur with time. In an area with wet winter climate, snow cover on the ground can cause decorrelation and incoherency of the generated image. However this factor can be minimized by selecting acquisition taken during the dry seasons. The C-band radar (ERS-1/-2 and Envisat) is widely used for InSAR analysis; however its shorter wavelength has difficulty penetrating vegetation. The reflected signal varies as the reflective properties of vegetation changes, and this cause decorrelation of the image. This factor can be minimized by selecting acquisition separated in short period (minimal vegetation coverage change).

Spatial separation of the satellite position is also an important factor which must be considered after temporal factors. Consideration for satellite geometry or spatial separation is the most critical when selecting the SAR data set to generate interfergrams. In order to minimize the decorrelation it is ideal to select two SAR data acquisitions taken spatially close to each other. The distance between the first acquisition (master scene) and the second acquisition (slave scene) is called baseline separation (B) which is the separation distance between satellite positions at the time of acquisition of the master and slave scenes. The baseline separation can be resolved into four different components: horizontal vertical, parallel, and perpendicular (Figure 3.7). A parallel baseline ($B_{\parallel}$) does

not affect a phase shift much as it is equal in all resolution cells so it is not considered for formation of a coherent interferogram. However, perpendicular baseline ($B_{\perp}$) is the main consideration which results in increasing the spatial parameter. In general, the smallest perpendicular baseline possible is best; however, successful interferogram generation is most likely to be done at perpendicular baselines up to 200 m.

3.2.4 Co-registration of Images

The phase information required for interferometric processing is contained in the raw data. First, an image, called a single-look-complex (SLC) image, is created from the raw data using a 1:5 compression algorithm for the azimuth and range resolution. The SLC image is co-registered with another SLC image to generate an interferogram.

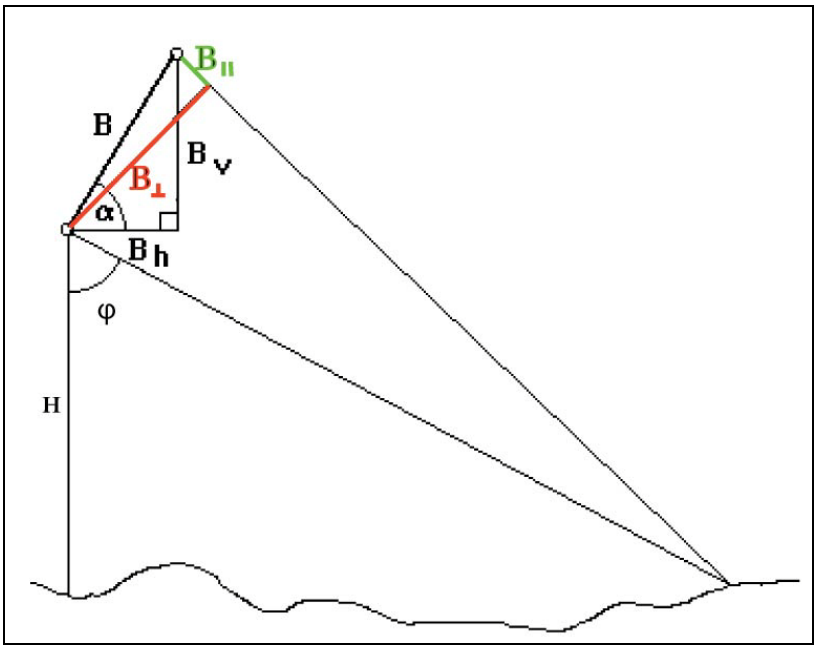

Figure 3.7 Simplified diagram of spatial geometry of interferometric baseline separation (B) of the master (M) and slave (S) satellite positions. Four components are shown: perpendicular and parallel ($B_{\perp}$ and $B_{\parallel}$) baseline components in satellite geometry and horizontal and vertical (B_h and B_v) baseline components in earth surface geometry. φ represents the look angle of the sensor.

Co-registration of the two SLC image must be very accurate. It is done on a resolution cell by resolution cell basis for the entire image, therefore this operation forms the most critical and time-consuming step. The concept and general procedure of co-registration is calculating the field of the slave image in the geometry of the master image (Gupta, 2003). Usually the operation is composed of two steps; a coarse co-registration and a fine co-registration. A coarse co-registration is first carried out using data from satellite orbits, or using arbitrary points selected in both images, to estimate the range and azimuth offsets of the two images. After this step, fine co-registration is utilized, using various statistical methods that have been developed such as maximum value of coherence coefficient, cross-correlation of pixel amplitude, and minimization of average fluctuation of phase difference (Gupta, 2003).

3.2.5 Generation of an Interferogram

After the two SLC images have been accurately co-registered, the interferogram can be generated by the subtracting of one data value from the other at each pixel in the co-registered images. Each pixel contains two important pieces of information; (1) the amplitude of the reflected energy and (2) the average value of radar phase ranging from 0-2 π of all backscattered energy. The resulting difference is measured in phase, and this phase difference between the two radar images is the most important information for interferometry. This information is generally expressed using a color sequence as fringes where one full sequence represents the full 0-2 π wavelength cycle (Figure 3.8). The interfered distance may either be in a direction towards or away from the satellite. This direction measured from the sensor to targets on the ground is called the line of sight

(LOS), and it is important that it is not perpendicular to the ground surface but has an angle called the incident angle (see Table 3.2). Any change in a place or position will be measured in the LOS distance between the satellite and the ground.

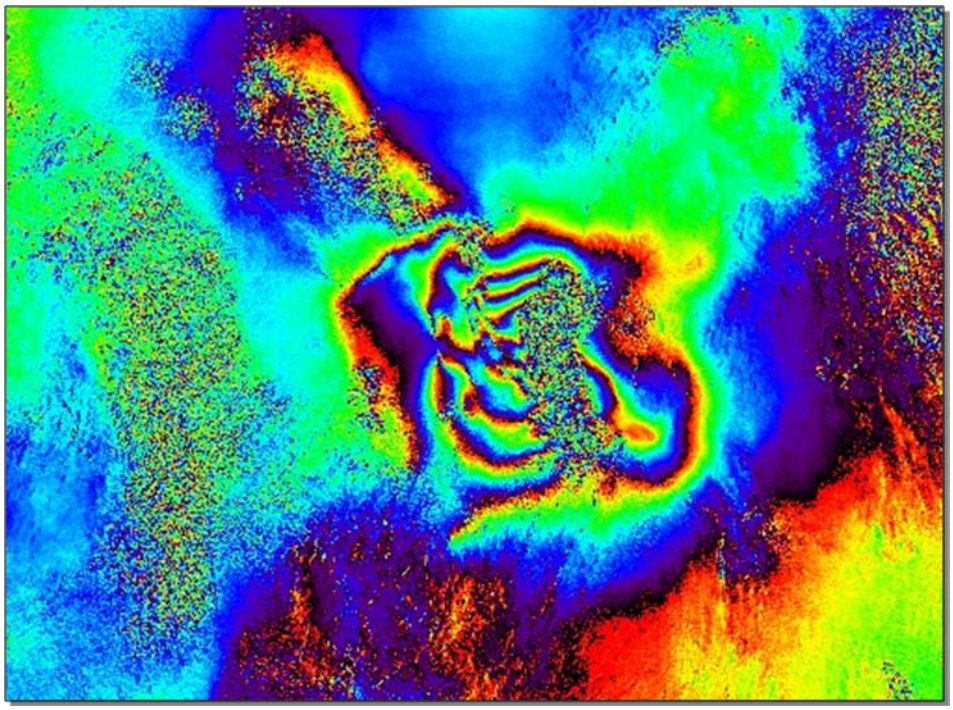

Figure 3.8 Interferometric fringes, generated from ERS data (September 28, 1996 and November 27, 1999).

When the two SLC images are interfered, the resultant interferogram phase value (φ_{int}) includes several phase-contributing components. The main component is topographic phase (φ_{topo}) which is the distance of the ground surface backscatter to the sensor. This phase value is used to create a DEM (Digital Elevation Map) which is another use of radar interferometry. Any deformation (φ_{def}) occurring between the acquisition of the master and the slave images is included in the topography phase. Therefore, the resultant interferogram phase value (φ_{int}) can be determined simply as;

$$\varphi_{int} = (\varphi_{topo})_{\text{master}} - (\varphi_{topo})_{\text{slave.}} \quad (3.9)$$

However, additional factors must be included; (1) a phase shift resulting from atmospheric effects (φ_a), (2) a decorrelative noise effect (φ_{noise}), (3) the "flat earth" contribution ($\varphi_{flat\text{-}earth}$) resulting from a pixel being in a slightly different position within the scene due to a baseline separation, and (4) a phase shift resulting from orbital inaccuracies (φ_{orb}). All four components need to be considered and the resultant interferogram phase value (φ_{int}) by subtracting the slave image from the master image and can be expressed as (Raucoules, et al., 2007):

$$\varphi_{int} = (\varphi_{topo} + \varphi_a + \varphi_{noise} + \varphi_{flat\text{-}earth} + \varphi_{orb})_{\text{master}} - (\varphi_{def} + \varphi_{topo} + \varphi_a + \varphi_{noise} + \varphi_{flat\text{-}earth} + \varphi_{orb})_{\text{slave}} \quad (3.10)$$

3.2.6 Topographic Phase Removal and Filtering

The principal phase component in an SLC image is the topographic phase and during InSAR processing this phase needs to be removed to determine the phase change due to the surface deformation. The process utilizes another source which is independent from the SAR phase signal but which has potential for showing some phase changes. The DEM data from the National Elevation Dataset (NED) is commonly used to subtract the topographic phase from the SAR phase signal. In this study, DEM were obtained from the USGS National Map Seamless Server. The resolution of downloaded DEM was decreased from 30 m to 60 m in order to decrease the processing time and the size of image.

After the topographic phase is removed, the remaining phase is composed mostly of the phase changes dominated by surface deformation. However, there are residual phases from any phase components. These residual phase signals appear as noise in the interferogram. Residual signals from the atmospheric phases cause significant noises or incoherency in the interferogram because the atmospheric conditions can change at any time. Removal of all residual phases causing noise in a single interferogram is not practical and is a very time consuming process if multiple interferograms need to be processed. It is necessary for a particular research purpose to identify which noise factor can be ignored or must be considered such as atmospheric consideration in dry or humid area.

3.2.7 Phase Unwrapping

Phase unwrapping is a very important aspect of interferometry and leads to determination of the absolute phase from the measured phase. The interferogram generated from SAR signals is called a wrapped interferogram and each resolution pixel contains a phase value ranging from 0 - 2π. Figure 3.9 illustrates how a LOS change of one half of a wavelength leads to the formation of one full fringe. A phase value is a periodic function of 2π, which means that the value wraps after reaching 2π (i.e. goes back to zero), and is represented as a sequence of 0-2π color fringes (discussed in 3.2.5), and cannot be used directly to estimate the surface elevation. For ERS-1, ERS-2 and Envisat, the LOS displacement equates to a total of 2.83 cm per fringe.

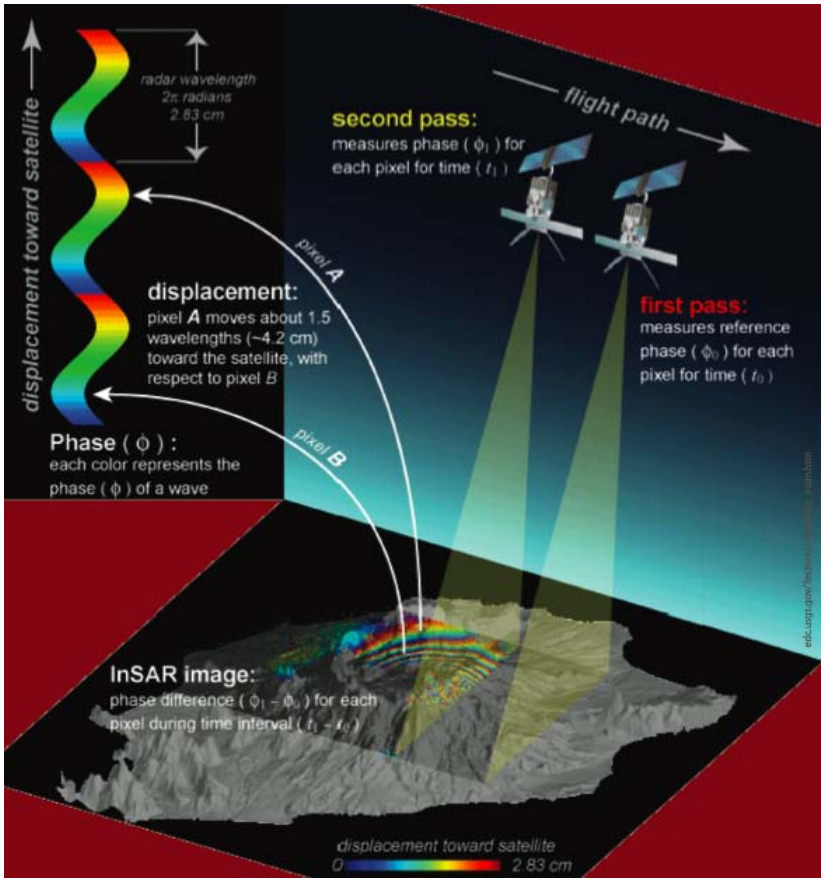

Figure 3.9 A caldera-floor subsidence model illustrating how one full fringe forms from a LOS change of wavelength. (Stanford Science Magazine, 2006)

In order to obtain the elevation change data, the measured phase values must be unwrapped from the measured 0-2π wrapped values. In this study, an algorithm developed by Goldstein et al. (1988) was utilized for phase unwrapping. The result of unwrapping the image is a georeferenced image showing LOS change for each pixel in radians. The LOS change in radar radian (LOS_{radian}), which is a real number, allows determining an actual distance number (LOS_{actual}) in centimeter for this study by using a conversion equation;

$$LOS_{actual} = \frac{LOS_{radian} \cdot \lambda}{4\pi} \tag{3.11}$$

Unlike a wrapped interferogram, which displays every phase data in each resolution pixel, an unwrapped interferogram will have pixels with no phase values as the result of the conversion algorithm. Therefore, the unwrapped interferogram will not cover (or drop-out) the areas of low coherence, in other words, it results in an image with real, coherent, and a well-correlated interferogram without any noise factor consideration (Figure 3.10). These unwrapped interferograms allow for combining of multiple short-term interferograms to evaluate longer time periods. The “stacked” interferogram shows minimal temporal decorrelation, resulting in a clear less drop-out cumulative data interferogram.

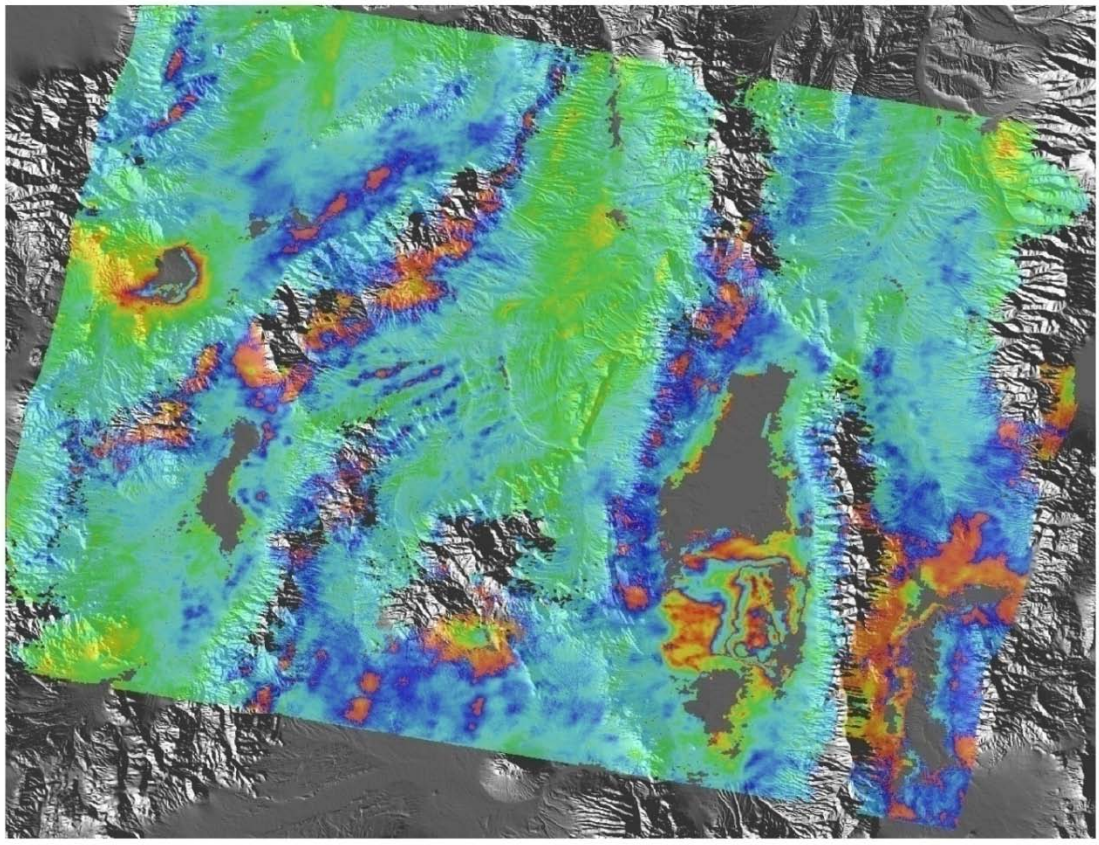

Figure 3.10 Unwrapped interferogram showing areas of drop-out data resulting from low coherence in InSAR processing.

3.2.8 Geocoding

The SAR interferogram generated is in a co-ordinate system related to the SAR geometric configuration. Conversion is required to present the data/DEM in the universal cartographic grid, called geocoding. It computes the absolute position of a pixel in the specific/standard Cartesian reference system. The DEM used to remove topographic phases, was used as a reference for this study.

Geocoded interferograms can be used for any cartographic analysis such as in ArcGIS software to create maps with geographic features or other data components.

Chapter 4

Ground Subsidence and Aquifer Compaction

The vertical ground movements of subsidence, collapse, and heave are often the results of human activities that change environmental conditions. Natural occurrences, such as earthquakes and tectonic movements, also cause surface displacements. The extraction of groundwater from unconsolidated aquifers can result in ground subsidence caused from the compaction of clay interbeds within the formation and the decrease in pore water pressure. This chapter will discuss the mechanism of aquifer compaction in alluvial subsidence.

4.1 Aquifer Compaction Mechanism

Ground subsidence occurs in unconsolidated to semi-consolidated sediments containing confined or semi-confined sand and gravel aquifers interbedded with clayey aquitards (Rahn, 1996). Lowering of the groundwater level can lead to ground surface subsidence and is attributed to the consolidation of sedimentary deposits (Bell, 1992). This section will discuss how the consolidation of sediments occurs due to groundwater withdrawal, the stress changes induced in the aquifer system, and changes to the specific storage of the aquifer from consolidation.

4.1.1 Pore Water Pressures and Effective Stresses

The concept generally used for stress analysis in soil mechanics in a system is that the total normal stress (σ) at any given point acts on the soil grains and the water held in

the pores. This was first developed by Terzaghi (1925) as the principle of effective stress. The component of the normal stress acting on the soil grains is called the effective stress (σ') and another component of the normal stress acting on the pore water is called the pore water pressure (*u*) (Terzaghi et al., 1996). From this concept the total stress (σ) can be expressed as:

$$\sigma = \sigma' + u \tag{4.1}$$

Understanding pore water pressures in subsurface environments is important as water pressures have a significant influence on the engineering behavior of most rock and soil masses. A pore water pressure (*u*) acts in all directions in equal intensity. It is equal to the depth below the hydrostatic water surface (*h*) times the unit weight of water (γ_w), and is expressed with the following equation:

$$u = h\,\gamma_w \tag{4.2}$$

The efficiency of a soil supporting structure is influenced by the effective or intergranular stress (σ'), that is, the pressure acting between the particles of the soil which develops resistance to applied load. It is an excess stress over the pore water pressure (*u*) within the total stress (σ) at any point on a section, and is expressed with the following equation:

$$\sigma' = \sigma - u, \tag{4.3}$$

The effective stress is also approximately the force per unit area carried by the soil skeleton. Figure 4.1 illustrates how the total stress, in this study, from lithostatic overburden, on an aquifer is supported by effective stress on the grain-to-grain skeleton of the aquifer as well as the pore fluid pressure in the aquifer. It is a very important concept that such stress in a soil mass controls its volume change and strength (Das,

2006). Increasing the effective stress induces soil to settle to a denser state by consolidation.

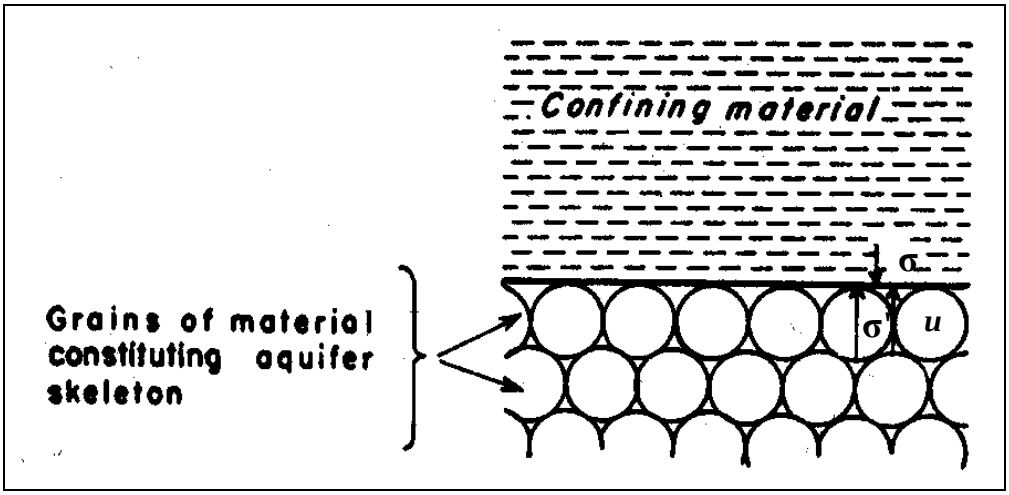

Figure 4.1 Schematic Illustration showing pressures acting at aquifer interface. Symbols σ, σ', and *u* represent the total stress, the effective stress, and the pore water pressure, respectively. (modified from Ferris et al., 1962)

4.1.2 Stress Changes Due to Water Withdrawal

The relation between changes in pore water pressure and compression of the aquifer system is based on the principle of effective stress,

$$\sigma = \sigma' + u, \tag{4.3}$$

When a change in the water table (Δh) in the aquifer-system occurs, the change in pore water pressure (Δu) is calculated using an equation:

$$\Delta u = \Delta h \, \gamma_w \tag{4.4}$$

According to Terzaghi et al. (1996), however, a change in the pore water pressure does not produce volume change directly, whereas all the measurable effects of change in stress are due exclusively to the changes in the effective stress. Therefore, investigating the saturated body of soil requires the knowledge of both the total stress and the pore water pressure.

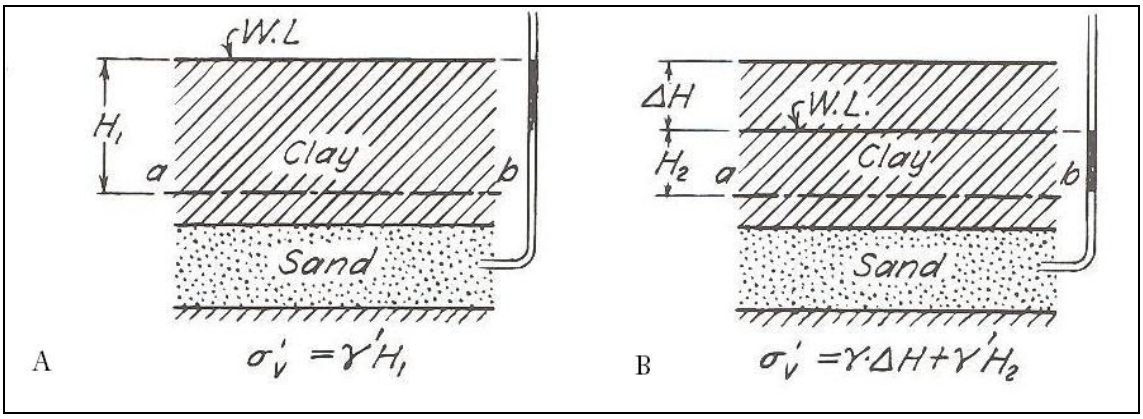

Figure 4.2 Diagrams illustrating physical causes of settlement of clay surface due to pumping from underlying water-bearing sand (Terzaghi et al., 1996)

Figure 4.2 illustrates the physical cause of compression of a saturated clay layer overlying a sand layer. The water table is lowered from the ground surface (A) to a distance ΔH (B) by pumping from the layer of sand. In A, the effective stress and the pore water pressure in a section ab are:

$$\sigma' = \gamma' H_1 \tag{4.5}$$

$$u = \gamma_w H_1 \tag{4.6}$$

respectively, where γ' is the dry unit weight of the clay and γ_w is the total unit weight of water. As the water table lowered (B) the effective stress and the pore water pressure become:

$$\sigma' = \gamma \Delta H + \gamma' H_2 \tag{4.7}$$

$$u = \gamma_w H_2 \tag{4.8}$$

where γ is the total unit weight of the saturated clay. The change in effective stress ($\Delta \sigma'$) due to the lowering of the water table can be determined by subtracting the original effective stress from the effective stress after the water table changes,

$$\Delta \sigma' = \gamma \Delta H + \gamma' H_2 - \gamma' H_1$$

$$= \Delta H (\gamma - \gamma')$$

$$= \gamma_w \Delta H \qquad (4.9)$$

Therefore, lowering the water table by a distance ΔH significantly increases the effective stress by an amount equal to the weight of water ΔH in height. In other words, as the pore water pressure is reduced as the groundwater is removed; a greater proportion of the geostatic pressure is transferred to the soil matrix. This increase leads a progressive settlement of the surface of the clay due to consolidation.

If the formation is unconsolidated it compacts until a denser, stronger structure is formed that is once more able to support the upper part of materials. Under this principle, Galloway et al. (1998) states response of the aquifer system responds to various stress conditions in the following manner.

- When the total stress remains constant, a change in pore fluid pressure causes an equivalent change in effective stress within the aquifer system, which causes the aquifer system skeleton to compress or expand under the new load.
- When the effective stress is decreased by an increase in pore fluid pressure, the aquifer system expands elastically.
- When the effective stress is increased by a reduction in pore fluid pressure and the effective stress does not exceed the maximum past effective stress (preconsolidation stress), the aquifer system compresses elastically.
- When a reduction in pore fluid pressure causes an increase in effective stress to values greater than the maximum preconsolidation stress, the pore structure of the fine grained aquitards in the system will not sustain the soil masses, resulting in a

permanent reduction of pore volume and compaction of the aquitards. This process can be quantified in terms of two compressibilities, one is elastic and another is inelastic, each of which can be applied to the aquifer system as a whole or, if the stratigraphy is well defined, to the aquitards only.

4.1.3 Permeability and Specific Storage

The permeability of the system is the main parameter for the rate at which consolidation occurs because it depends on the rate at which the pore water can drain from the system. The time required to reach the consolidating stage varies directly according to the specific storage and the square of the thickness of the zone from which drainage is occurring (Bell, 1992).

The elastic and inelastic skeletal compressibilities, α'_k, of the aquitards are expressed in terms of the skeletal specific storages, S'_{sk},

$$S'_{sk} = S'_{ske} = \alpha'_{ke}\rho g, \qquad \sigma_e < \sigma_{e(max)}, \tag{4.10}$$

$$S'_{sk} = S'_{ski} = \alpha'_{ki}\rho g, \qquad \sigma_e > \sigma_{e(max)},$$

where subscripts e and v refer to the elastic and inelastic (virgin) properties, ρ is fluid density, and g is gravitational acceleration. When effective stress changes in the aquifer, the aquitard deforms elastically when the effective stress is less than the previous maximum effective stress, $\sigma_{e(max)}$. On the other hand, when the effective stress is greater than $\sigma_{e(max)}$, the aquitard deforms inelastically. In typical aquifer systems, which are composed of unconsolidated to semi-consolidated late Cenozoic sediments, S'_{ski} is generally 30 to several hundred times larger than S'_{ske} (Ireland et al., 1984). The aquitard

skeletal storage coefficient S'_k can be calculated by multiplying the elastic or inelastic skeletal specific storage and the thickness of the aquitards, $\Delta b'$:

$$S'_k = S'_{ke} = S'_{ske}(\Delta b'), \qquad \sigma_e < \sigma_{e(max)}, \tag{4.11}$$

$$S'_k = S'_{ki} = S'_{ski}(\Delta b'), \qquad \sigma_e > \sigma_{e(max)}.$$

Ground subsidence due to aquifer compaction, where the effective stress changes ($\Delta\sigma_e$) are due only to pore water pressure changes (Δu) under constant total stress permits the bulk elastic and inelastic storage coefficients, S^*_{ke} and S^*_{ki}, to be estimated from two parameters, the change in aquifer-system thickness or compaction (Δb) and the change in hydraulic head (ΔH) . The method widely used (Hoffmann et al., 2001, Bell et al., 2008) is to determine the ratio of the two values;

$$S^*_{ke} = \Delta b_e / \Delta H_e \tag{4.12}$$

$$S^*_{ki} = \Delta b_i / \Delta H_i$$

This estimation can be calculated if the measured compaction is assumed as the maximum compaction for the measured hydraulic head change.

The specific storage for the coarse-grained aquifers and for the pore water can be determined by the following equations which express the relationships between the compressibility of the aquifer skeleton (α_k) and the aquifer skeletal storage coefficient (S_k), and the compressibility of water (β_w) and the component of aquifer system storage attributed to the pore water (S_w), respectively:

$$S_k = S_{sk}(\Delta b) \approx \alpha_{ke}\rho g(\Delta b), \tag{4.13}$$

$$S_w = \beta_w \rho g[n(\Delta b) + n'(\Delta b')], \tag{4.14}$$

where Δb is the thickness of the aquifers and n and n' are the porosities of the aquifers and aquitards, respectively. For coarse-grained aquifers interbedded with compacting

aquitards, the difference between the elastic and inelastic compressibilities of the aquifer skeleton is considered relatively insignificant, and $\alpha_k \approx \alpha_{ke}$ (Galloway, 1999).

The aquifer-system storage coefficient S^* is defined by adding the three variables of the skeletal storage coefficients of the aquitards (from equation 4.11), the aquifer skeletal storage coefficient (from equation 4.13), and the storage attributed to water compressibility (equation 4.14).

$$S^* = S'_k + S_k + S_w. \tag{4.15}$$

4.1.4 Rate of Subsidence in Clay-rich Aquifer

As stated at the beginning of this chapter, ground subsidence extensively occurs in unconsolidated to semi-consolidated sediments containing confined or semi-confined sand and gravel aquifers interbedded with clayey aquitards. Meinzer (1928) states that the effect of pressure changes was greater in formations with high clay content. These fine-grained beds have low hydraulic conductivity and the resulting longer-term transitional head (groundwater table) changes would introduce a time delay between the withdrawal and the consequent compaction (Jacob, 1940).

Riley (1969) presented the length of time that it takes pressure within a single interbed to reach equilibrium due to changes of pressure in the adjacent aquifer. The aquitard time constant, τ, is a function of the amount of water that must be displaced and the impedance to its escape:

$$\tau = \frac{S''(b'/2)}{K'} \tag{4.16}$$

where S^* is the specific storage, K' the vertical hydraulic conductivity and b' the thickness of the interbed. S^* is a combination of storage components due to the compressibility of the interbed and of the fluid (section 4.2.3).

However, for large regional subsidence due to the consolidation of a very thick aquifer assessing the compressibility of the soils will be challenging because the degree of continuity of the drainage layers often cannot be accurately detected (Terzaghi et al., 1996).

Chapter 5

InSAR Procedures and Resulting Interferograms

The Interferometric Synthetic Aperture Radar (InSAR) method was used to determine the magnitude and lateral extent of ground subsidence resulting from pumping groundwater in Diamond Valley, Nevada. This chapter will outline the procedures and the results of InSAR processing.

5.1 Data Selection

SAR data acquired by the European Space Agency's (ESA) Environmental Remote-Sensing satellite 1 (ERS-1), Environmental Remote-Sensing satellite 2 (ERS-2), and the Environmental Satellite (Envisat), were used for this study. All three satellites cover the same descending satellite tracks and the satellite scene, Track 170 and Frame 2799, which covers the study area, is shown in Figure 5.1.

SAR data were obtained from a European Space Agency data grant and from the Western North American Interferometric Synthetic Aperture Radar (WInSAR) Consortium. Three ERS-1 and nine ERS-2 satellite data sets and thirteen Envisat satellite data sets were utilized to process the InSAR images. The scenes, which were used to create interferograms in this study, are listed in Table 5.1. Scene selections for potential pairs creating the interferogram were done using perpendicular baseline estimation by Eolisa utilities, which provided a good basis for selection. For this study, all interferometric pairs with a perpendicular baseline separation of 200 m or less were processed.

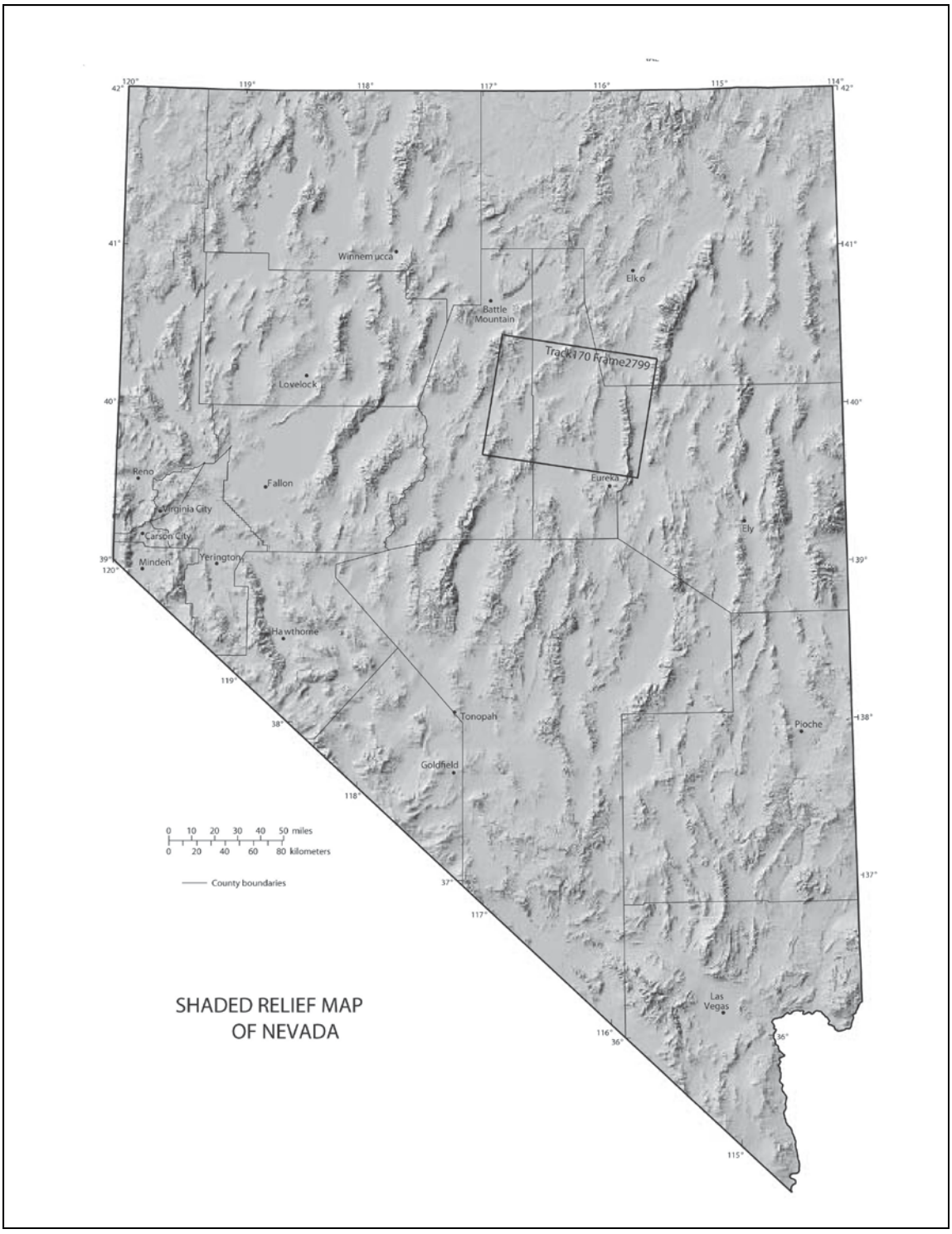

Figure 5.1 Shaded relief map showing the location of the frame used in this study. The black box represents the approximate coverage of the frame, Track170-Frame 2799. (Base map from Nevada Bureau of Mines and Geology, 1999)

Satellite	Acquisition date	Orbit number
ERS-1	06/17/1992	4824
ERS-1	09/30/1992	6327
ERS-1	07/07/1993	10335
ERS-2	11/18/1995	3030
ERS-2	04/06/1996	5034
ERS-2	05/11/1996	5535
ERS-2	09/28/1996	7539
ERS-2	07/05/1997	11547
ERS-2	04/11/1998	15555
ERS-2	05/01/1999	21066
ERS-2	11/27/1999	24072
ERS-2	04/15/2000	26076
Envisat	09/11/2004	13250
Envisat	10/16/2004	13751
Envisat	01/29/2005	15254
Envisat	05/14/2005	16757
Envisat	11/05/2005	19262
Envisat	07/08/2006	22769
Envisat	08/12/2006	23270
Envisat	09/16/2006	23771
Envisat	11/25/2006	24773
Envisat	12/30/2006	25274
Envisat	03/10/2007	26276
Envisat	05/19/2007	
Envisat	12/15/2007	30284

Table 5.1 Table of raw SAR scenes used for InSAR processing in this study. Columns indicate the satellite which imaged the scene, the date of image acquisition, and the orbit of the image scenes.

5.2 Data Processing

The program used for interferometric processing was the Repeat Orbit Interferometry Package (ROI_PAC) developed by the NASA Jet Propulsion Laboratory (JPL). The two-pass interferometric technique was utilized to create all interferograms. It uses two SAR scenes acquired on separate satellite orbits, and the topography is subtracted using a DEM.

A total of 44 interferometric pairs were processed, and 34 interferograms were successfully produced. Table 5.2 shows all of the interferograms that were successfully created for this study.

Master Acquisition Date	Slave Acquisition Date	Perpendicular Baseline (m)
06/17/1992	04/06/1996	102
06/17/1992	09/28/1996	18
06/17/1992	07/05/1997	89
09/30/1992	05/11/1996	7
07/07/1993	11/18/1995	89
04/06/1996	09/28/1996	110
04/06/1996	04/11/1998	163
04/06/1996	04/15/2000	7
09/28/1996	07/05/1997	71
09/28/1996	04/11/1998	43
09/28/1996	11/27/1999	70
07/05/1997	04/11/1998	28
07/05/1997	05/01/1999	162
07/05/1997	11/27/1999	141
04/11/1998	05/01/1999	134
04/11/1998	11/27/1999	113
04/11/1998	04/15/2000	156
05/01/1999	04/15/2000	22

Master Acquisition Date	Slave Acquisition Date	Perpendicular Baseline (m)
11/27/1999	04/15/2000	112
09/11/2004	11/05/2005	171
09/11/2004	07/08/2006	80
09/11/2004	08/12/2006	88
10/16/2004	05/14/2005	4
10/16/2004	11/05/2005	120
10/16/2004	12/30/2006	66
10/16/2004	03/10/2007	98
01/29/2005	11/25/2006	86
05/14/2005	11/05/2005	124
05/14/2005	12/30/2006	62
05/14/2005	03/10/2007	94
11/05/2005	12/30/2006	186
09/16/2006	11/25/2006	151
11/25/2006	12/15/2007	131
12/30/2006	03/10/2007	32

Table 5.2 List of all interferograms along with the average perpendicular baseline separation as calculated by ROI_PAC.

5.3 InSAR Results

For each successfully processed interferometric pair, the unwrapped result was carefully inspected for coherence of the image and any phase artifacts resulting from residual orbital, atmospheric, or topographic signals. The ENVI program for image processing was utilized for InSAR data. After a good interferogram with minimal phase artifacts was identified the unwrapped data was used to create a georeferenced interferogram. The georeferenced unwrapped interferograms were then used to create a longer time period interferogram by stacking single interferograms. The individual unwrapped interferograms must be successive one after another. In other words, the slave

scene of one interferogram matches the master scene from the next successive interferogram whenever possible.

The stacked interferogram created from the ERS-1/ERS-2 data uses the four best interferograms covering the time period of June 17, 1992, through November 27, 1999 (Table 5.3). The stacked interferogram created from Envisat data used the three best interferograms covering the time period of October 16, 2004, through December 15, 2007 (Table 5.4).

Master Acquisition Date	Slave Acquisition Date	Perpendicular Baseline (m)
06/17/1992	04/06/1996	102
04/06/1996	04/11/1998	163
04/11/1998	11/27/1999	113
04/11/1998	04/15/2000	192

Table 5.3 Acquisition dates and perpendicular baselines of the four interferograms used to create the ERS-1/ERS-2 stack.

Master Acquisition Date	Slave Acquisition Date	Perpendicular Baseline (m)
09/11/2004	11/05/2005	171
11/05/2005	12/30/2006	186
11/25/2006	12/15/2007	131

Table 5.4 Acquisition dates and perpendicular baselines of the three interferograms used to create the Envisat stack.

For a stacked interferogram, the data drop out must be considered to interpret the overall ground subsidence magnitude. All of the unwrapped interferograms created in this study have the data drop out, which is shown as the blank area in an image. Those areas were masked during unwrapping process due to low coherence between the two data sets, and a value for LOS displacement was determined as zero at that pixel. However, some

ground deformation almost certainly occurs in those zero-data areas. These areas could contain the largest ground deformation magnitudes because the low coherency mostly occurs in areas of active agricultural fields where on-going groundwater pumping is currently taking place. Therefore, the maximum magnitude of subsidence for each interferogram may not represent the actual maximum value that occurred during each particular time period. In other words, the maximum values obtained with InSAR profiles are the maximum recorded ground subsidence values ("minimum maximums"). Each individual interferogram used to create the two stacks and the stacks themselves are shown in Figures 5.3 through 5.11.

Another consideration when interpreting the magnitude of ground deformation is a profile view in the stacked interferogam. When a stack is created by some interferograms, the image will have areas of discontinuous value changes (e.g. a sudden magnitude drop down) and the profile shows a stepped look. Figure 5.2 represents a subsidence profile taken from the ERS-1/ERS-2 stack interferogram (Table 5.3). First of all, it is important to keep in mind that the subsidence magnitude of this profile is the sum of all four single interferograms. Sections of zero magnitude in the profile mean that all four interferograms have low coherency and data masked out in those areas, and consequently the stack profile has zero magnitude. In the right hand side the profile shows sudden up and down magnitude change, and these features do not represent what occurred in the section during the time period. This feature indicates that some of the single interferograms have subsidence values but some do not in this section. Only available values have been summed in the section. The estimated profile is inferred from those available values by observing overall features of the profile.

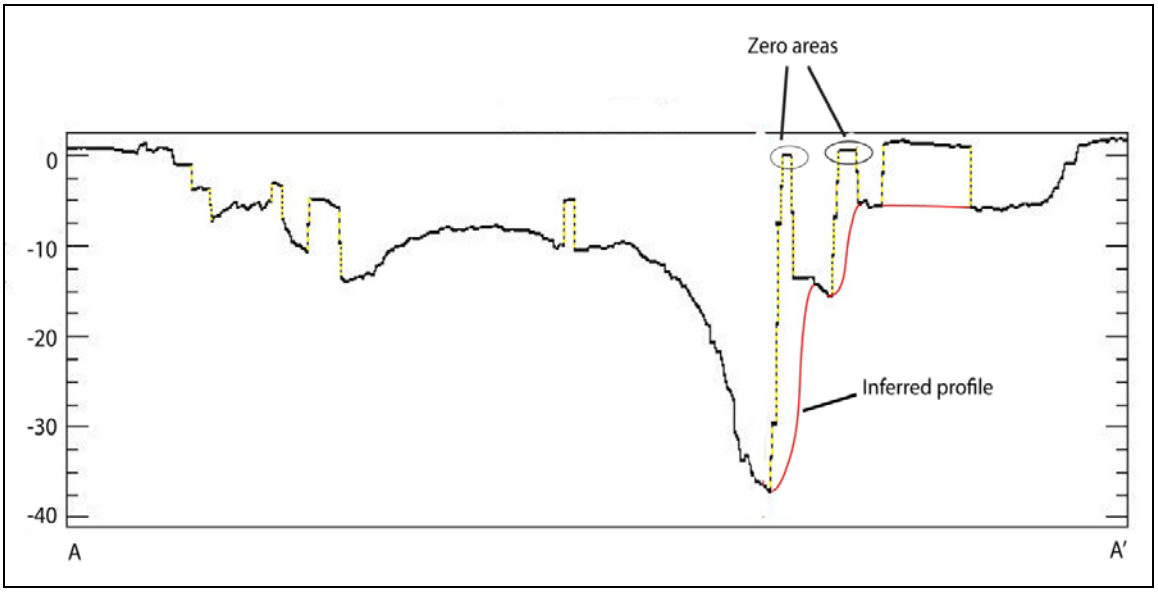

Figure 5.2 Subsidence profile from the ERS-1/ERS-2 stack interferogram modified to show zero value sections (drop-out areas on a map view), limited available values and an estimated profile.

In order to understand the amount of ground subsidence that has occurred and its lateral extent, 5 cm interval subsidence contour lines were delineated by carefully observing available and reliable pixel values. Each ground subsidence contour map from the ERS-1/ERS-2 stack and the Envisat stack is shown on the hillshaded DEM of the valley (Figure 5,12 an 5,13, respectively).

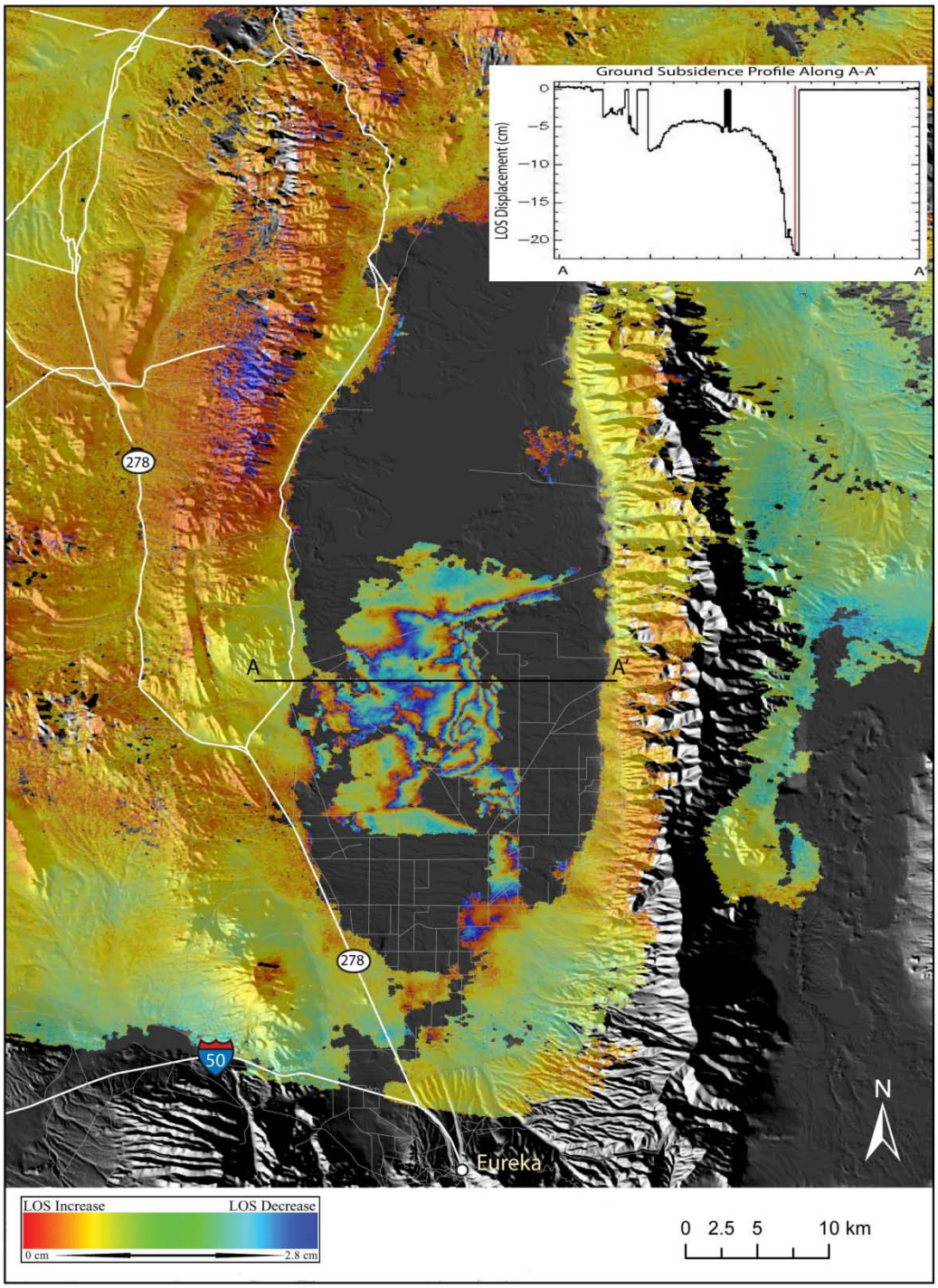

Figure 5.3 Unwrapped interferogram covering the time period of June 17, 1992 – September 28, 1996. Each red-yellow-blue color cycle (fringe) represents approximately 3 cm of LOS change. The profile at the upper right corner shows LOS change along the line (A-A') in the figure. A negative change indicates subsidence during the time period.

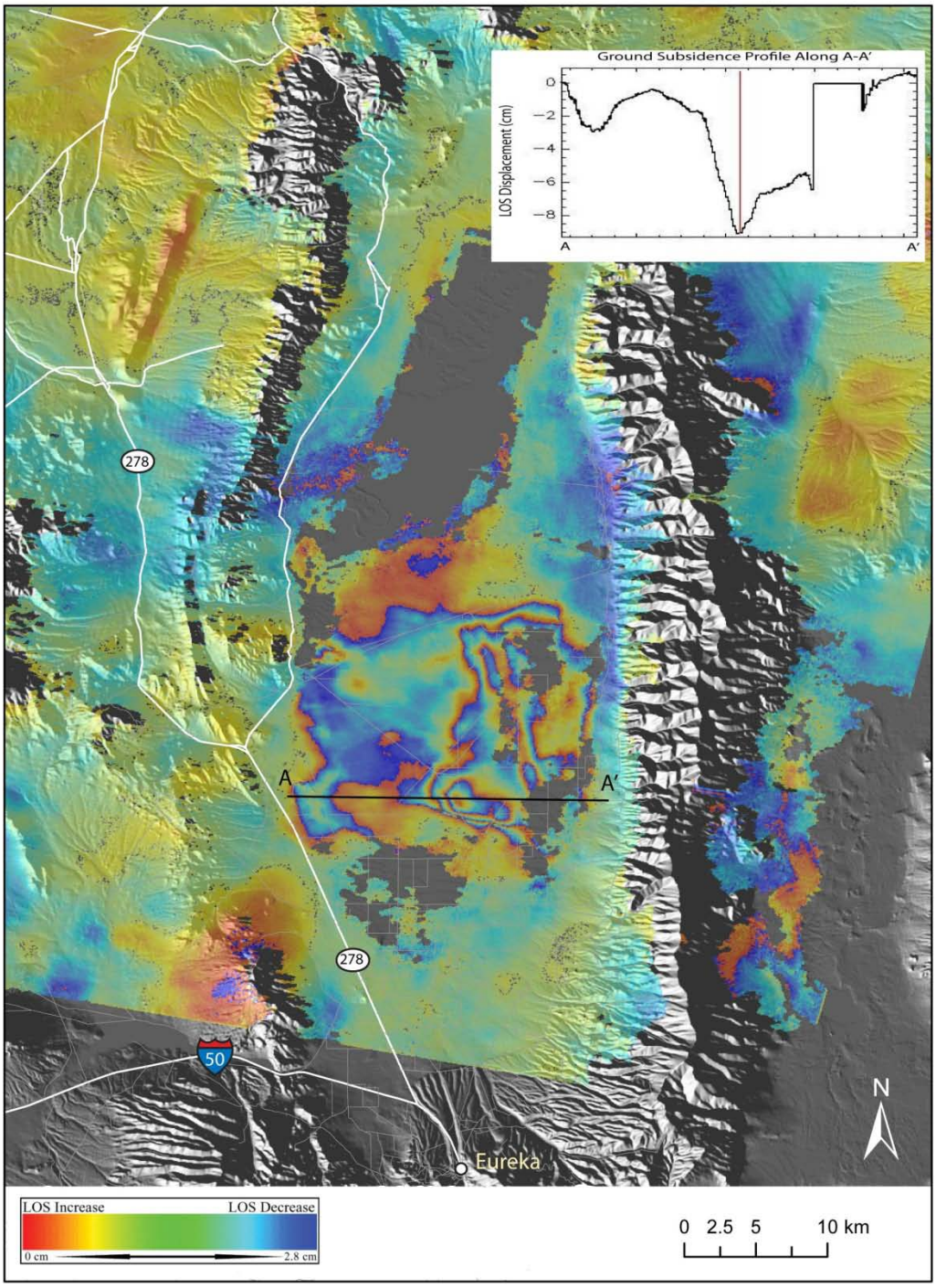

Figure 5.4 Unwrapped interferogram covering the time period of April 6, 1996 – April 11, 1998. Each red-yellow-blue color cycle (fringe) represents approximately 3 cm of LOS change. The profile at the upper right corner shows LOS change along the line (A-A') in the figure. A negative change indicates subsidence during the time period.

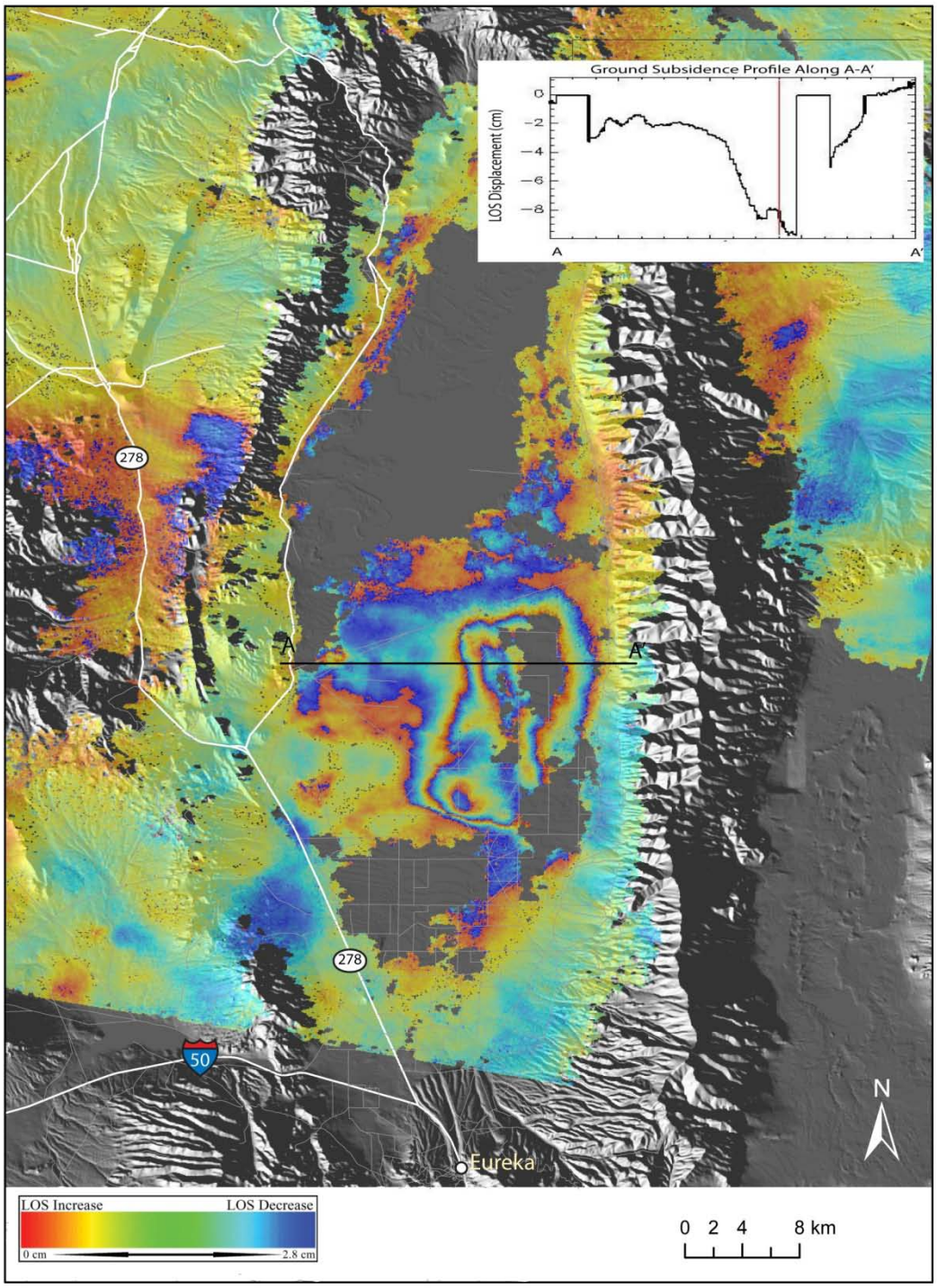

Figure 5.5 Unwrapped interferogram covering the time period of April 11, 1998 – November 27, 1999. Each red-yellow-blue color cycle (fringe) represents approximately 3 cm of LOS change. The profile at the upper right corner shows LOS change along the line (A-A') in the figure. A negative change indicates subsidence during the time period.

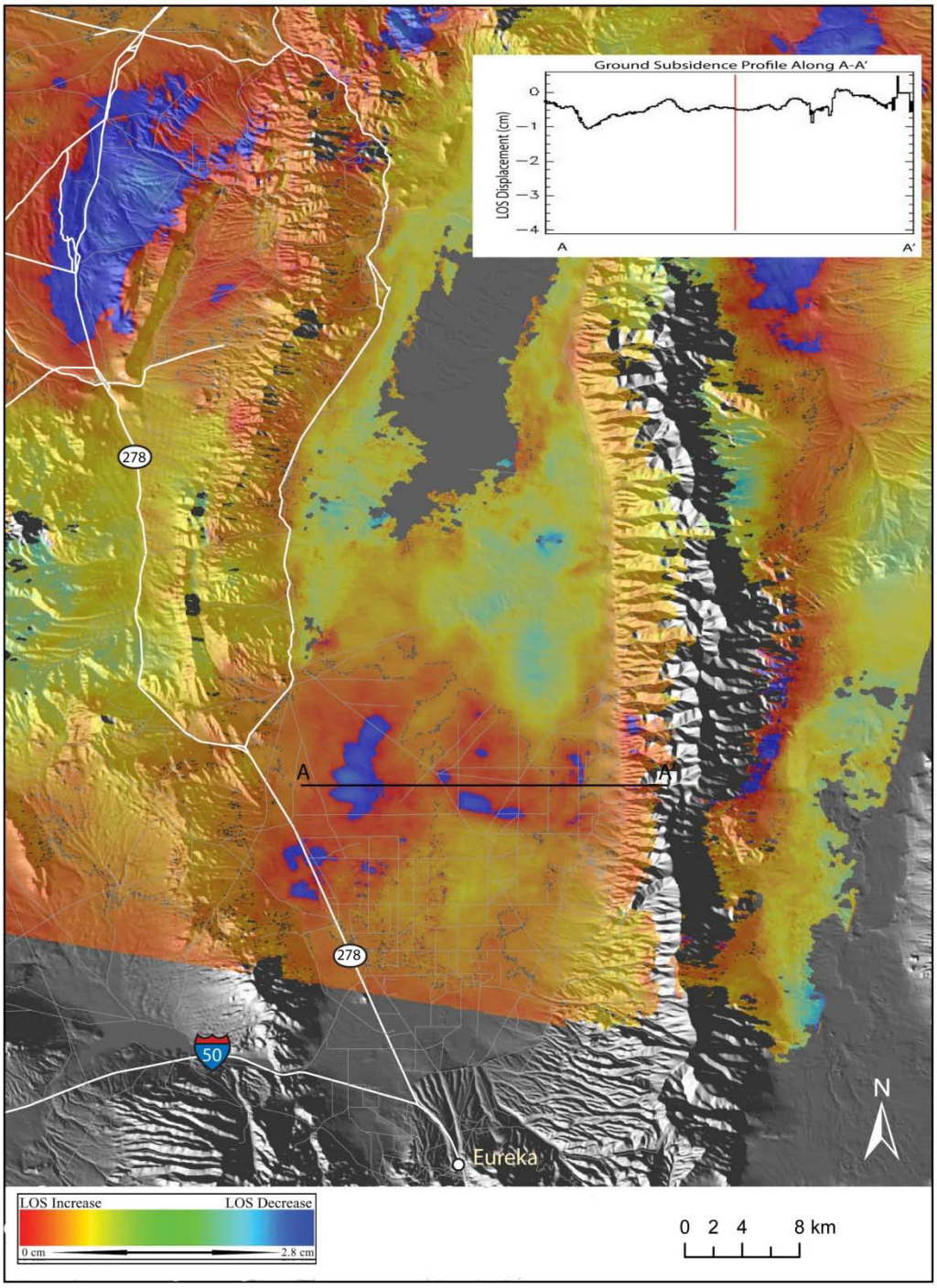

Figure 5.6 Unwrapped interferogram covering the time period of November 27, 1999 – April 15, 2000. Each red-yellow-blue color cycle (fringe) represents approximately 3 cm of LOS change. The profile at the upper right corner shows LOS change along the line (A-A') in the figure. A negative change indicates subsidence during the time period.

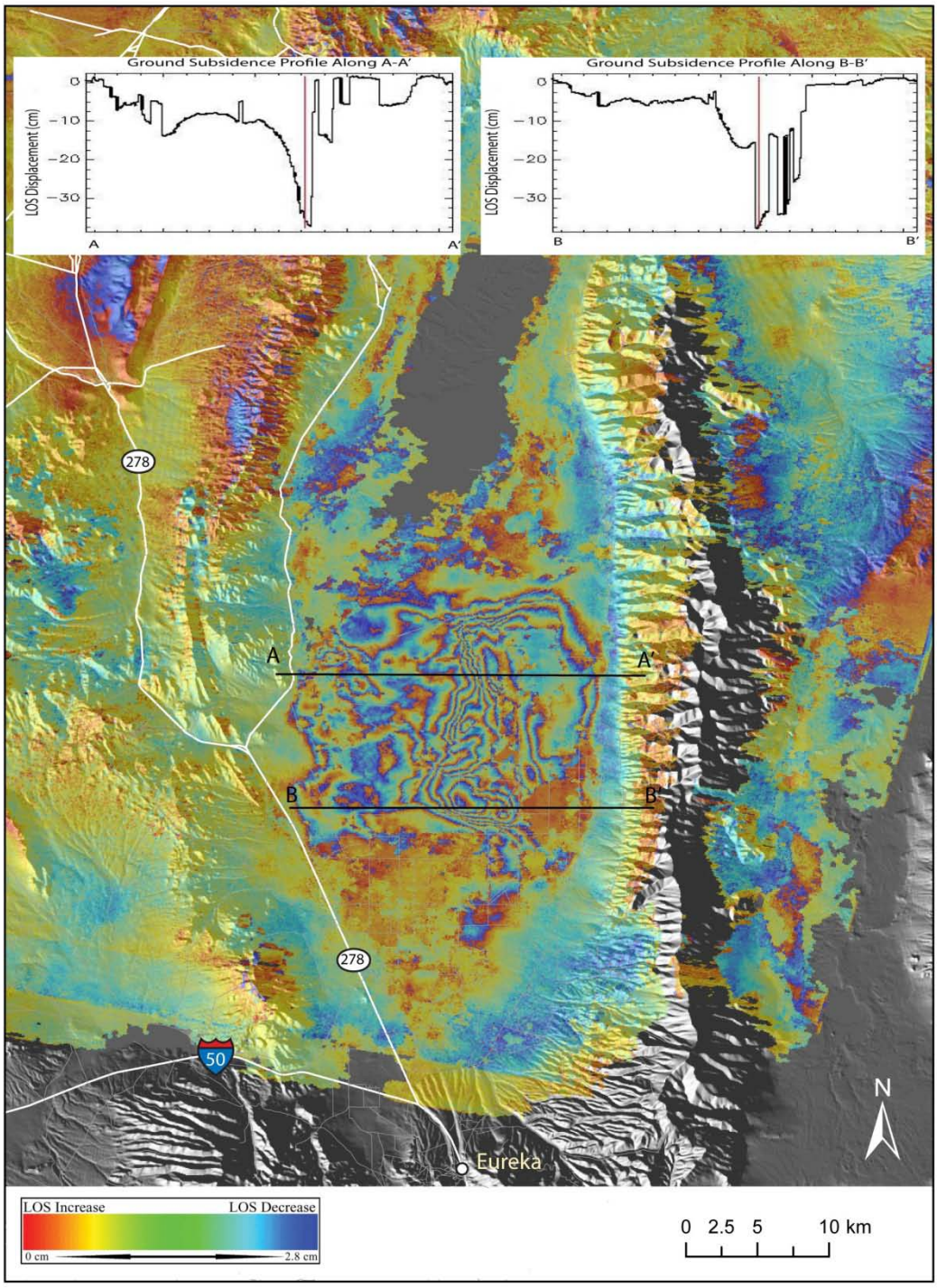

Figure 5.7 Unwrapped stacked interferogram covering the time period of June 17, 1992 – April 15, 2000. Each red-yellow-blue color cycle (fringe) represents approximately 3 cm of LOS change. The profiles show LOS change along the lines (A-A' and B-B') in the figure. A negative change indicates subsidence during the time period.

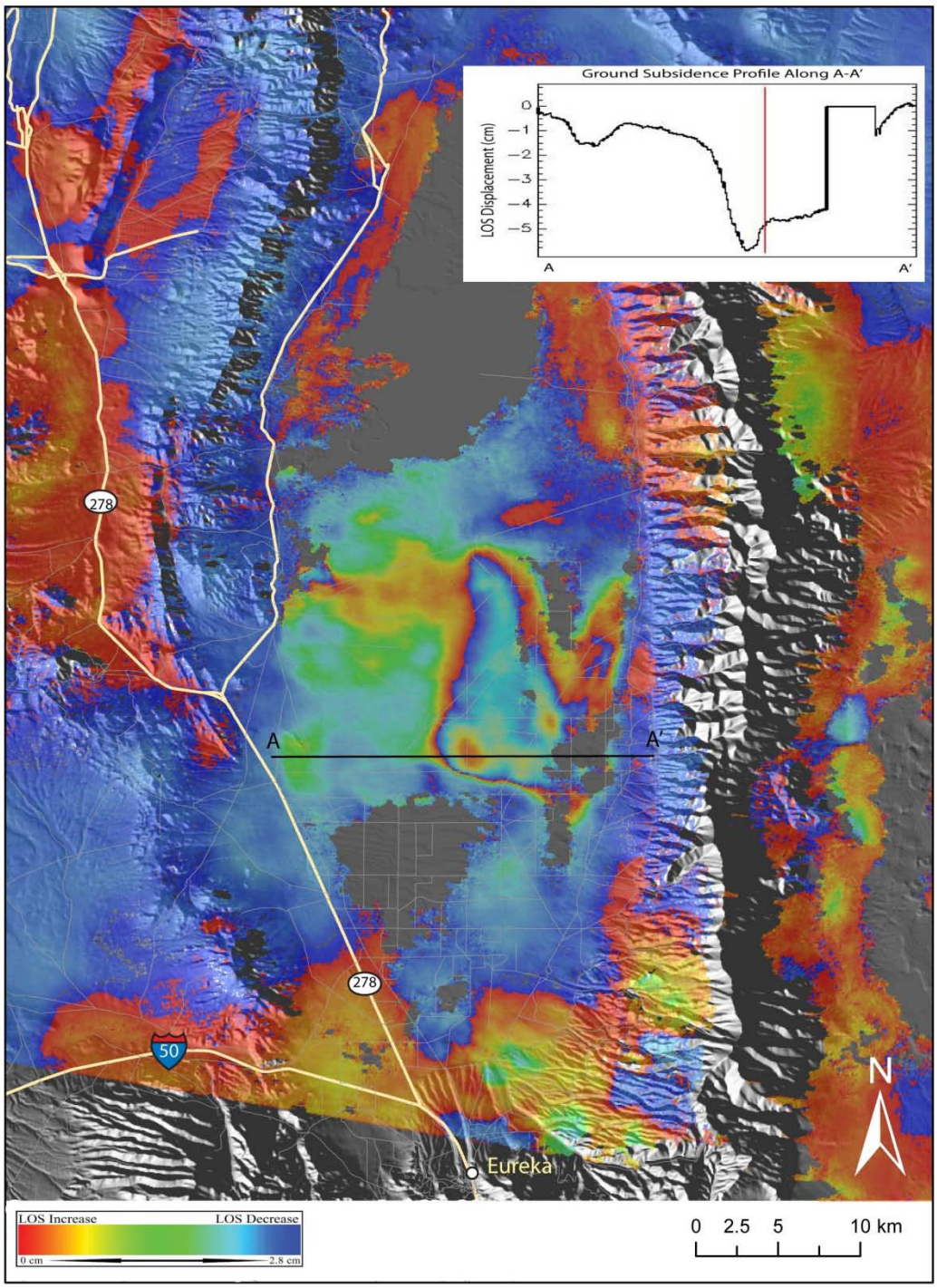

Figure 5.8 Unwrapped interferogram covering the time period of September 11, 2004 – November 5, 2005. Each red-yellow-blue color cycle (fringe) represents approximately 3 cm of LOS change. The profile at the upper right corner shows LOS change along the line (A-A') in the figure. A negative change indicates subsidence during the time period.

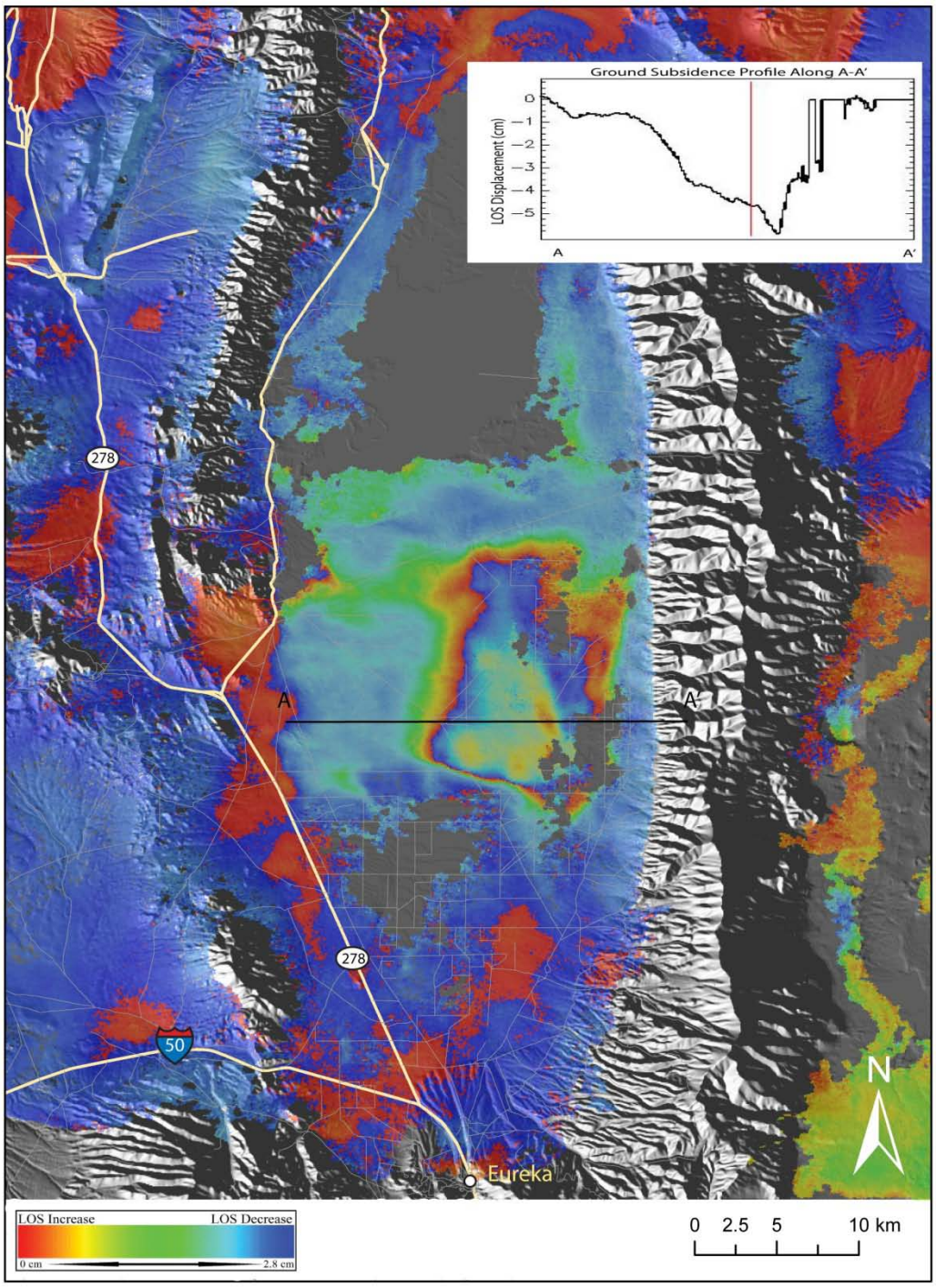

Figure 5.9 Unwrapped interferogram covering the time period of November 5, 2005 – December 30, 2006. Each red-yellow-blue color cycle (fringe) represents approximately 3 cm of LOS change. The profile at the upper right corner shows LOS change along the line (A-A') in the figure. A negative change indicates subsidence during the time period.

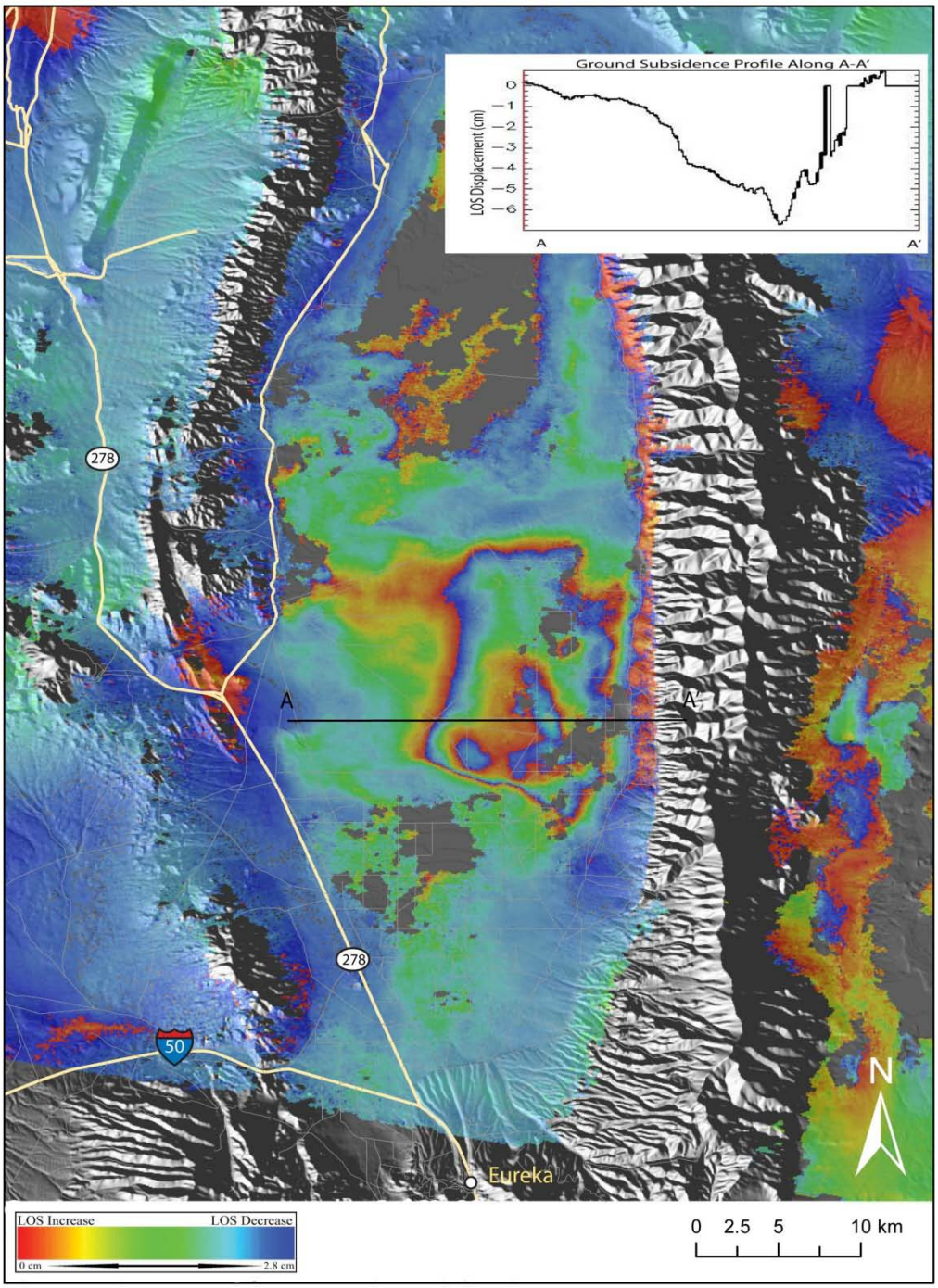

Figure 5.10 Unwrapped interferogram covering the time period of November 25, 2006 – December 15, 2007. Each red-yellow-blue color cycle (fringe) represents approximately 3 cm of LOS change. The profile at the upper right corner shows LOS change along the line (A-A') in the figure. A negative change indicates subsidence during the time period.

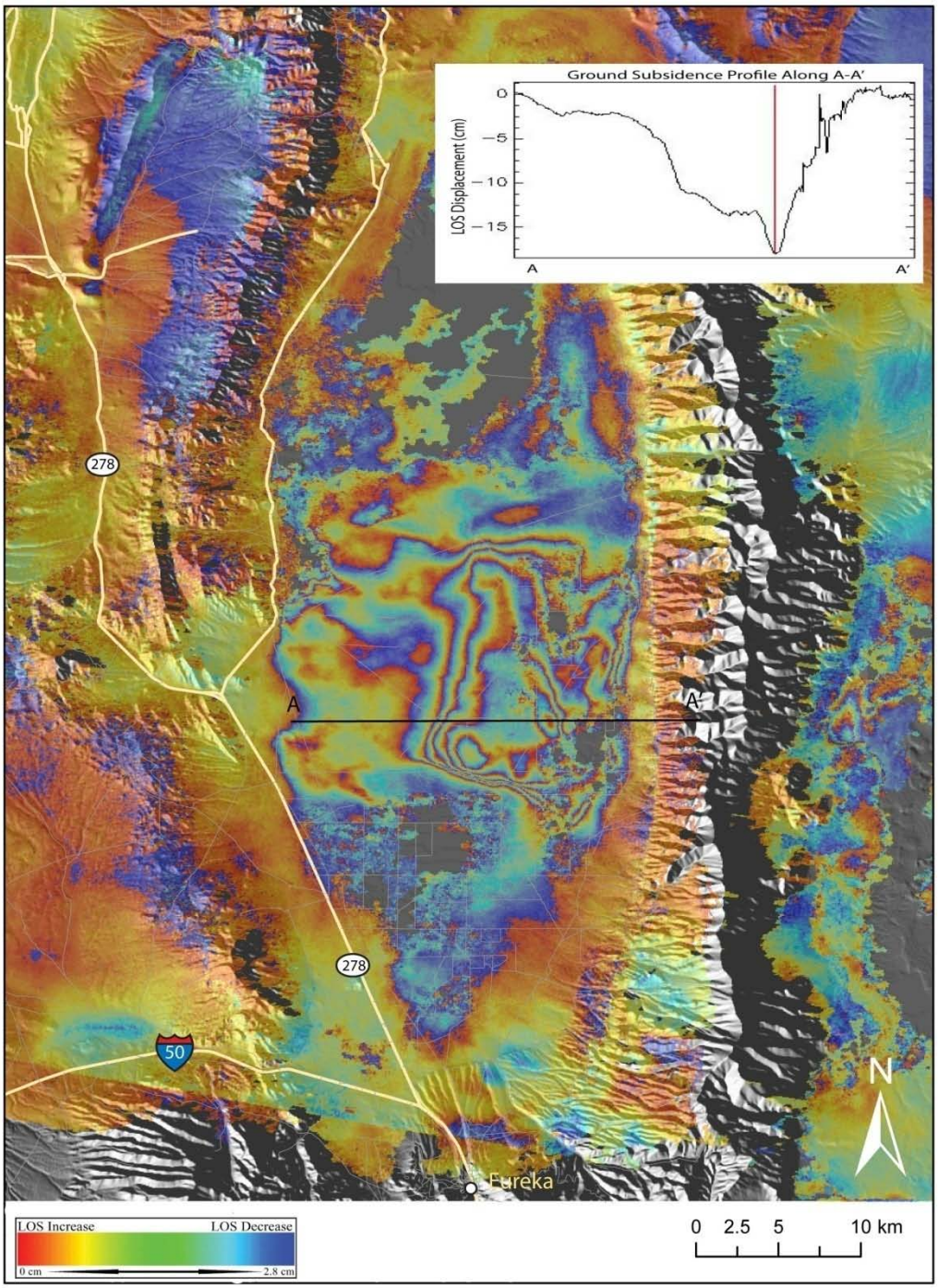

Figure 5.11 Unwrapped stacked interferogram covering the time period of September 11, 2004 – December 15, 2007. Each red-yellow-blue color cycle (fringe) represents approximately 3 cm of LOS change. The profile at the upper right corner shows LOS change along the line (A-A') in the figure. A negative change indicates subsidence during the time period.

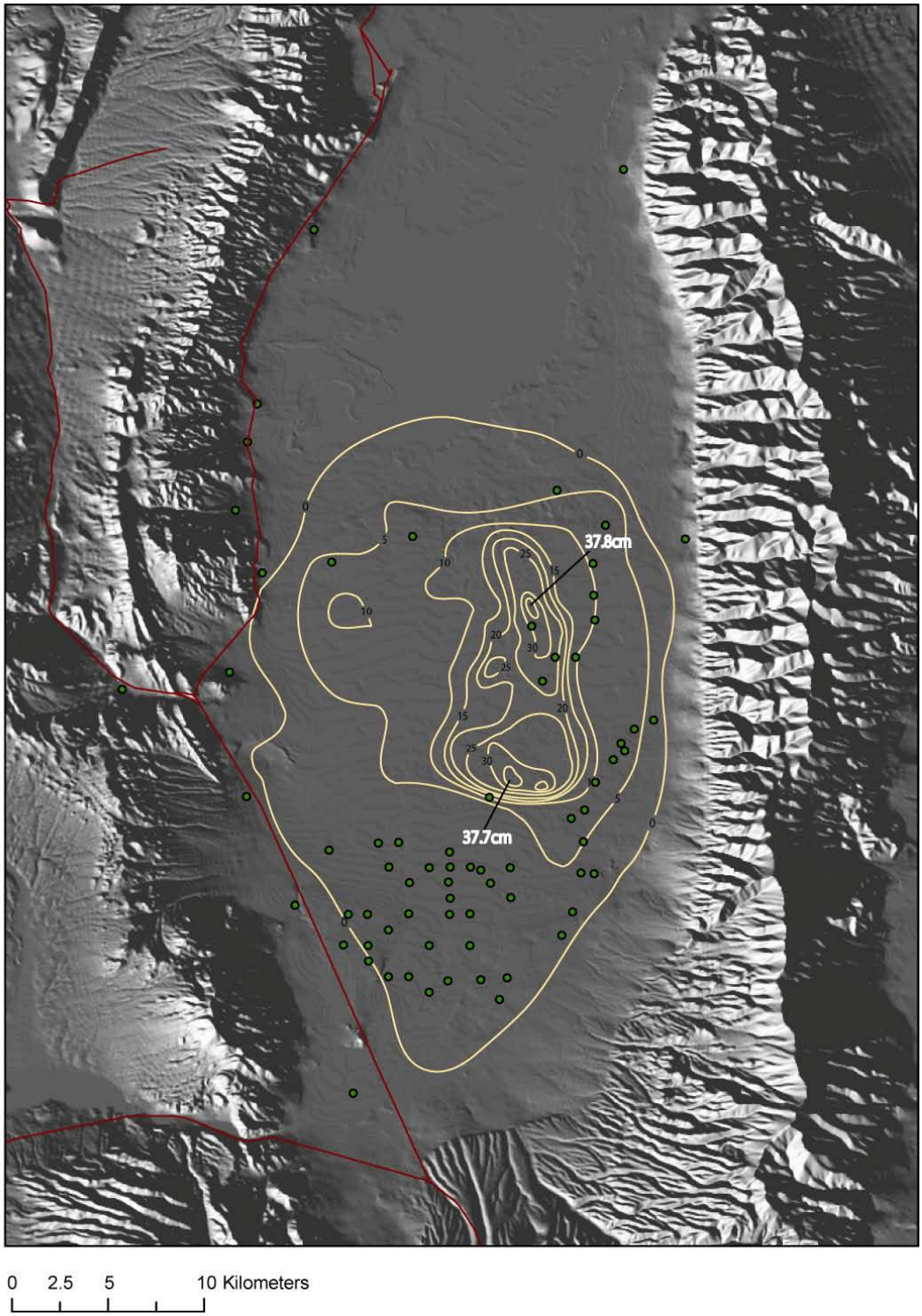

Figure 5.12 Ground subsidence contours in time period of June 17, 1992 – April 15, 2000 generated from the ERS-1/ERS-2 stacked interferogram. Green circles represents the existing wells. The subsidence values obtained here are based on the number of fringes (red-yellow-blue color sequence).

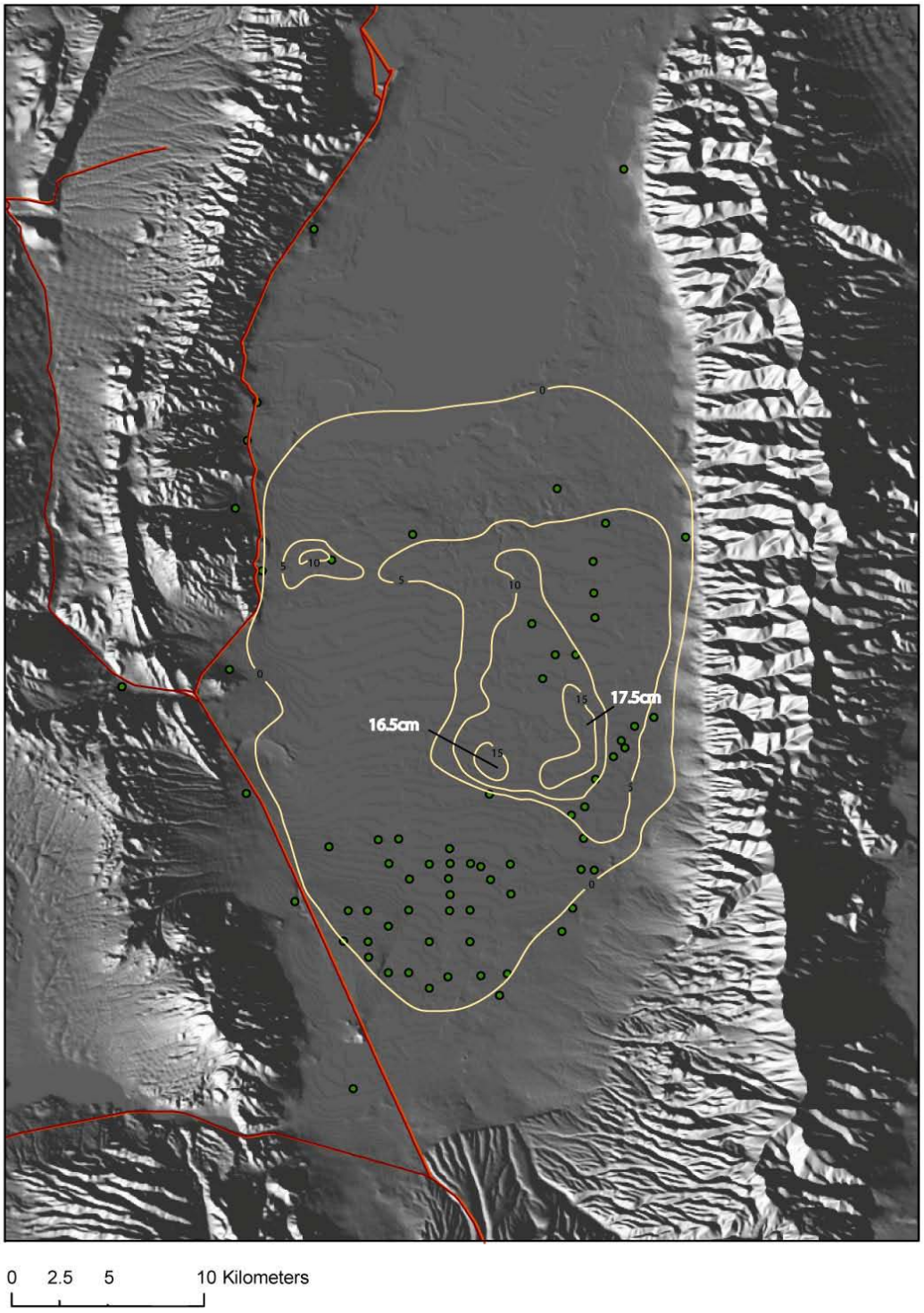

Figure 5.13 Ground subsidence contours in time period of September 11, 2004 – December 15, 2007 generated from the Envisat stacked interferogram. Green circles represent existing wells. The subsidence values obtained here are based on the number of fringes (red-yellow-blue color sequence).

Chapter 6

Water Table Drawdown and Correlation with Subsurface Materials and InSAR Analysis in the South Diamond Valley

This section outlines the water table drawdown with time, the distribution of the subsurface lithology in the south part of the valley, and the correlation with InSAR analysis.

In order to understand the aerial extent and the magnitude of ground subsidence, the overall distribution of clay, sand and gravel in the subsurface combined with the water table drawdown characteristics were analyzed.

6.1 Well-Number Systems

Two different designations were used for identifying wells: the USGS local well number and the Nevada log number. For the USGS local well number, wells are identified and numbered according to their location in the Township and Range rectangular system for the subdivision of public lands referenced to the Mount Diablo baseline and meridian. Identification consists of four units separated by spaces; the hydrographic area number, the township number preceded by an N to indicate location north of the baseline; the range number preceded by E to indicate location east of the meridian; and the section number plus letters (A, B, C, and D) designating quarter section, quarter-quarter section, and so on. Figure 6.1 shows the well location for a local well number, 153 N22 E54 18CADD. The number 153 is the hydrographic area number

for the Diamond Valley and the first site recorded in the southeast quarter, of the southeast quarter, of the northeast quarter, of the southwest quarter of section 18, Township 22 North, Range 54 East, Mount Diablo baseline and meridian.

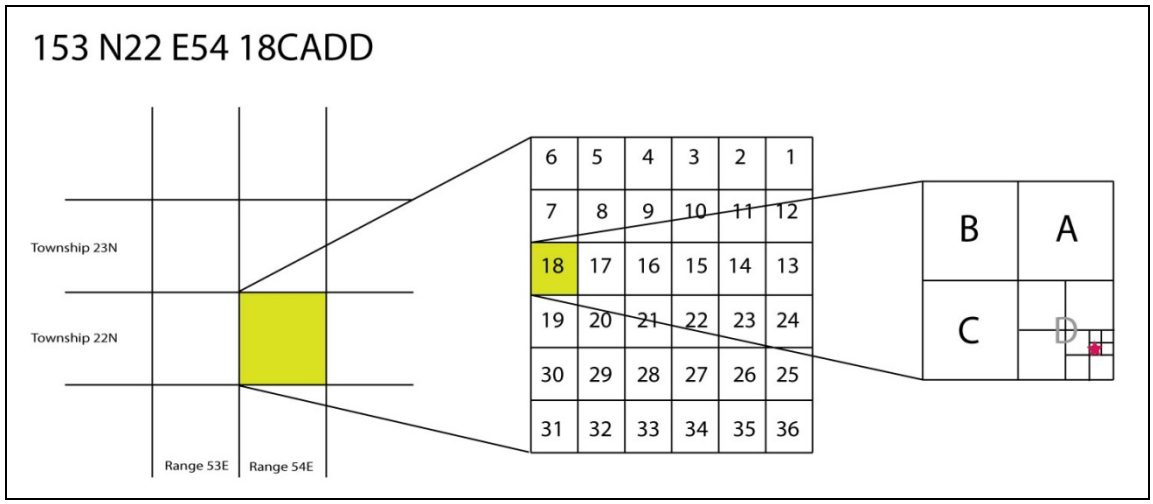

Figure 6.1 Example of locating a well by a USGS local well number.

The Nevada log number is assigned by the Nevada Division of Water Resources after the well is completed and the log is filed. The Nevada log numbers are used to describe drillers' logs for water wells which were used to determine the lithologic distribution of subsurface materials.

6.2 Water Table Drawdown Due to Groundwater Withdrawals

Water levels in the Diamond Valley have changed over time as a result of groundwater withdrawals for irrigation. According to Arteaga et al. (1995), the irrigated area expanded from 3,200 acres in 1961 to 22,200 acres in 1990. In the early development, Harrill (1968) estimated total pumpage to be 12,000 acre-ft in 1965 and 50,000 acre-ft for 1950–65. Between 1972 and 1990, annual pumpage of ground water

for irrigation increased from 23,000 to 64,000 acre-ft (Arteaga et al, 1995) in Diamond Valley.

In 1961, there were 85 irrigation wells in Diamond Valley and more than 200 irrigation wells had been drilled by 1965 (Harrill, 1968). Periodic measurements of the water level by U.S. Geological Survey are made at approximately the same times in each year to reduce seasonal effects. In 1990, there were 158 irrigation wells in use among 291 existing wells, and the largest water table decline measured was more than 50 ft, which was recorded in the developed areas of southern Diamond Valley (Arteaga et al, 1995). In 2005, the water table elevations of 87 irrigation wells were measured in Diamond Valley by the USGS (Tumbusch and Plume, 2006). The water table decline contour map in southern part of the valley (Figure 6.2) was created using water table elevation data from 1965 and 2005 from 67 irrigation wells.

Water table elevations from 1965 to 2006 for selected irrigation wells were analyzed to determine the rate of drawdown from the data sets obtained from Interflow Hydrology (2009). The wells were selected on the basis of their locations and are located in an area of intense ground subsidence recorded by InSAR permitting any correlation between the water table drawdown and the ground subsidence to be determined. The water table elevation at each well is plotted (Figure 6.3) using the same plot parameters in order to make them visually comparable.

The largest water table drawdown, approximately 70 feet, occurred at well #7 (153 N21H E54 32DCCC). Water table plots of wells #5 (153 N22 E54 27CAB) and #6 (153 N22 E54 28DCCC) show a maximum drawdown of 65 and 66 feet respectively. As well location moves northwards, moving away from the active irrigating area, the water

table drawdown value decreases from 44 feet at well #4 (153 N22 E54 18CADD), 39 feet at well #3 (153 N22 E54 6CCCC), 30 feet at well #2 (152 N23 E54 30DDDD), and to 29 feet at well #1 (153 N23 E54 29CDDD), as indicated from the contour lines of Figure 6.2.

It is interesting to note differences between plot characteristics of the larger drawdown wells (#5, #6, and #7) and those of the smaller drawdown wells (#1-#4). While the rates (the slopes of a plot) of well #5, #6 and #7 are approximately constant through the time until the present, that of wells #1 through #4 changes over the time. The rate between 1975 and the late 1980's is highest for these four wells, and it may indicate that for this time period the water table experienced the fastest decline over the recorded history. After this period the water table at these four wells recovered in the late 1990's.

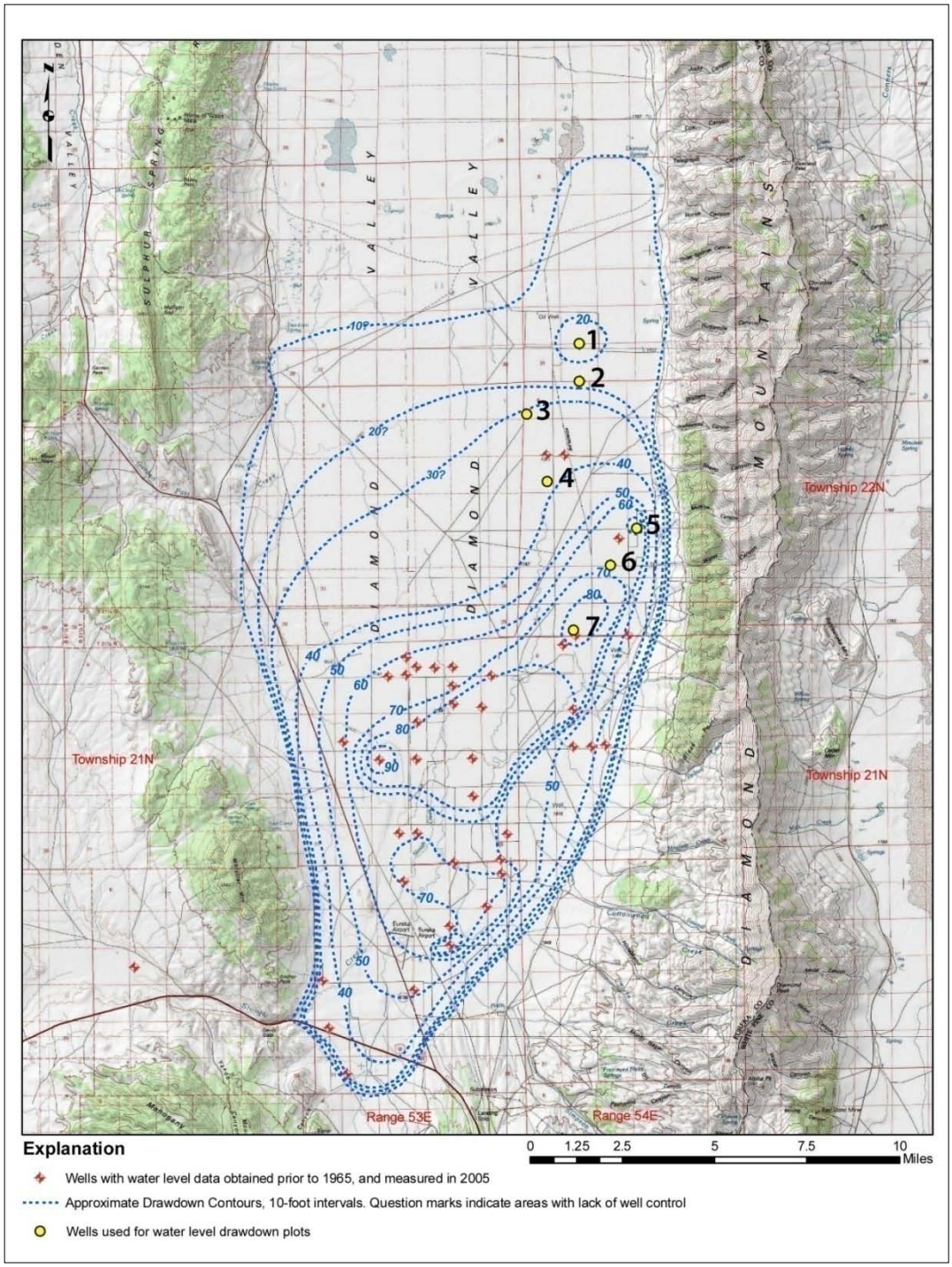

Figure 6.2 Water table contour map for irrigation wells in the southern Diamond Valley. Each yellow circle with a number represents a location of the well analyzed the water table drawdown rate. (Modified from Interflow Hydrology, 2009)

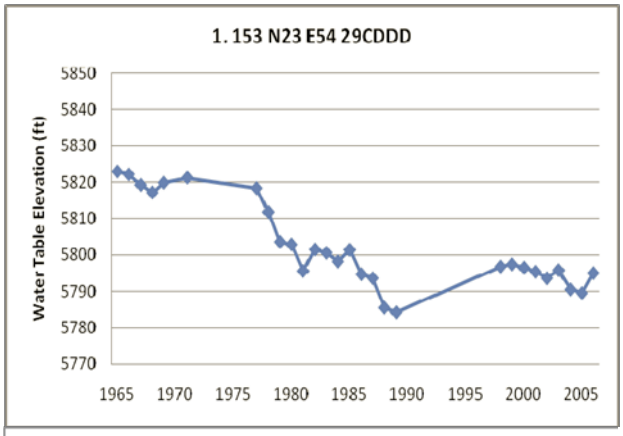

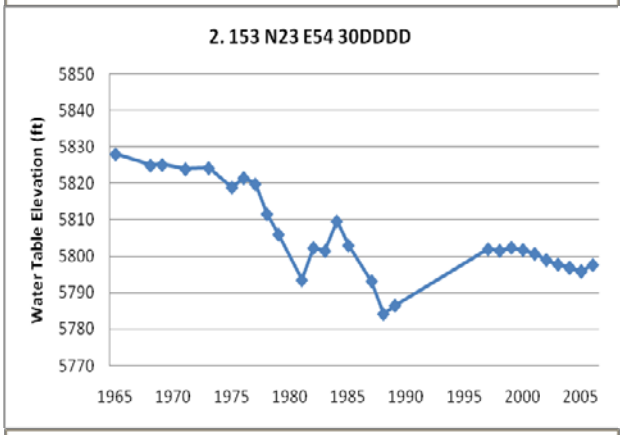

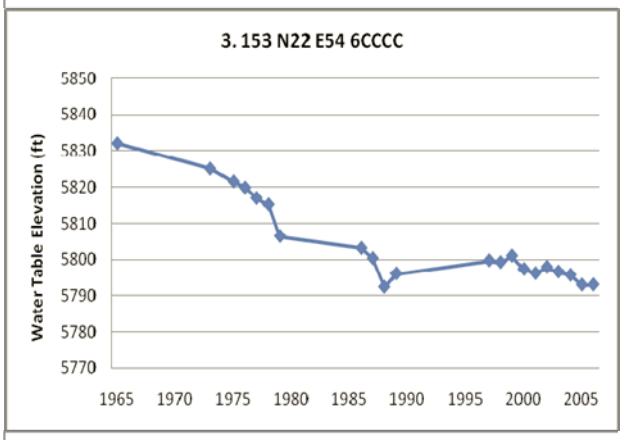

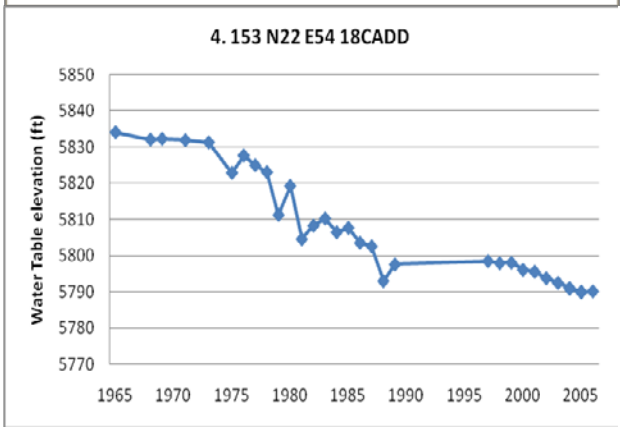

Figure 6.3 Water level elevation plots for selected seven wells for the time period of 1965-2006. Locations shown in Figure 6.2. (see Appendix II for data set)

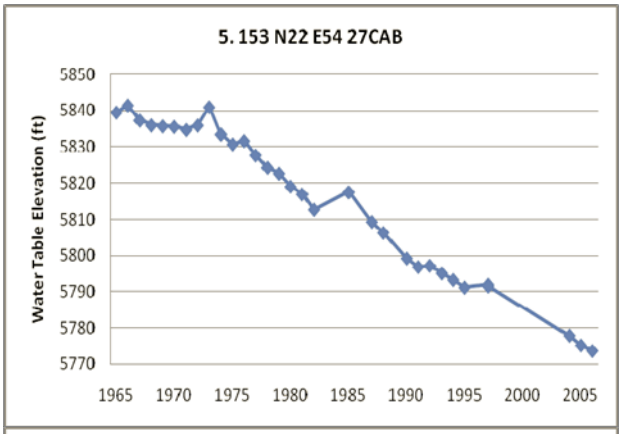

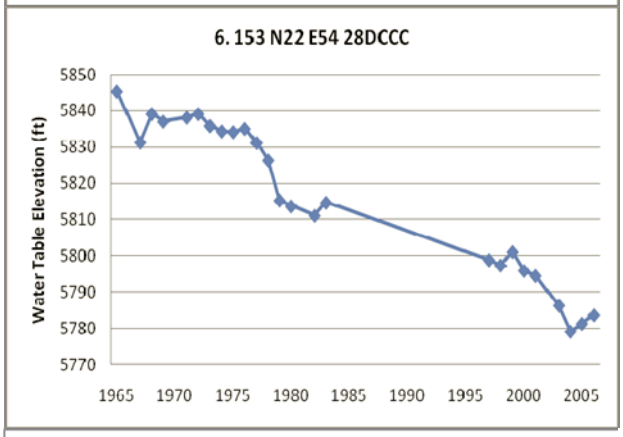

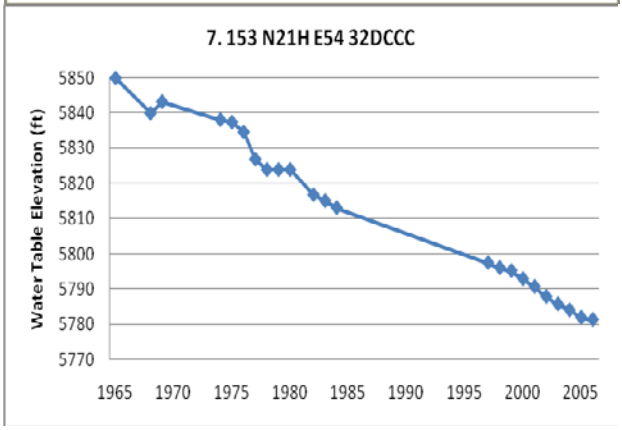

Figure 6.3 continued.

As stated in Chapter 4 (Section 4.1.3), the bulk elastic and inelastic skeletal storage coefficients in an aquifer-system can be estimated by utilizing the change in aquifer-system thickness or compaction (Δb) and the change in hydraulic head (ΔH). In this study Δb is the LOS displacement (assumed to be vertical) determined from InSAR results, and the change in effective stress ($\Delta \sigma_e$) is reflected by water-level change (ΔH). Three locations were selected for obtaining the magnitude of subsidence and water level data from available information.

Since there is a time gap of approximately four years between ERS and Envisat InSAR coverage, estimation of cumulative subsidence for 1992-2007 period was made by extrapolating the ERS time series rates through the four year data gap. Figure 6.4 a-c show the subsidence rates for three locations of water wells between 1996-2007. Table 6.1 summarizes estimations of the bulk skeletal storage coefficients of the sites.

Figure 6.4 Cumulative subsidences for three water wells. The subsidence data are extrapolated (dashed line) in order to estimate the total 1996-2007 subsidence. The blue lines are annual water level data since 1996. (a. Well #3, b. Well #4 and c. Well #7)

a.

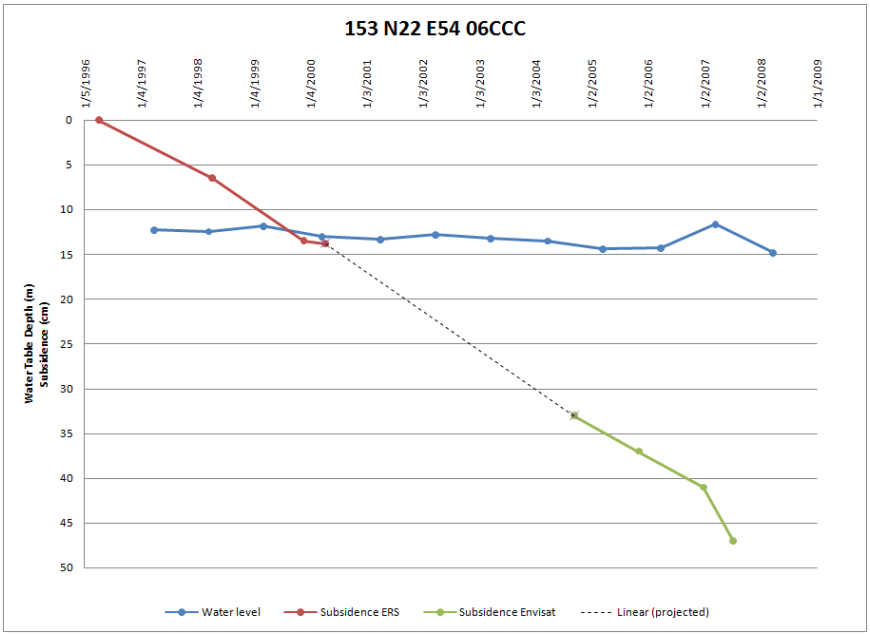

Figure 6.4 continued.

b.

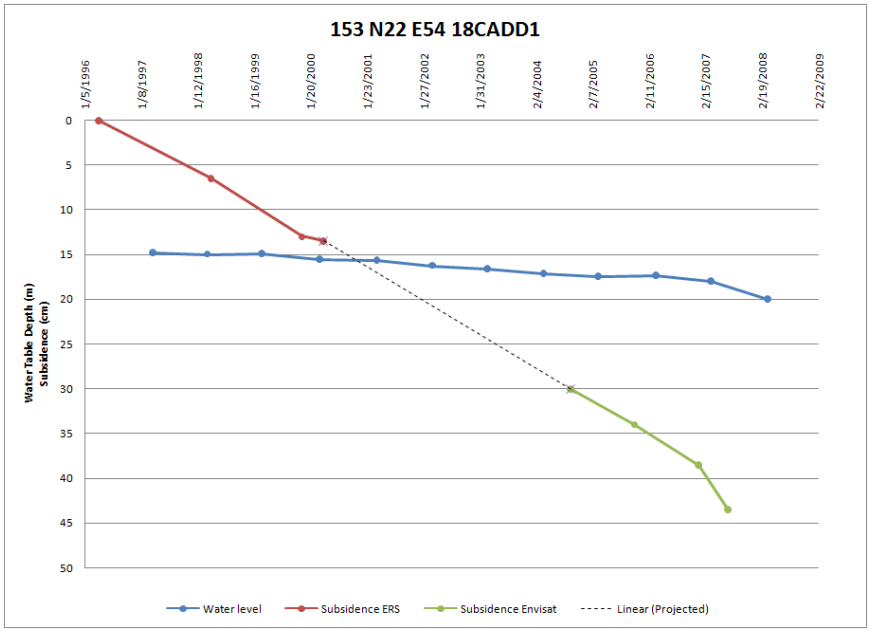

c.

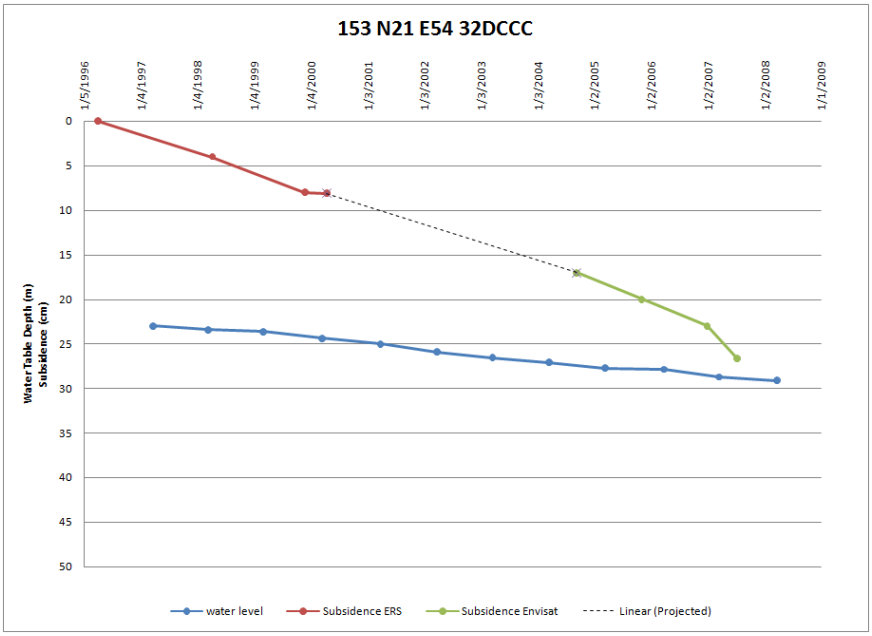

Table 6.1 Summary of estimations of the bulk skeletal storage coefficients for the locations, well #3(153 N22 E54 6CCCC), #4(153 N22 E54 18CADD) and #7(153 N21H E54 32DCCC).

	Subsidence, Δb (cm)	**Head change, ΔH (m)**	**Storage coefficient (S^*_k)**
Well #3	47.0	2.54	1.85×10^{-1}
Well #4	43.5	5.20	8.37×10^{-2}
Well #7	26.7	6.16	4.33×10^{-2}

6.3 Analysis of Subsurface Materitals

The subsurface distribution of clay, sand and gravel in Diamond Valley was made by analyzing drillers' log data of water wells available from the Nevada Division of Water Resources website. Analysis was made of the distribution of subsurface materials from each well log, with depths ranging from 200 feet up to 500 feet. A total of 34 logs was utilized (Appendix III), selected on the basis of their location and clarity of imformation.

Any information derived from logs is subject to certain limitations. The major difficulty in assessing material distribution is the lithologic interpretation made by the well driller. A lithologic description for the log is initially made by the driller and contains his/her interpretation. Some differences were apparent in observing and selecting drillers' log data such as some logs were in feet scale, and other were in deca-feet scale. An interpretation must then be made of the drillers' lithologic description to reduce them to suitable terms for comparison and analysis for this study. The interpretation used in this study is based on that used by Harrill (1968) and is summarized in Figure 6.4. Drillers' lithologic descriptions were categorized into three lithologic

groups: sand and gravel, clay, and a mixture of clay, sand and gravel. Harrill (1968) estimated the percentage of clay in a mixed material, this study focused on the distribution and amount of clay layers, as a clay layer plays a critical role in soil compaction (Chapter 4). The sum of all interpretations represents overall conditions with a reasonable degree of accuracy, and is supported by the fact that results obtained from logs show a good agreement with adjacent logs. The locations of selected logs are shown in Figure 6.5 with the estimated percentage of the three groups.

Drillers' description	Geologic interpretation	Estimated composition	Percentage of sand, gravel or both
Gravel	Gravel	100% gravel	100
Sand and gravel	Interbedded layers of medium to coarse-grained sand and gravel	50% sand 50% gravel	100
Sand, gravel, and clay Gravel and clay, cemented gravel	(1) Pebbles in a matrix of sand, silt, and clay, matrix is indurated in the case of cemented gravel (2) Interbedded layers of sand, gravel, and clay	20% gravel 20% sand 60% silt and clay	40
Sand	Fine, medium, or coarse-grained sand	100% sand	100
Sand and clay, sandy clay	Interbedded layers of medium-grained sand, silt, and clay	30% sand 70% silt and clay	30
Clay, silt, mud, muck	Interbedded silt and clay in varying proportions	0 to 100% clay 0 to 100% silt	0

Figure 6.5 Geologic interpretations and estimated compositions from materials described in drillers' logs. (Harrill, 1968)

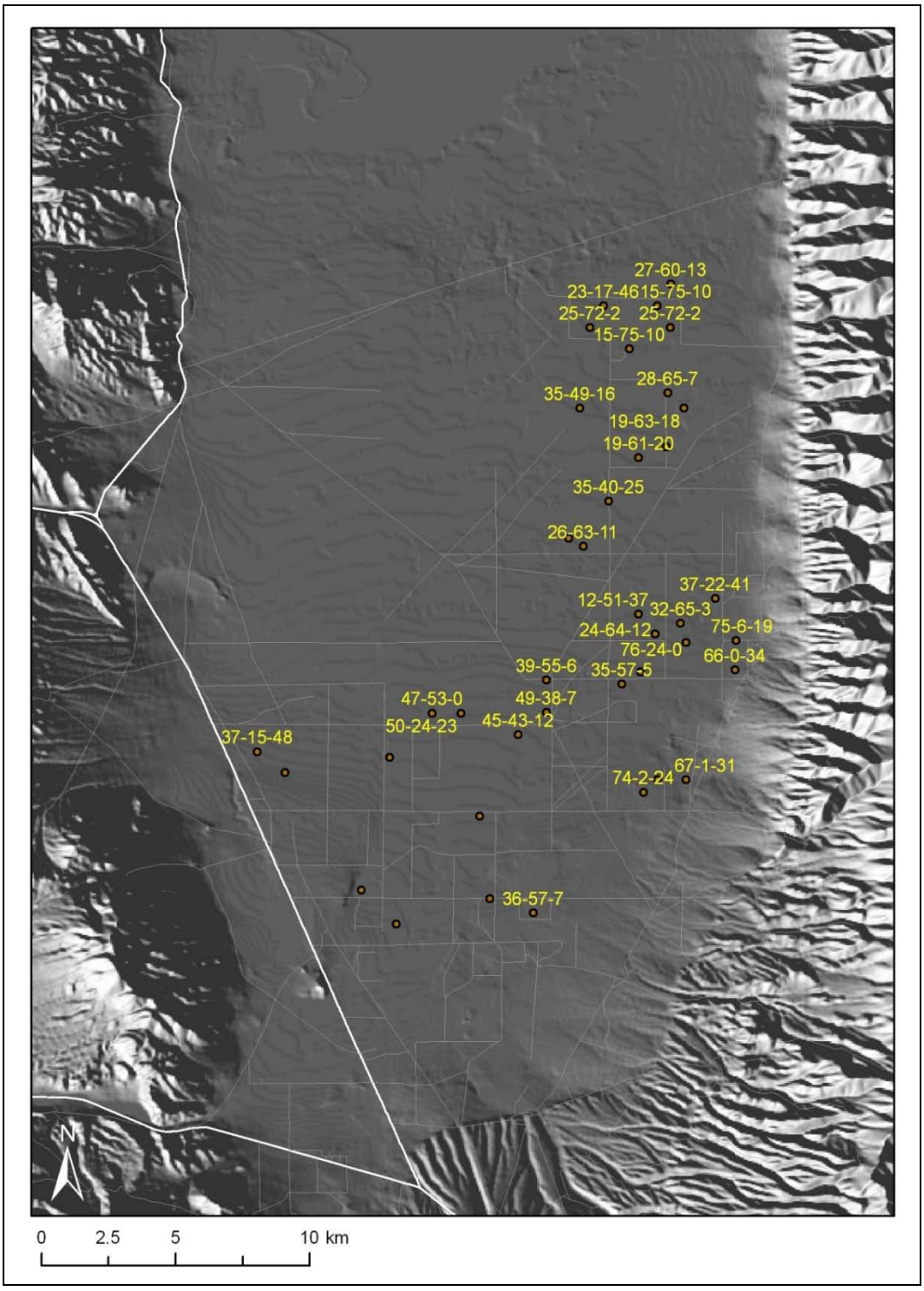

Figure 6.6 Locations of selected drillers' logs and the percentage of the three litholigic groups. Three numbers connected with huphens indicate the estimated proportion in order of "sand and gravel – clay – mixture of clay, sand and gravel". (see Appendix III for data sets and the analysis)

6.4 Correlation between subsidence characteristics and subsurface analysis

Detailed ground subsidence characteristics from InSAR resuls (Chapter 5) are analyzed in order to determine any correlations with the subsurface conditions. InSAR results show very detailed ground displacement with time. Detecting the aerial extent of the subsidence area and the magnitude over time also enabled this study to understand the average rate of subsidence from the maximum magnitude divided by the time period between two data acquisition dates. The results of the stacked interferograms discussed in Chapter 5 are compared to the water table drawdown features and the subsurface materials, over the same time period.

The subsidence profiles obtained from the ENVI program, the water table drawdown profiles, and well logs were compared. Although the water table elevation plots show detailed water table change histories (Section 6.2), the water table contour map was utilized for a comparison in this analysis as it is normalized and easier to visualize its feature. Subsurface materials estimated from the drillers' logs were visualized as virtual borehole logs in the cumulative percentage of the three lithologic groups. The virtual boreholes were then used to make a model of the subsurface lithologic distribution along a cross section.

Figure 6.6 is the ERS stack interferogram covering the time period June 17, 1992 – April 15, 2000 with the water table drawdown contour lines and the borehole locations. Two east-west cross sections (H_A-H_A' and H_B-H_B') and one north-south cross section (V-V') were constructed. The cross section H_A-H_A' runs through the area where the maximum subsidence was calculated, and Figure 6.7-a shows a relatively constant clay percentage and a small water table drawdown. The cross section H_B-H_B' also runs

through the area where the maximum subsidence was detected, and Figure 6.7-b shows the subsurface model which correlates to the subsidence features. The subsurface lithologic model shows increasing clay percentage towards the east where the greatest subsidence occurs. The north-south cross section (Figure 6.7-c) runs through the two maximum subsidence areas and also represents some correlation between the subsidence features and the subsurface lithologic model.

Figure 6.8 is the Envisat stack interferogram covering the time period of September 11, 2004 – December 15, 2007 with the water table drawdown contour lines and the borehole locations. An east-west cross section (H-H') and a north-south cross section (V-V'), which both run though the maximum subsidence area, were also constructed. The cross section H-H' (Figure 6.9-a) shows an increase in clay percentage in the model which correlates to the subsidence. The subsurface lithologic model also shows increasing clay percentage towards the east as observed in the cross section H_B-H_B' in the ERS interferogram. The north-south cross section (Figure 6.9-b) also shows some correlation between the subsidence values and clay amount in the model. A very small amount of clay is modeled just off the subsidence signal with the clay percentage dramatically increasing towards the signal.

The subsurface lithologic models in the two interferogram stacks also helped to understand the relationship between the calculated subsidence and the subsurface lithology. The vertical cross section from the ERS interferogram runs approximately 4km west of the Envisat interferogram, and the model shows more clay percentage in its entire section compared to the Envisat model. It reveals that, for the ERS subsidence signal, the magnitude of subsidence is higher in the area with the higher clay percentage. This fact

shows that the larger the amount of clay in an aquifer, the greater the amount of ground subsidence due to ground water withdrawal.

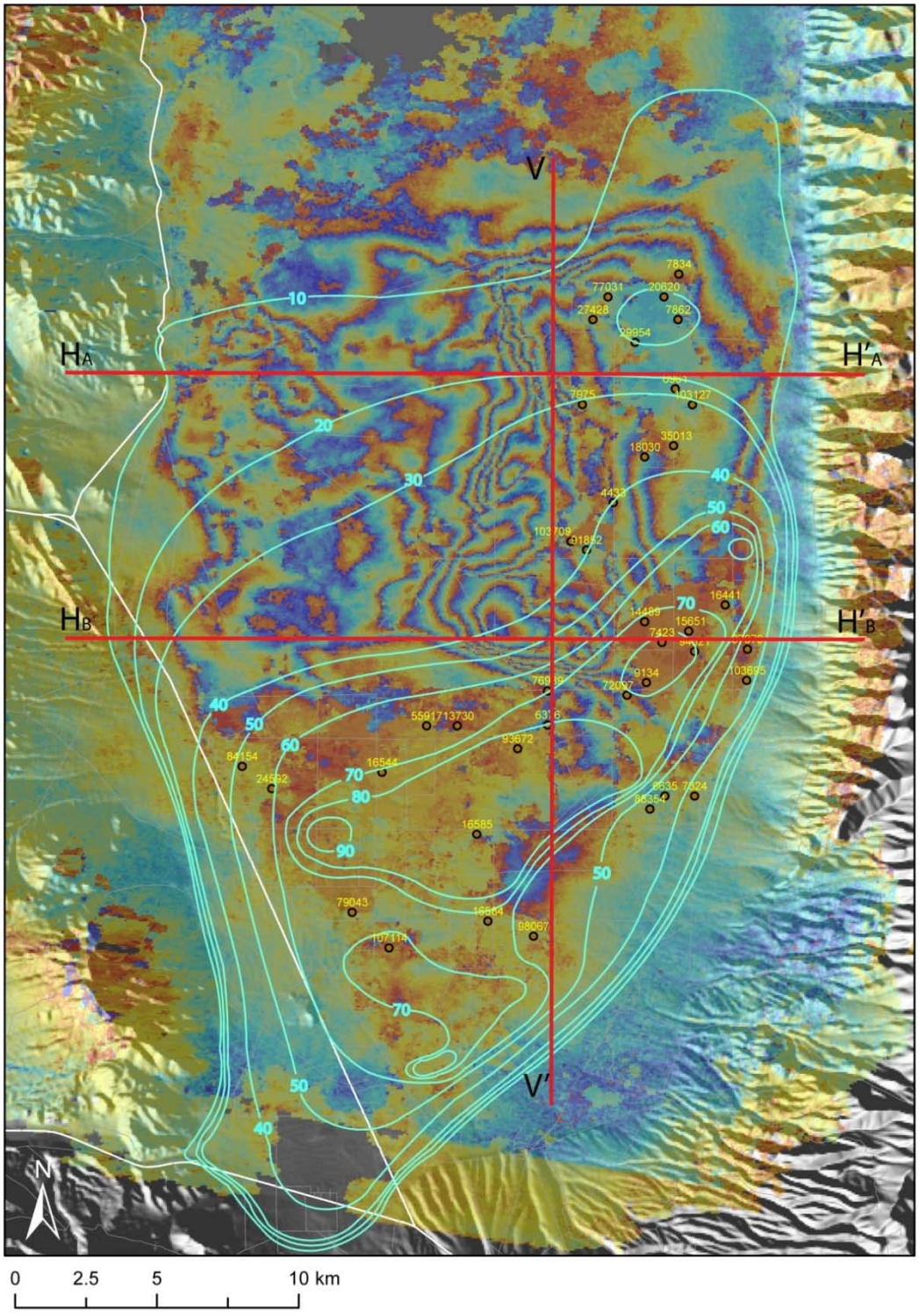

Figure 6.7 ERS stacked interferogram covering the time period of June 17, 1992 – April 15, 2000 showing the locations of cross sections. The light blue lines with numbers represent the approximate water table drawdown in feet. Circles with numbers show locations of the borehole logs.

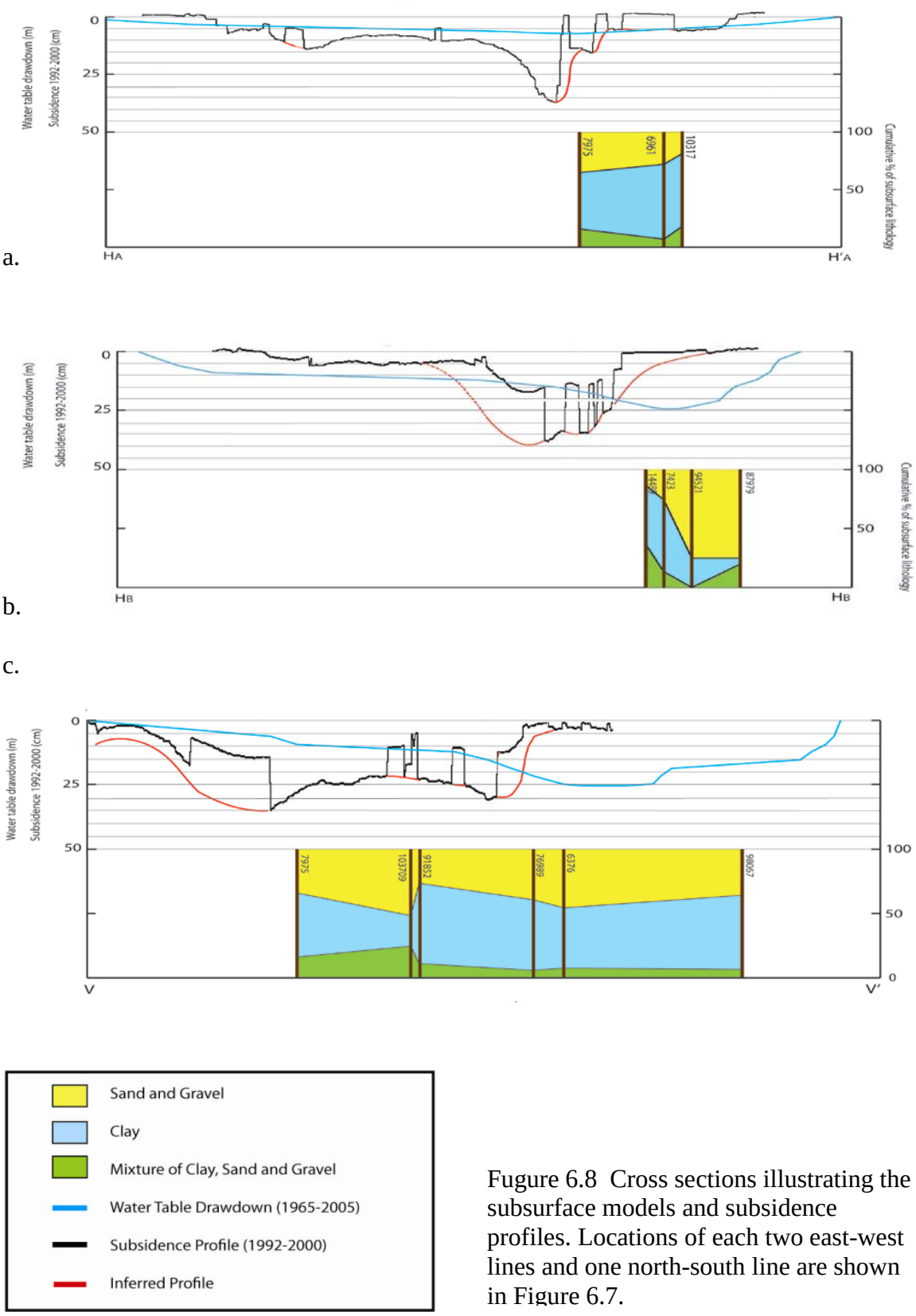

Fugure 6.8 Cross sections illustrating the subsurface models and subsidence profiles. Locations of each two east-west lines and one north-south line are shown in Figure 6.7.

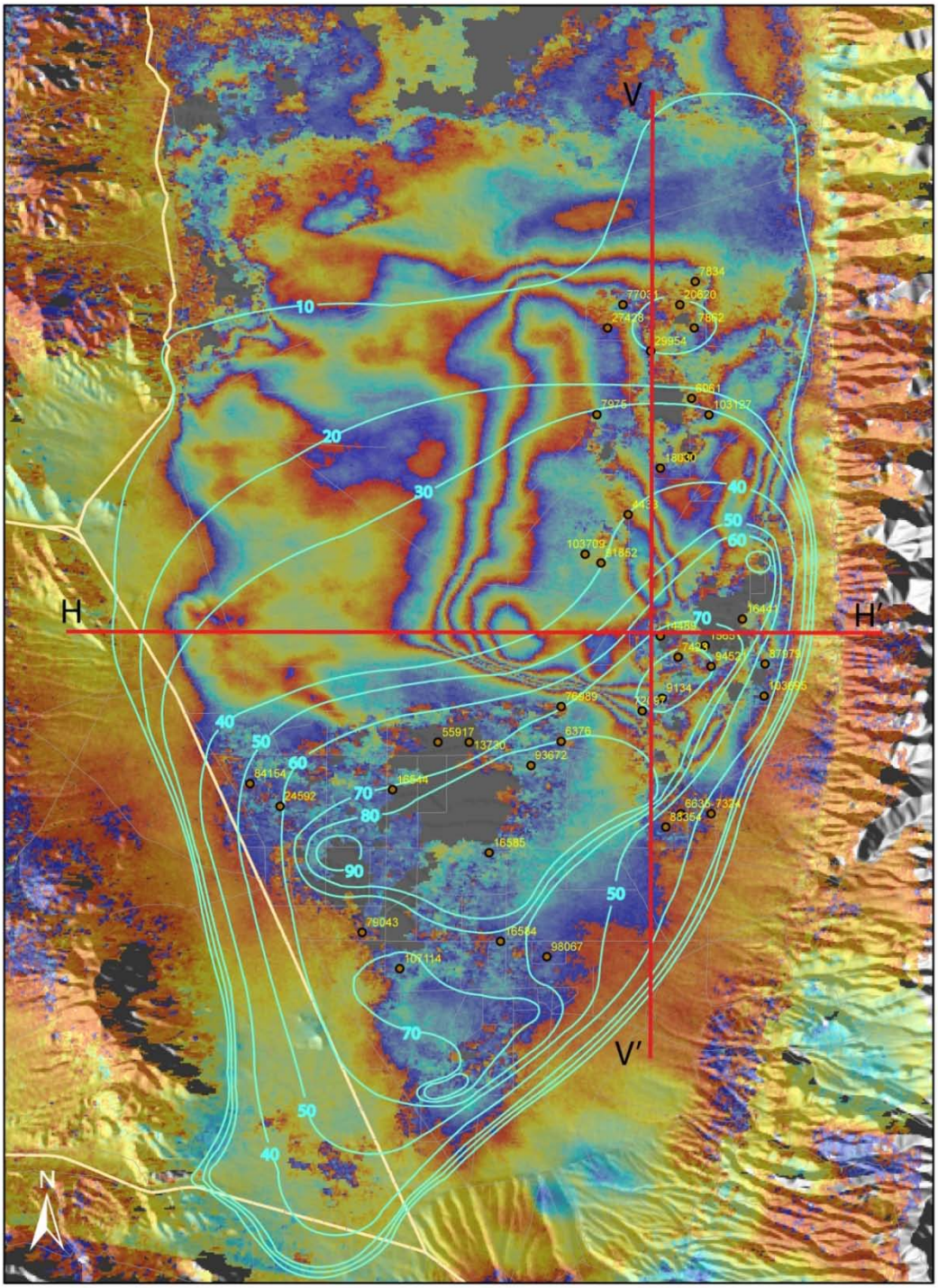

Figure 6.9 Envisat stacked interferogram covering the time period of September 11, 2004 – December 15, 2007 showing the locations of cross sections. The light blue lines with numbers represent the approximate water table drawdown in feet. Circles with numbers show locations of the borehole logs.

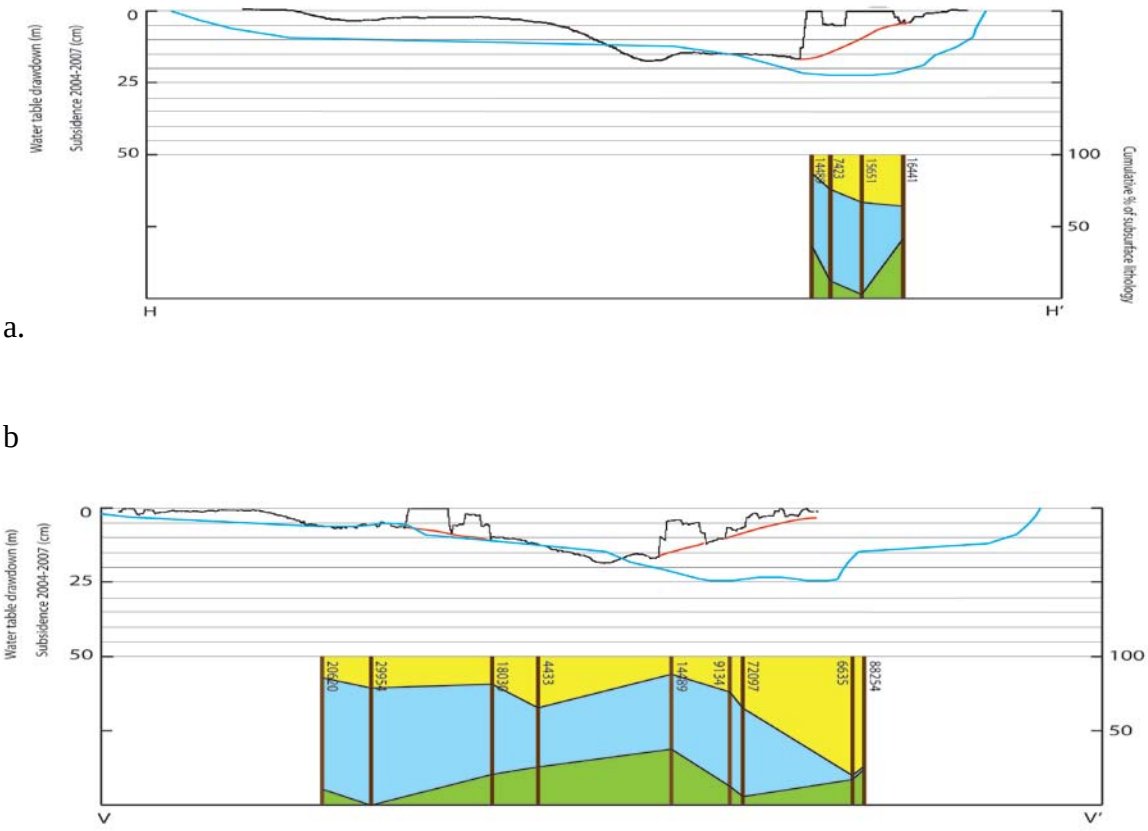

Fugure 6.10 Cross sections illustrating the subsurface models and subsidence profiles. Locations of each east-west lines and one north-south line are shown in Figure 6.9.

Chapter 7

Conclusions

Interferometric synthetic aperture radar (InSAR) has great potential to detect and quantify ground subsidence caused by aquifer system compaction. In this study, InSAR mapped ground deformation signals with high spatial detail and resolution of displacement, developed in a groundwater basin in Diamond Valley, Nevada, using radar data collected from the ERS-1/ERS-2 and Envisat satellites. The site was suitable for the InSAR method as a result of the semi-arid climate, sparse vegetation, and the approximate flat valley basin. Deccorrelation was observed only in the area of agricultural activities and surrounding mountain ranges.

A total of 32 single interferograms with different time coverage permitted a detailed investigation of the deformation magnitude history over time, as well as a quantification of the areal extent of the signal. The maximum magnitude of the subsidence signals at the south part of the valley, where irrigation wells exist, were found to be 37.6 cm between July 17, 1992 and November 27, 1999 (obtained from ERS-1/ERS-2) and 17.5 cm between October 16, 2004 and December 15, 2007 (obtained from Envisat satellite data). These values may or may not represent the actual subsidence values because these are considered as minimum observed maximum subsidence values. The actual maximum subsidence may occur within the area of deccorrelation, which does not recover in the unwrapped interferogram.

The profile views of the subsidence signals assist in visualizing the deformation geometry even though they are highly exaggerated. The profiles show where gradual or

steep deformation occurred, and the overall complexity of the geometry indicates that the subsurface lithology can increase or decrease the deformation. The subsurface model estimated from the history of water table decline and the subsurface lithology distribution approximately correlate with the subsidence signals. Poor correlation occurred where limited availability of good subsurface data and limited spatial coverage of well logs existed.

InSAR is an excellent reconnaissance ground surveying tool for basins where other geodetic networks or extensometers are difficult to install or operate. In areas where radar coherency can be achieved for periods of months to years, InSAR will work in reconnaissance and monitoring of ground subsidence providing a high spatial detail. InSAR also could yield a considerable cost advantage over conventional surveys, where large-scale, high-density change detection is required such as urban area ground deformation.

References

Arteaga, F.E., Smith, J.L., and Harrill, J.R., 1995, Irrigated croplands, estimated pumpage, and water-level changes in Diamond Valley, Eureka and Elko Counties, Nevada, through 1990: U.S. Geological Survey Open-File Report 95–107, 68 p.

Bell, F.G., 1992, Engineering properties of soils and rocks, 3rd ed., Butterworth-Heinemann, p.296.

Bell J.W., and Price, J.G., 1991, Subsidence in Las Vegas Valley, 1980-91 – Final Project Report: Nevada Bureau of Mines and Geology, Open-File Report 93-4, 10 sect. 9 plates, scale 1:62,500.

Bell, J. W., Amelung, F., Ramelli, A., and Blewitt, G., 2002, Land subsidence in Las Vegas, Nevada, 1935-2000: New geodetic data show evolution, revised spatial patterns, and reduced rates, Environmental Engineering Geoscience, v. 8, no. 3, p.155– 174.

Bell, J.W., Amelung, F., Ferretti, A., Bianchi, M., Novali, F, 2008, Permanent scatterer InSAR reveals seasonal and long-term aquifer-system response to groundwater pumping and artificial recharge, Water Resources Research, v. 44, 18 p.

Bell, J.W. 2009, personal communication, Nevada Bureau of Mines and Geology.

Burbey, T.J., 1995, Pumpage and Water-Level Change in the Principal aquifer of Las Vegas Valley, 1980-90 – Nevada Division of Water Resources Information Report 34, 224 p.

Burgmann, R., Ferretti, A., Hilley, G.,Novali, F., 2006, Resolving vertical tectonics in the San Francisco Bay Area from permanent scatterer InSAR and GPS analysis, Geology, v. 34, no. 3, p. 221–224.

Das, B.M., 2006, Principles of geotechnical engineering, 6th ed., Thomson, p.312.

Dow, A., 2006, Earthquake: Keeping an eye out of change, using satellites to forecast earthquakes and volcanoes, Stanford Scientific Magazine http://www.stanford.edu/group/stanscimag/volume4-2/articles4-2/earthquakeForecast.html

Ferris, J.G., Kriowles, D.B., Brown, R.H., and Stallman, R.W., 1962. Theory of aquifer tests. U.S. Geological Survey, Water-Supply Paper 1 536-E.

Fowler, L.C., 1981, Economic consequences of land surface subsidence. Proc. American Society of Civil Engineering, J. Irrigation and Draining Division, pp. 151-159.

Franceschetti, G., Lanari, R., Synthetic aperture radar processing, 1999, CRC Press, Boca Raton, FL. p.167
Galloway, D.L., Hudnut, K.W., Ingebritsen, S.E., Phillips, S.P., Peltzer, G., Rogez, F., and Rosen, P. A., 1998, Detection of aquifer system compaction and land subsidence using interferometric synthetic aperture radar, Antelope Valley, Mojave Desert, California, Water Resource Reseach, v. 34, no. 10, pp. 2573-2585

Galloway, D.L., Jones, D. R., and Ingebritsen, S. (editors), 1999, Land Subsidence in the United States, USGS Circular 1182, 177 p.

Goldstein, R.M., Zebker, H.A., and Werner, C.L., 1988, Satellite Radar Interferometry: Two-Dimensional Phase Unwrapping, Radio Science, v. 23, no. 4, p. 713 – 720.

Gupta, R.P., Remote Sensing Geology, 2003, Springer-Verlag Pub. P367.

Harrill, J.R., 1968, Hydrologic response to irrigation pumping in Diamond Valley, Eureka and Elko Counties, Nevada, 1950-65: Nevada Department of Conservation and Natural Resources, Water Resources Bulletin 35, 85 p.

Hanssen, R.F., 2001, Radar Interferometry, Data Interpretation and Error Analysis, Kluwer Academic Publishers, 308 p.

Henderson, F.M., and Lewis, A.J., 1998, Principles & Applications of Imaging Radar, Manual of Remote Sensing, Third Edition, Volume 2. Published in cooperation with the American Society for Photogrammetry and Remote Sensing, John Wiley & Sons, Inc., 869 p.

Houghton, J.G., Sakamoto, C.M., and Gifford, R.O., 1975, Nevada's weather and climate: Nevada Bureau of Mines and Geology Special Publication 2, 78 p.

Hunt, R.E., 2007, Geologic hazards: a field guide for geotechnical engineers, p. 137.
Interflow Hydrology, 2009, Draft Environmental Impact Statement, Hydrogeology and Numerical Flow Modeling of the Mount Hope Area, Eureka County, Nevada

Interflow Hydrology, Cordilleran Hydrology, and Environmental Solutions, Inc., 2008, Hydrogeology and numerical flow modeling of the Mount Hope area, including Kobeh, Diamond, and Pine Valleys, Eureka County, Nevada: unpublished consultant's report prepared for General Moly, Inc.

Ireland, R.L., Poland, J.F., Riley, F.S., 1984, Land subsidence in the San Joaquin Valley, California, as of 1980. USGS professional Paper, Report: P 0437-I, pp.I1-I93.

Jacob, C.E., 1940. On the flow of water in an elastic artesian aquifer. American Geophysical Union Transactions Part 2, 574-586.

Leake, S.A., 2004**,** Land Subsidence from groundwater pumping, U.S.Geological Survey and U.S.Department of Interior Report.
Lehner, R.E., Tagg, K.M., Bell, M.M., and Roberts, R.J., 1961, Preliminary geologic map of Eureka County, Nevada. U.S. Geological Survey Mineral Inv. Field Studies Map. MF-178.

Mabey, D.R., 1964, Gravity map of Eureka County and adjoining areas, Nevada. U.S. Geological Survey Geophysical Inv. Map GP-415.

Massonnet, D., Rossi, M., Carmona, C., Adrangna, F., Peltzer, G., Feigl, K., Rabaute, T., 1993, The displacement field of the Landers earthquake mapped by radar interferometry, Nature, v. 364.

Massonnet, D., Briole, P. and Arnaud, A., 1995, Deflation of Mt. Etna monitored by spaceborne radar interferometry, Nature, v. 375, p. 567 – 570.

Meinzer, O.E., 1928, Compressibility and elasticity of artesian aquifers. Economic Geology 23, 263-291.

Ozawa, S., Murakami, M., Fujiwara, S. and Tobita, M., 1997, Synthetic aperture radar interferogram of the 1995 Kobe earthquake and its geodetic inversion, Geophysical Research Letters, v. 24, no. 18, p. 2327 – 2330.

Peake, W.H., and Oliver, T.L., 1971, The Response of Terrestrial Surfaces at Microwave Frequencies, Ohio State University Technical Report 2440-7, Columbus, Ohio.

Poland, J.F., and Ireland, R.L., 1988, Land Subsidence in the Santa Clara Valley, California, as of 1982: U.S. Geological Survey Professional Paper 497-F, 61 p.

Poland, J.F., 1988, Subsidence due to ground water withdrawal, *in* Speidel, D.H., Ruedisili, L.C., Agnew, A.F., 1988, Perspectives on water uses and abuses. Oxford University Press, p.272.

Rahn, P.H., 1996, Engineering geology: an environmental approach, Prentice Hall PTR. p.353.

Raucoules, D., Colesanti, C., and Carnec, C., 2007, Use of SAR Interferometry for Detecting and Assessing Ground Subsidence, Comptes Rendus Geoscience, Elsevier, no. 339, p. 289 – 302.

Riley, F.S., 1969. Analysis of borehole extensometer data from central California. Land Subsidence, Vol. 2, IAHS Publication 89. IAHS, Wallingford,

Shaded Relief map of Nedava, 1999, Nevada Bureau of Mines and Geology educational series E-31

Singhroy, V., and Mattar, K., Gray, L., 1998, Landslide characterization in Canada using interferometric SAR and combined SAR and TM images. Adv. Space Res. 2 (3), 465–476.

Singhroy, V., Ohkura, H., and Molch, K., 2004, Monitoring landslides and volcanic deformation from InSAR technique. International Geological Congress, vol. 32, Part 2, pp.1182.

Tumbusch, M. L., and Plume, R.W., 2006,Hydrogeologic framework and ground water in basin-fill deposits of the Diamond Valley flow system, central Nevada. U.S. Geological Survey Scientific Inv.
Terzaghi, K., 1925, Principles of soil mechanics, IV, Settlement and consolidation of clay, Eng. News Rec., 95(3), p. 874–878.

Terzaghi, K., Peck, R.B., and Mesri, G., 1996, Soil Mechanics in Engineering Practice, John Wiley & Sons, Inc., p. 83-85, p. 467-469.

Weeks, R.E., Panda, B., and Fergason, K., Unpublished, Application of Synthetic Aperture Radar Interferometry (InSAR) in Defining Mine-Related Ground Deformation and Subsidence Hazards, Unpublished.

Appendix I

This appendix includes all 34 interferometric pairs successfully processed in this study. The unwrapped interferogram of each pair or the wrapped interferogram of a pair which did not process phase unwrapping is presented. Each interferogram is cropped to show approximately the same portion of the valley. A color fringe (red-yellow-green-blue) represents 2.83 cm of LOS distance. Unwrapped interferograms are draped over a shaded DEM and areas where the interferogram layer is absent represent data drop-out in areas of low coherence that were masked during the phase unwrapping process.

Satellite Type	Master Acquisition Date	Slave Acquisition Date	Perpendicular Baseline (m)
ERS-1/ERS-2	6/17/1992	4/6/1996	102
Wrapped interferogram			

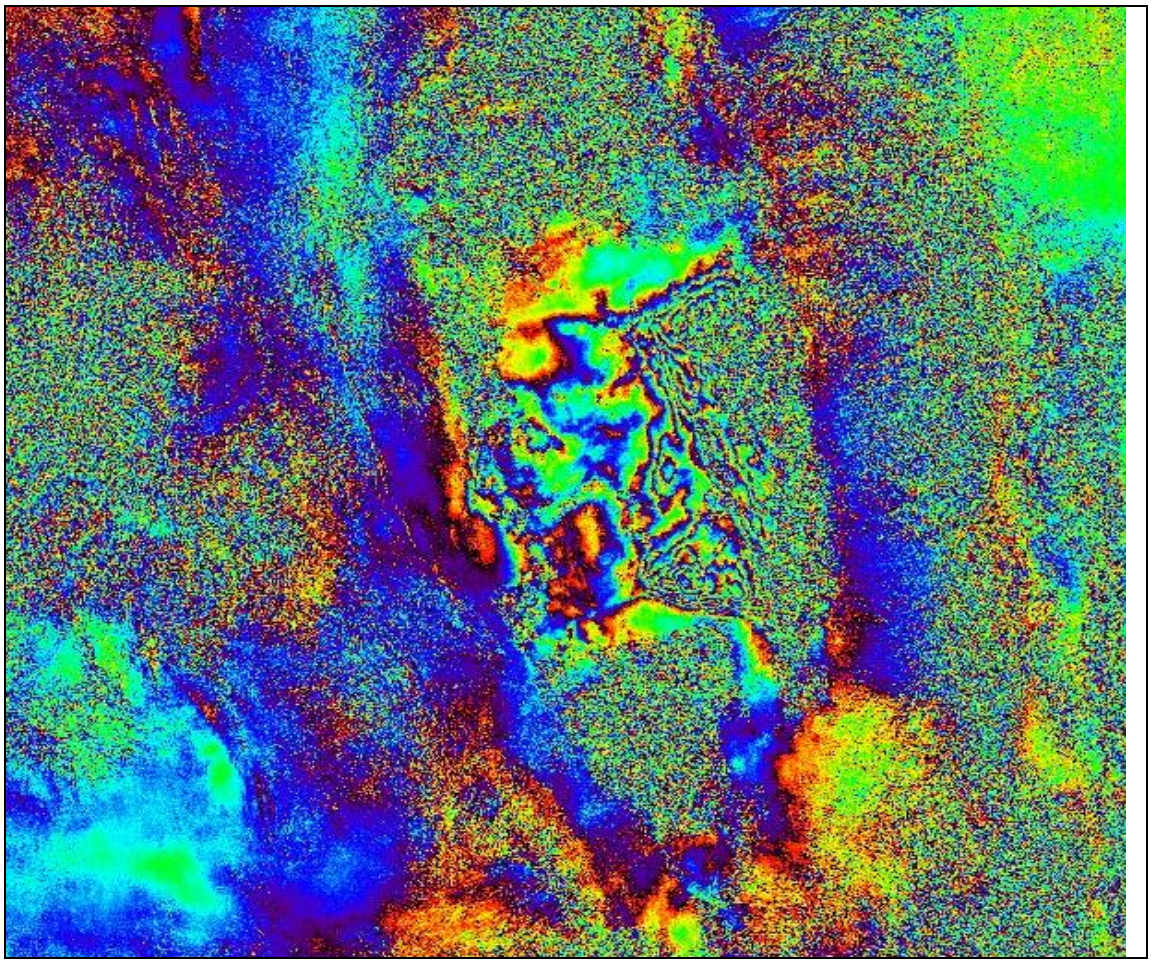

Satellite Type	Master Acquisition Date	Slave Acquisition Date	Perpendicular Baseline (m)
ERS-1/ERS-2	6/17/1992	9/28/1996	18
Unwrapped interferogram			

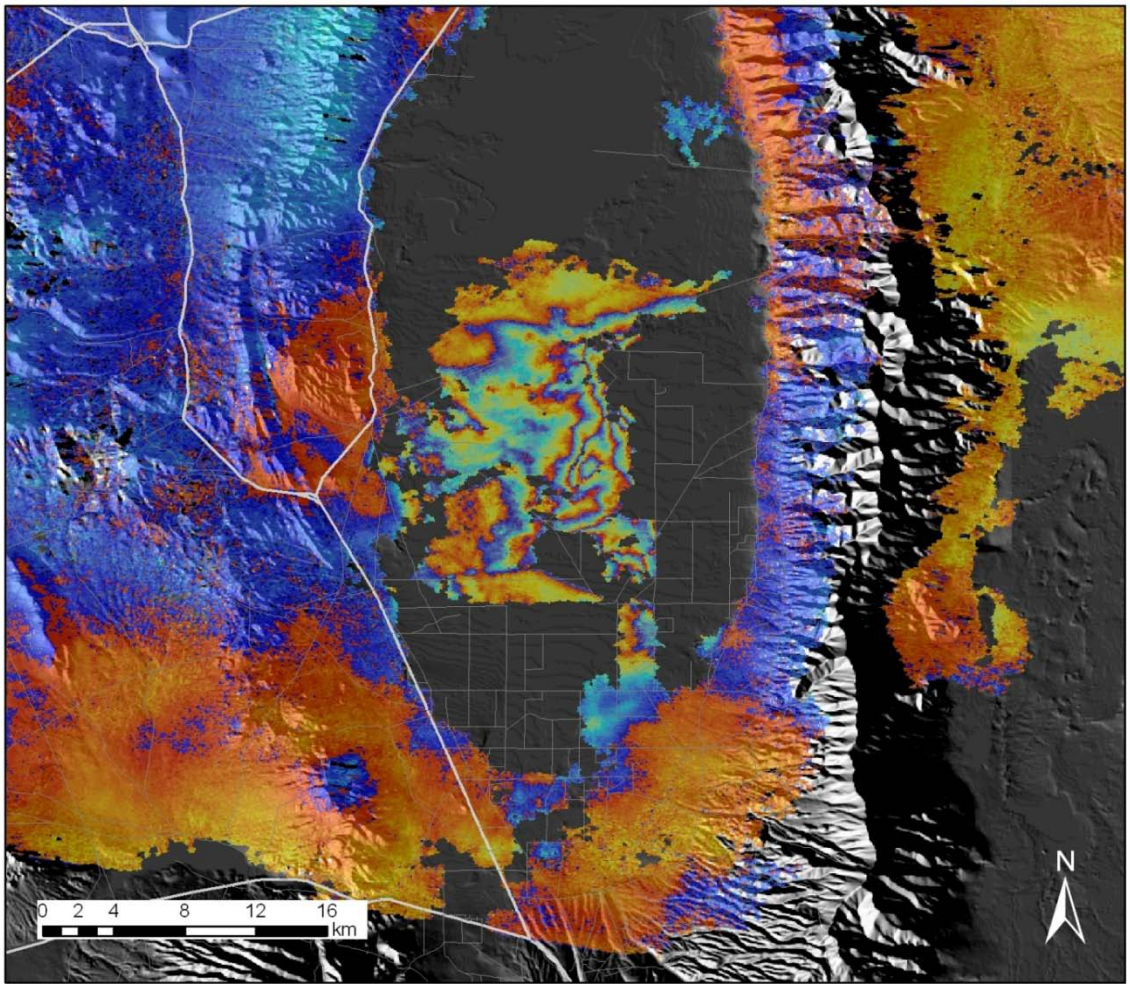

Satellite Type	Master Acquisition Date	Slave Acquisition Date	Perpendicular Baseline (m)
ERS-1/ERS-2	6/17/1992	7/5/1997	89
Wrapped interferogram			

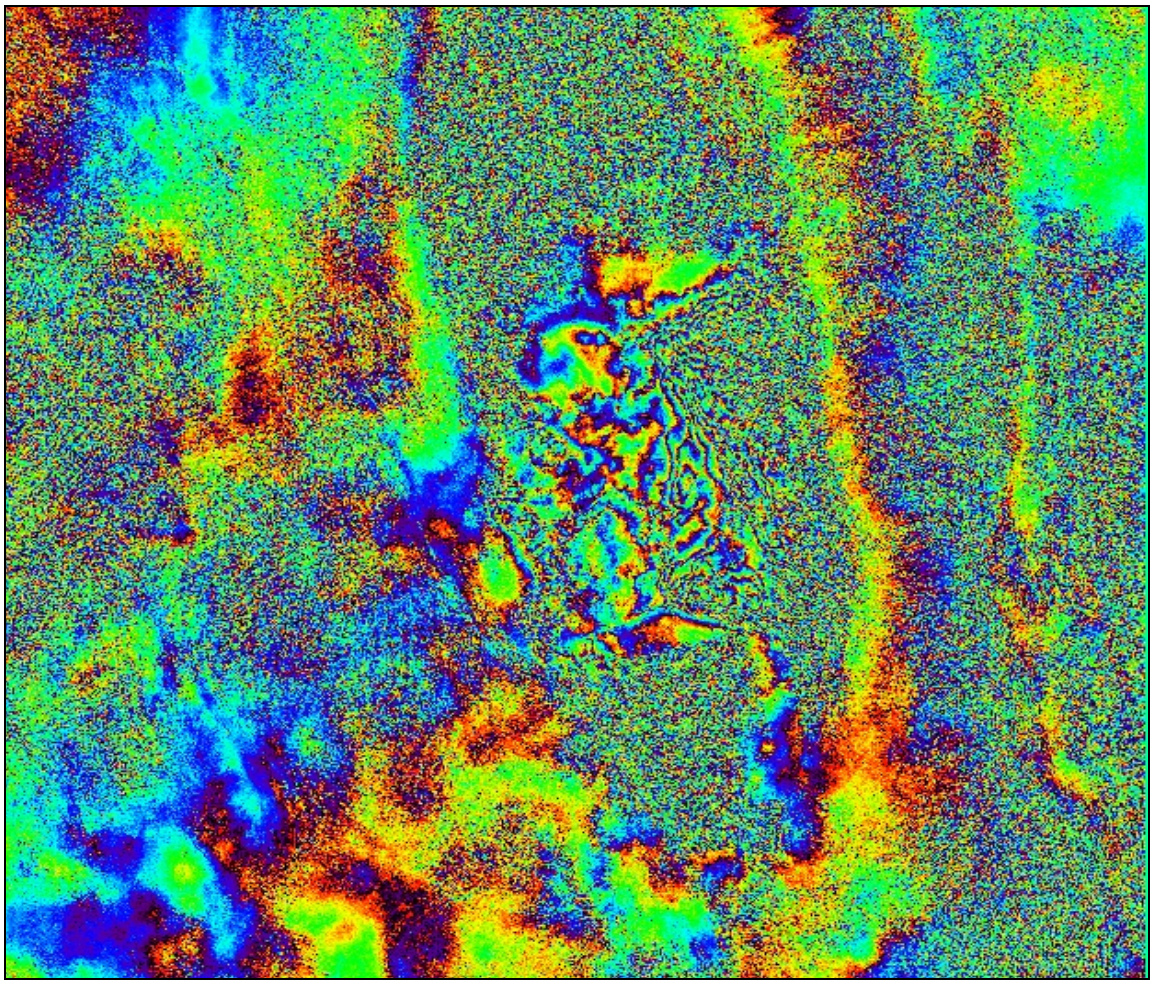

Satellite Type	Master Acquisition Date	Slave Acquisition Date	Perpendicular Baseline (m)
ERS-1/ERS-2	9/30/1992	5/11/1996	7
Unwrapped interferogram			

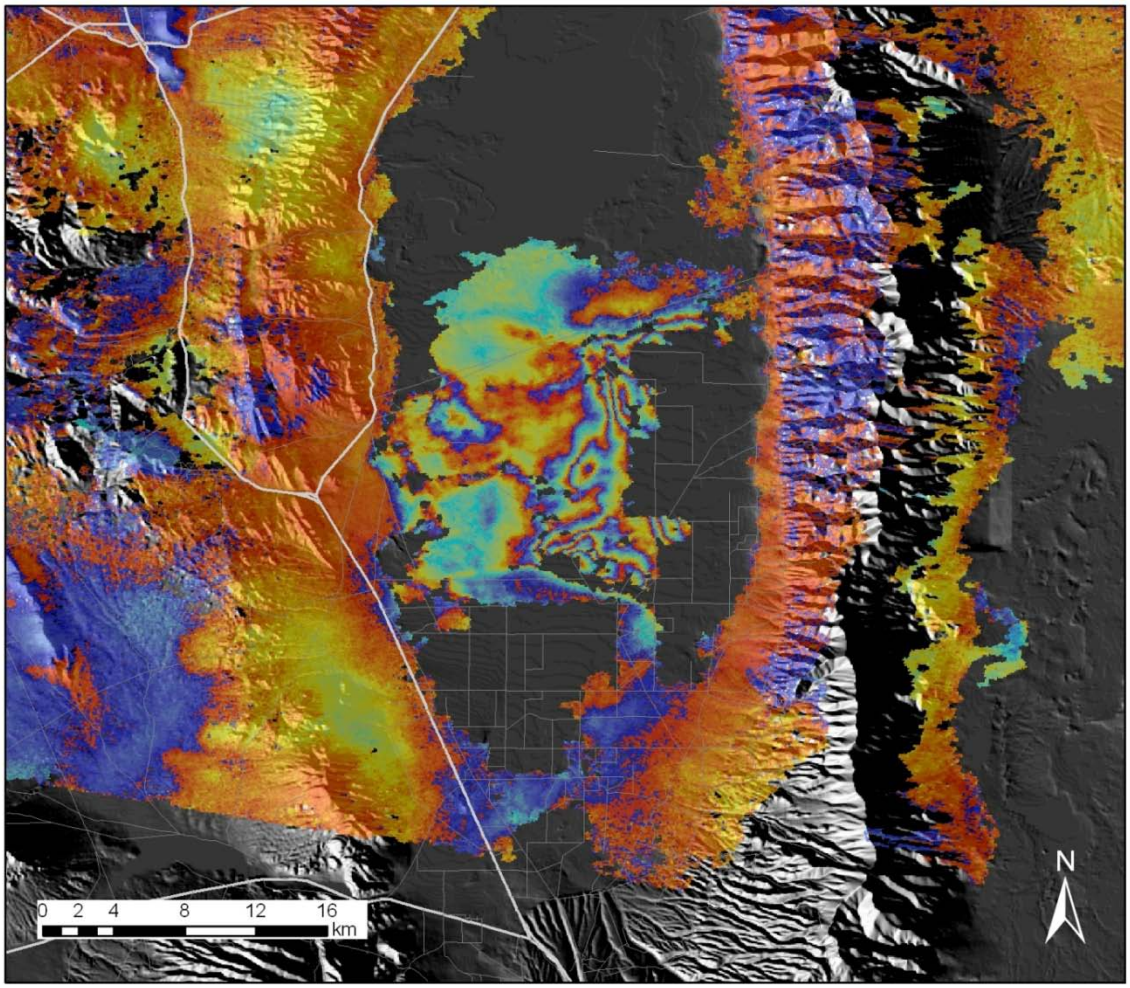

Satellite Type	Master Acquisition Date	Slave Acquisition Date	Perpendicular Baseline (m)
ERS-1/ERS-2	7/7/1993	11/18/1995	89
Unwrapped interferogram			

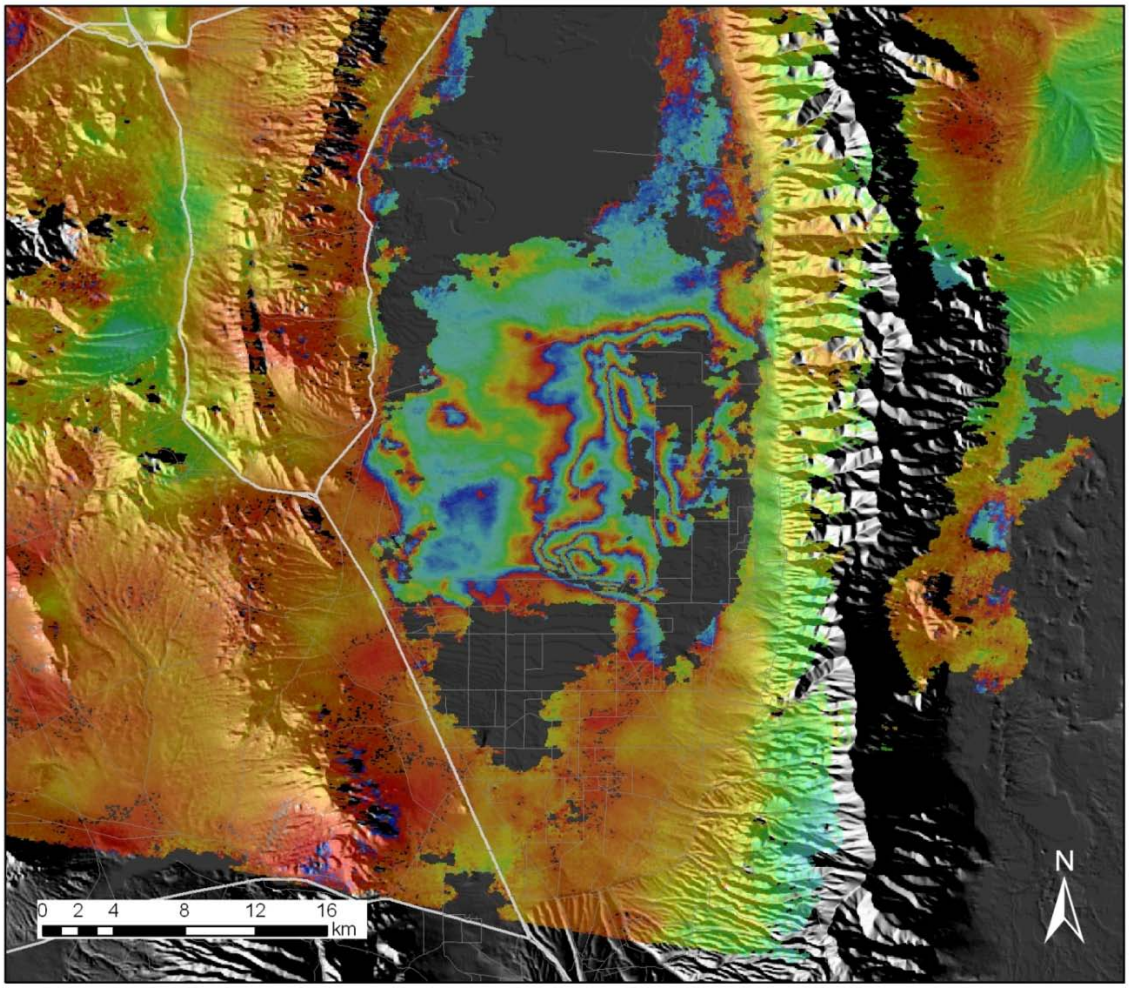

Satellite Type	Master Acquisition Date	Slave Acquisition Date	Perpendicular Baseline (m)
ERS-2	04/06/1996	09/28/1996	110
Unwrapped interferogram			

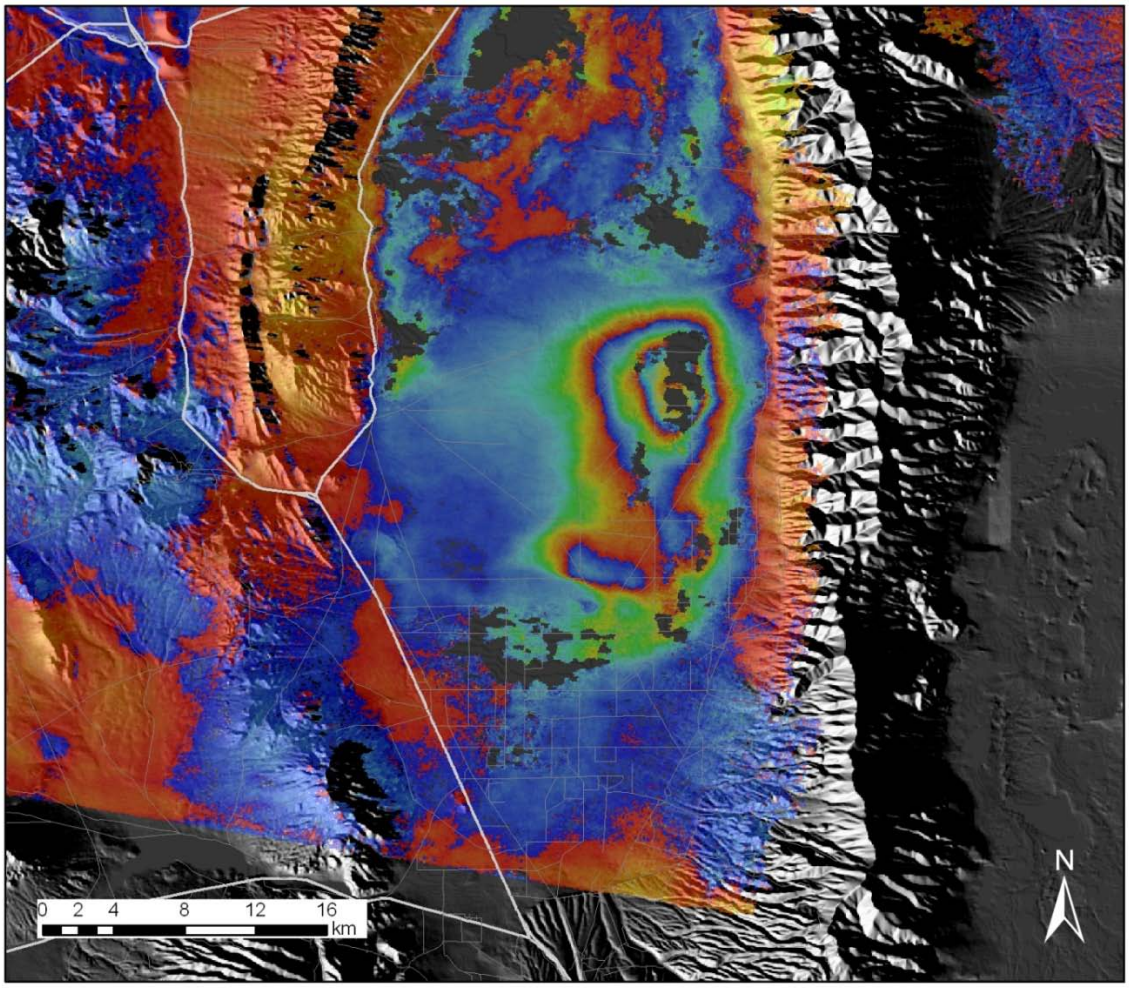

Satellite Type	Master Acquisition Date	Slave Acquisition Date	Perpendicular Baseline (m)
ERS-2	4/6/1996	4/11/1998	163
Unwrapped interferogram			

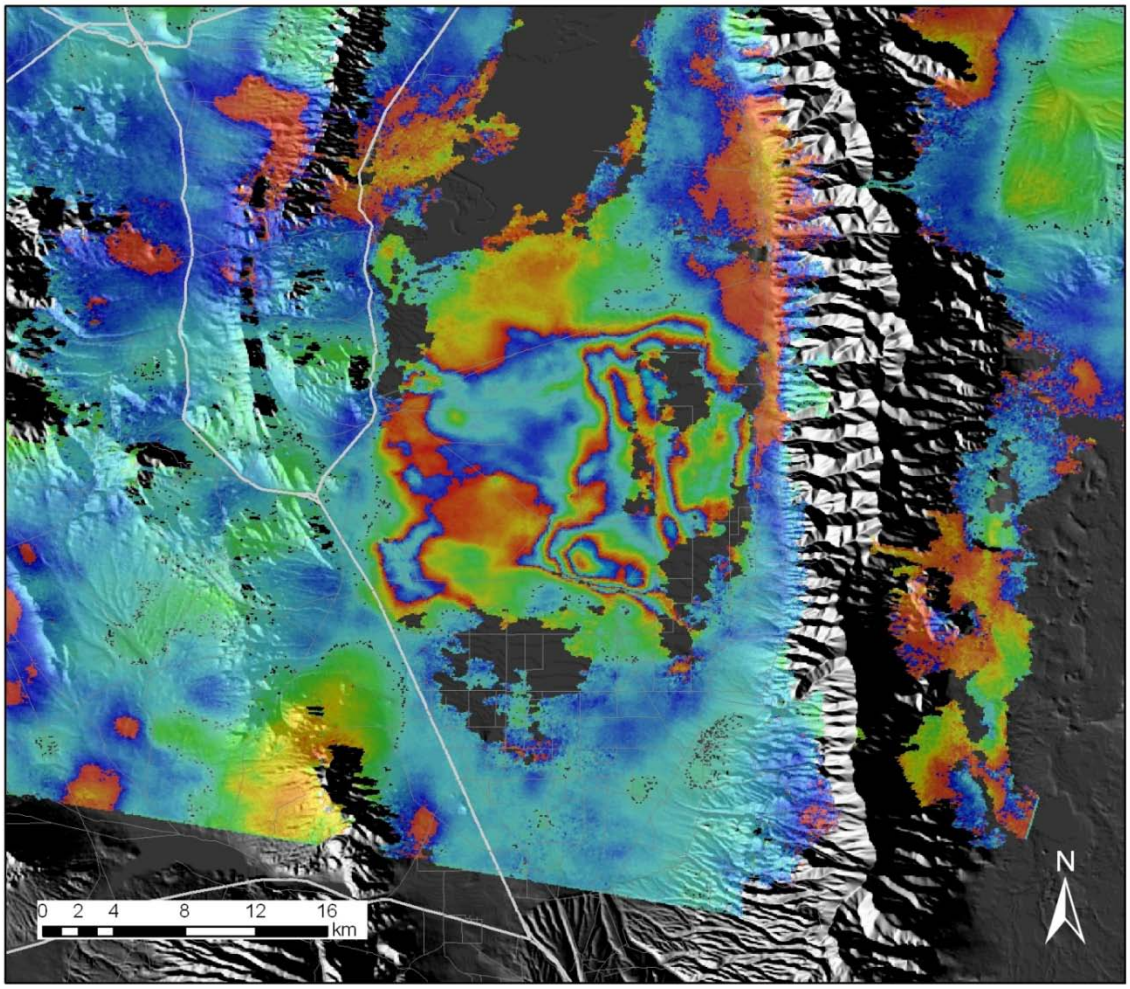

Satellite Type	Master Acquisition Date	Slave Acquisition Date	Perpendicular Baseline (m)
ERS-2	4/6/1996	4/15/2000	7
Wrapped interferogram			

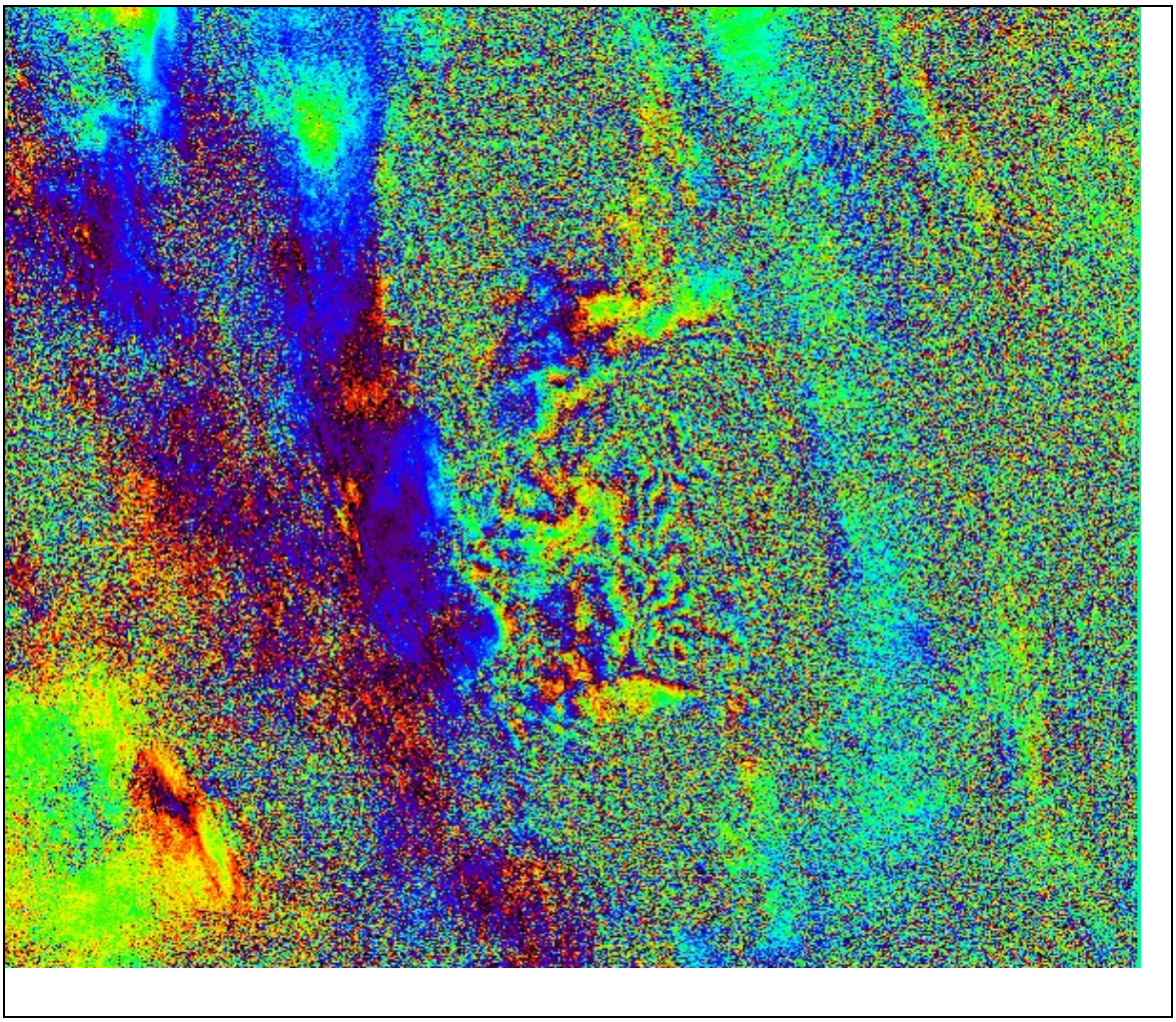

Satellite Type	Master Acquisition Date	Slave Acquisition Date	Perpendicular Baseline (m)
ERS-2	9/28/1996	7/5/1997	71
Unwrapped interferogram			

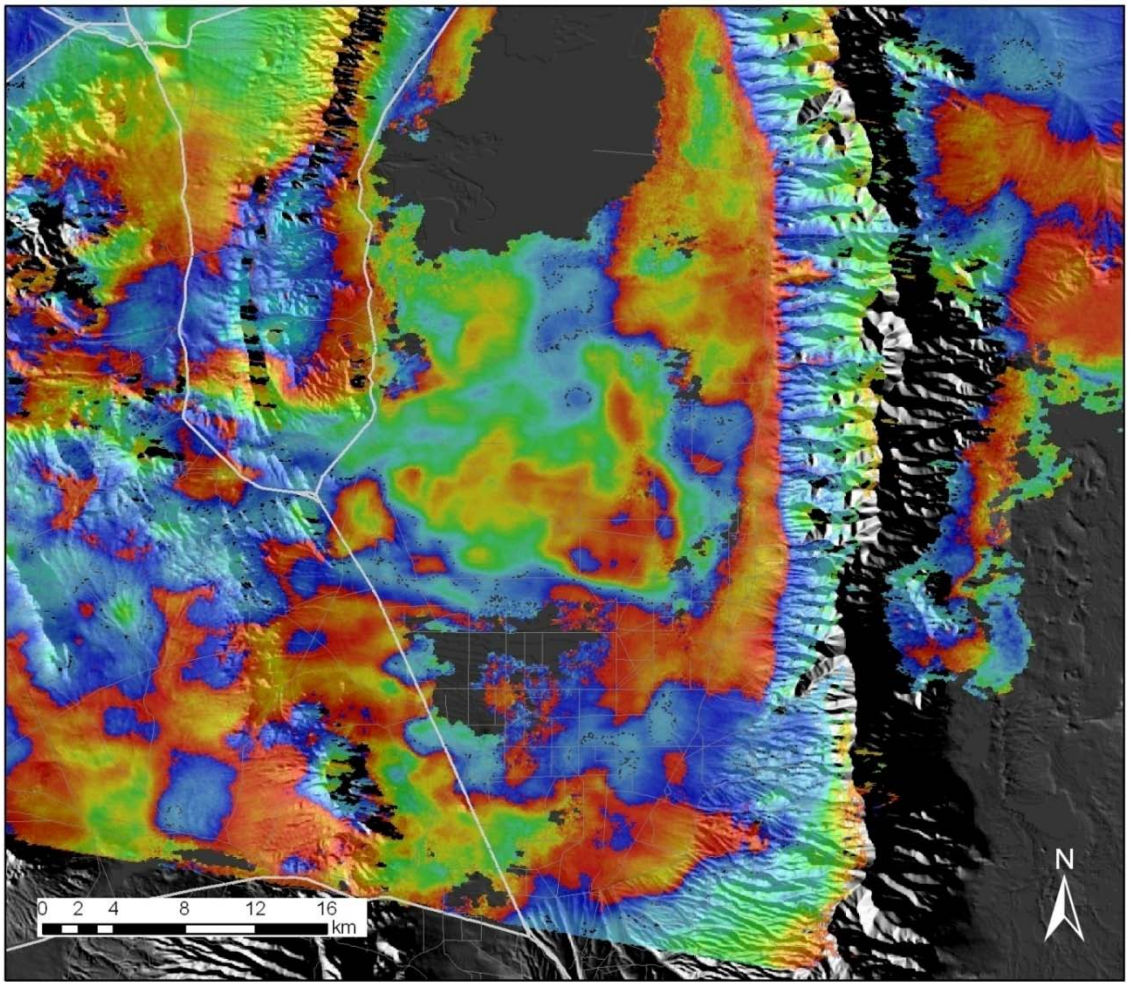

Satellite Type	Master Acquisition Date	Slave Acquisition Date	Perpendicular Baseline (m)
ERS-2	9/28/1996	4/11/1998	43
Unwrapped interferogram			

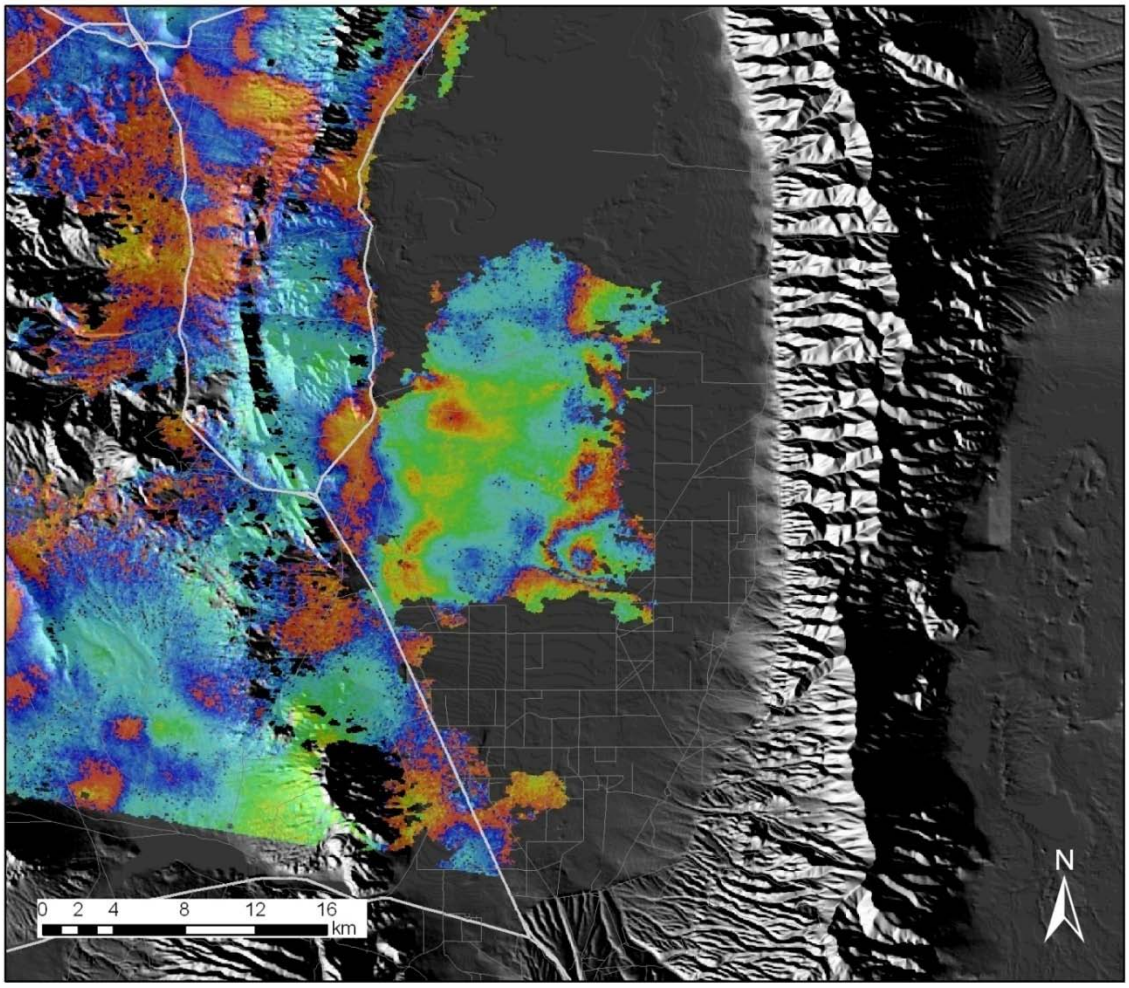

Satellite Type	Master Acquisition Date	Slave Acquisition Date	Perpendicular Baseline (m)
ERS-2	9/28/1996	11/27/1999	70
Unwrapped interferogram			

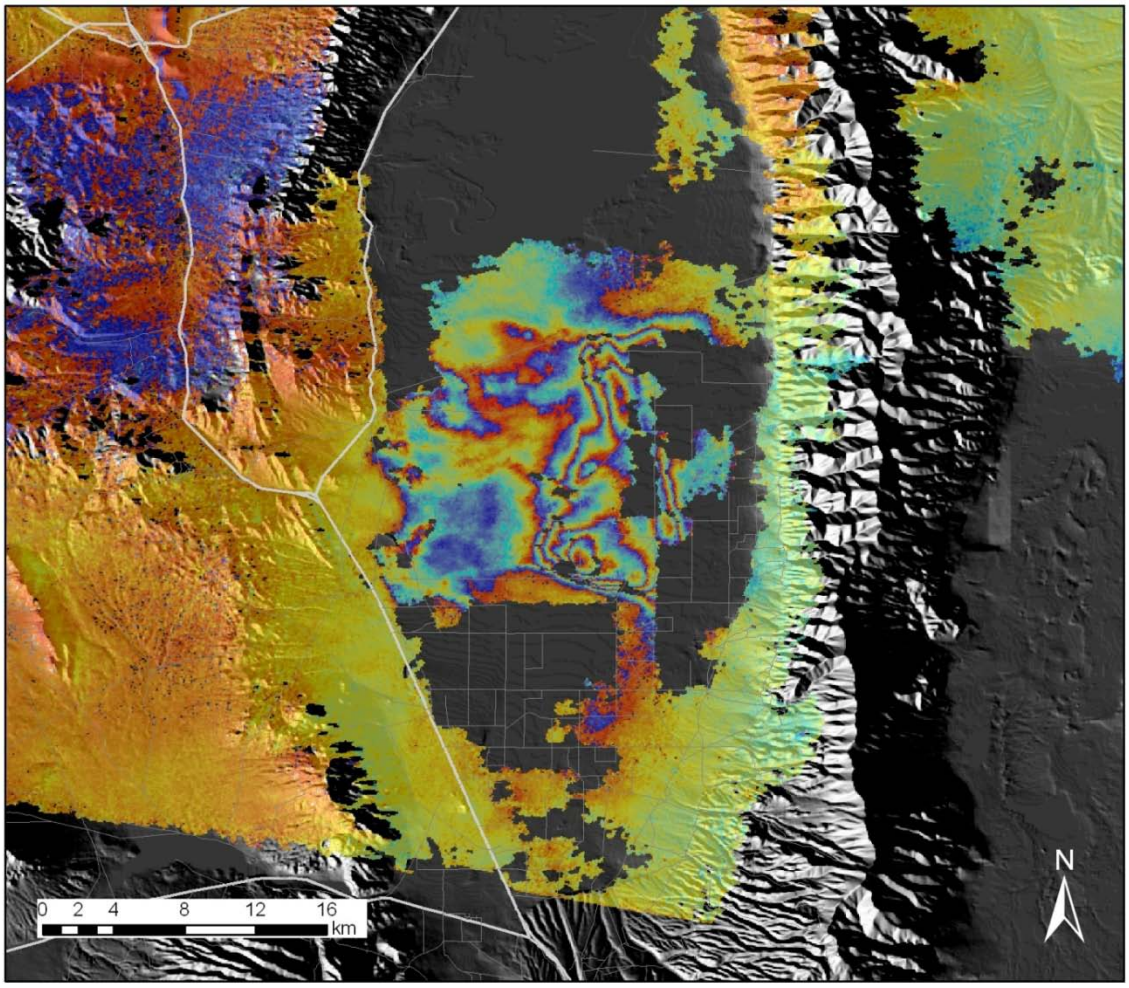

Satellite Type	Master Acquisition Date	Slave Acquisition Date	Perpendicular Baseline (m)
ERS-2	7/5/1997	4/11/1998	28
Unwrapped interferogram			

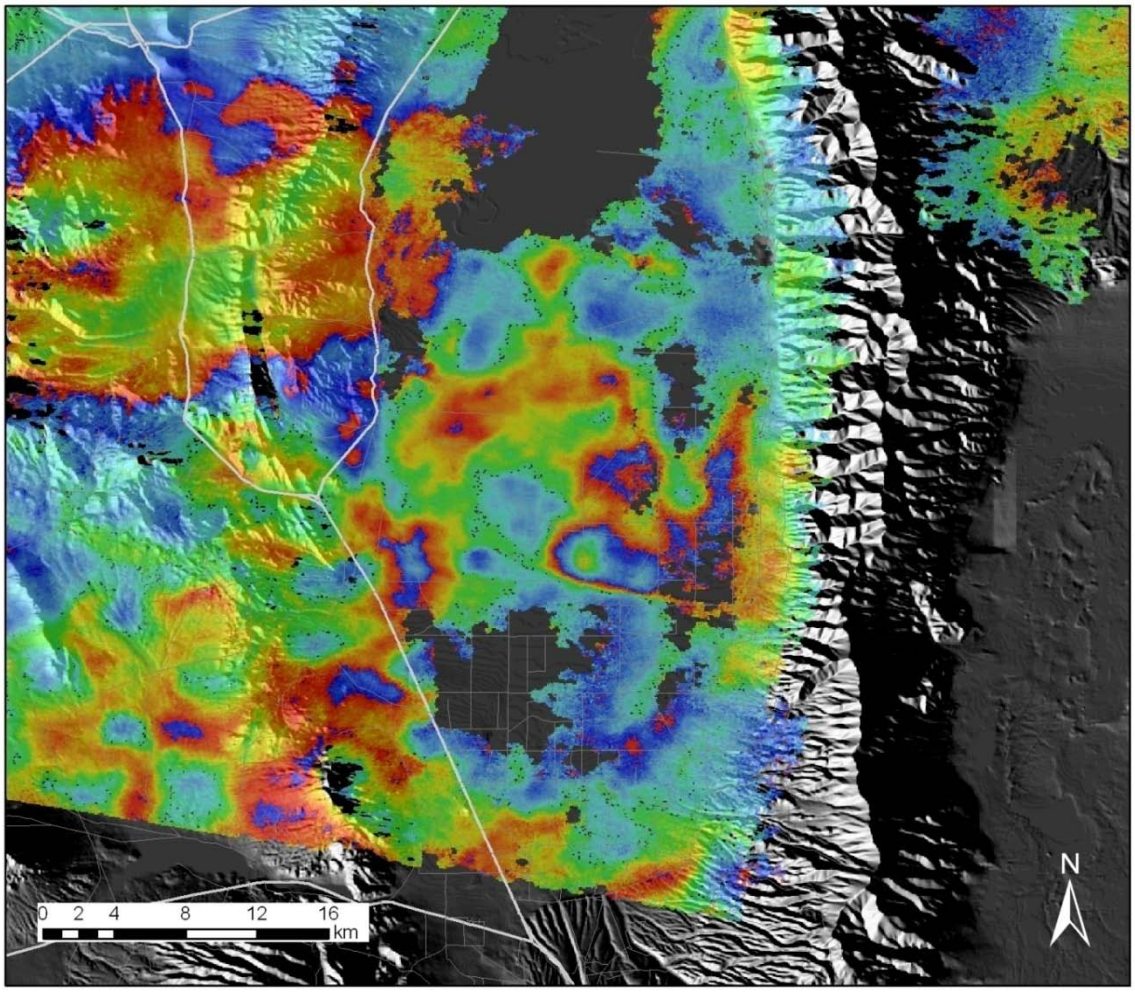

Satellite Type	Master Acquisition Date	Slave Acquisition Date	Perpendicular Baseline (m)
ERS-2	7/5/1997	5/1/1999	162

Wrapped interferogram

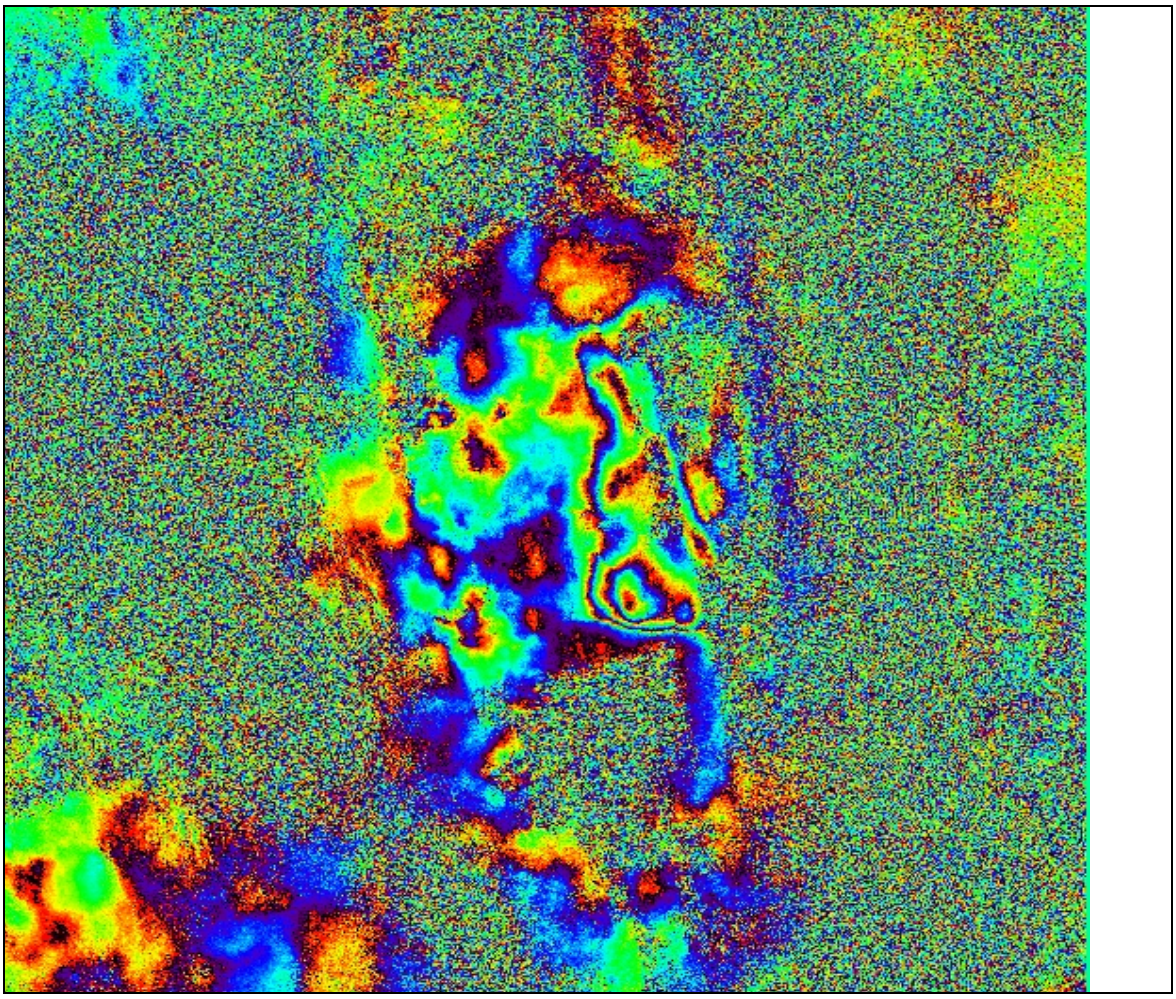

Satellite Type	Master Acquisition Date	Slave Acquisition Date	Perpendicular Baseline (m)
ERS-2	7/5/1997	11/27/1999	141

Unwrapped interferogram

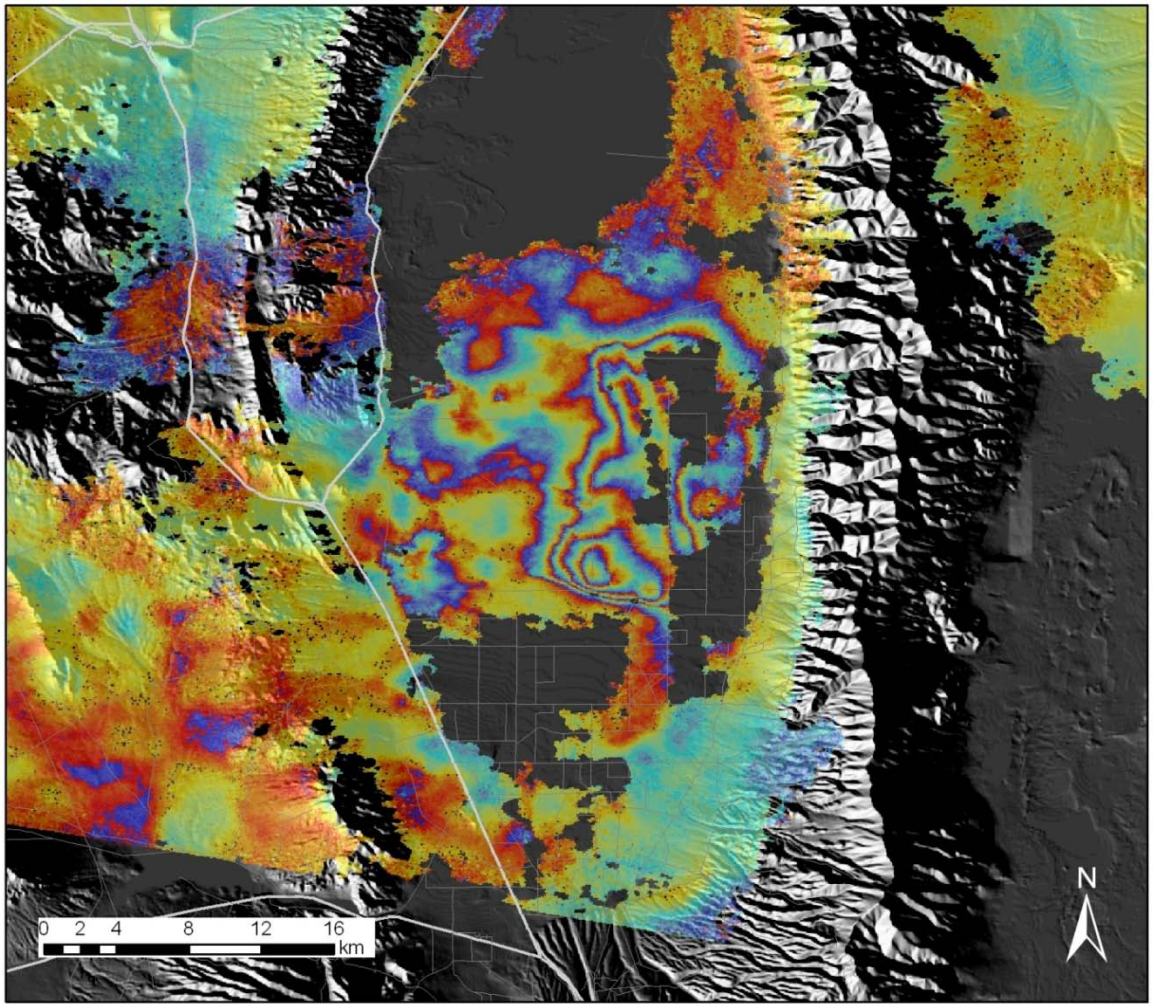

Satellite Type	Master Acquisition Date	Slave Acquisition Date	Perpendicular Baseline (m)
ERS-2	4/11/1998	5/1/1999	134

Unwrapped interferogram

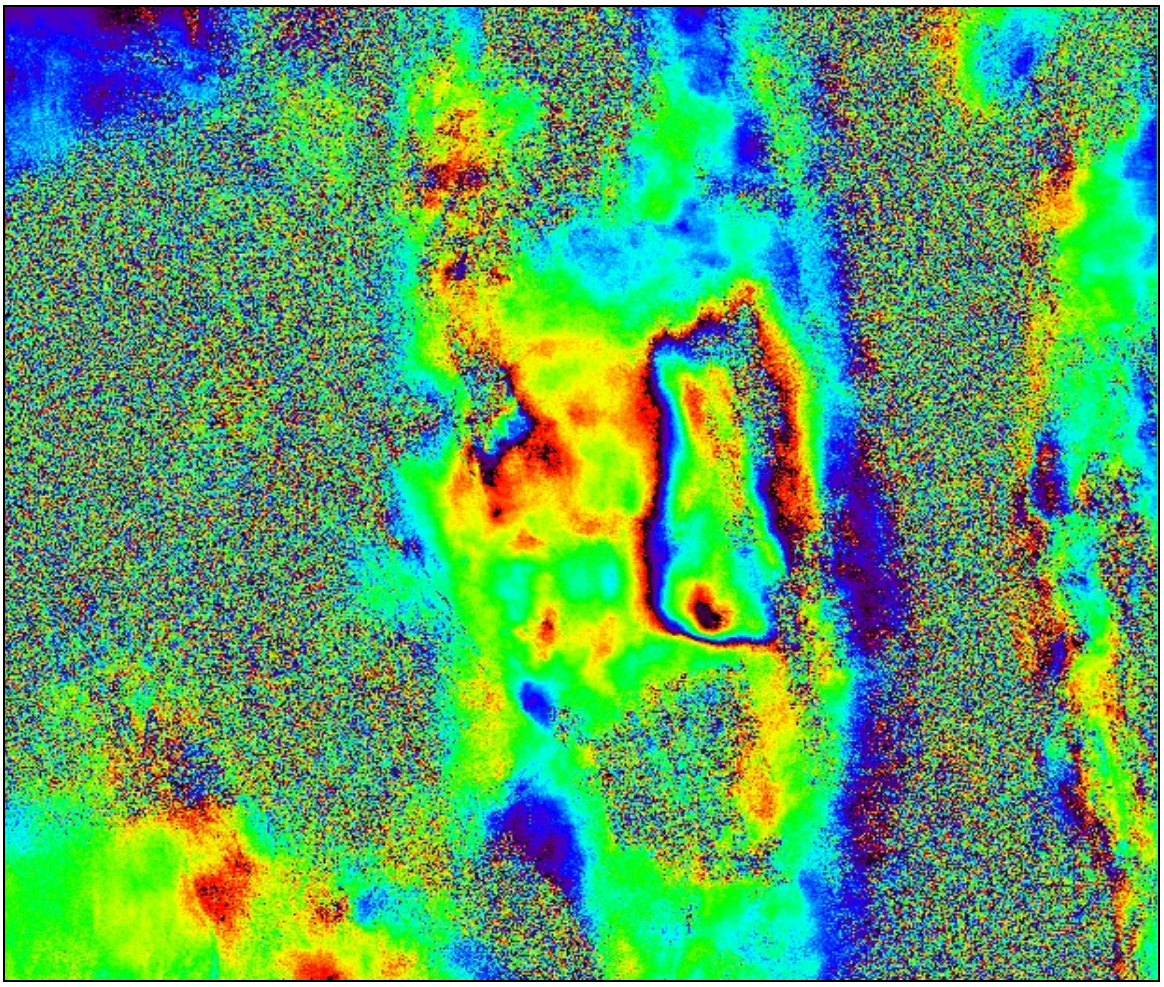

Satellite Type	Master Acquisition Date	Slave Acquisition Date	Perpendicular Baseline (m)
ERS-2	4/11/1998	11/27/1999	113
Unwrapped interferogram			

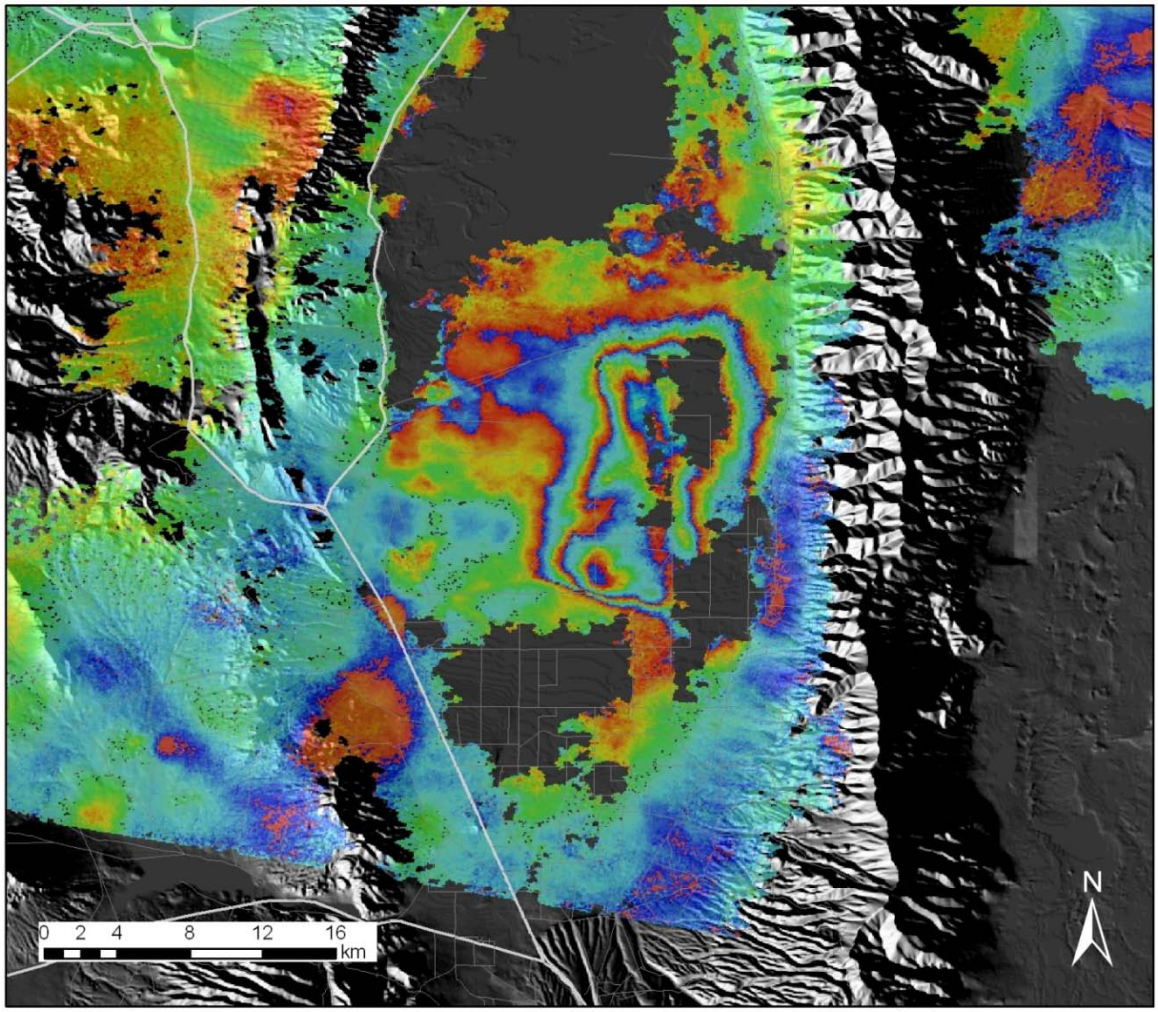

Satellite Type	Master Acquisition Date	Slave Acquisition Date	Perpendicular Baseline (m)
ERS-2	4/11/1998	4/15/2000	156
Unwrapped interferogram			

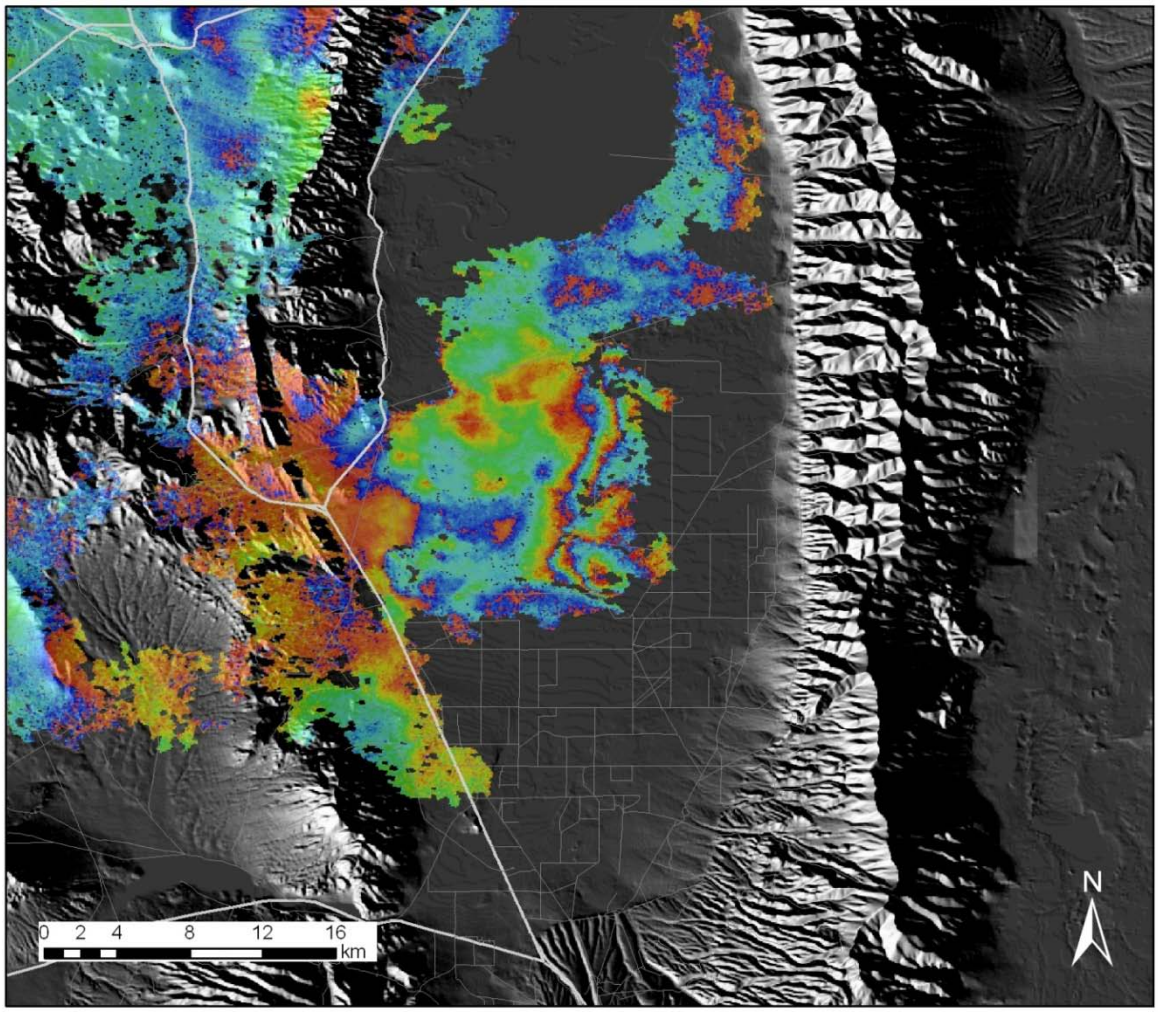

Satellite Type	Master Acquisition Date	Slave Acquisition Date	Perpendicular Baseline (m)
ERS-2	5/1/1999	4/15/2000	22
Wrapped interferogram			

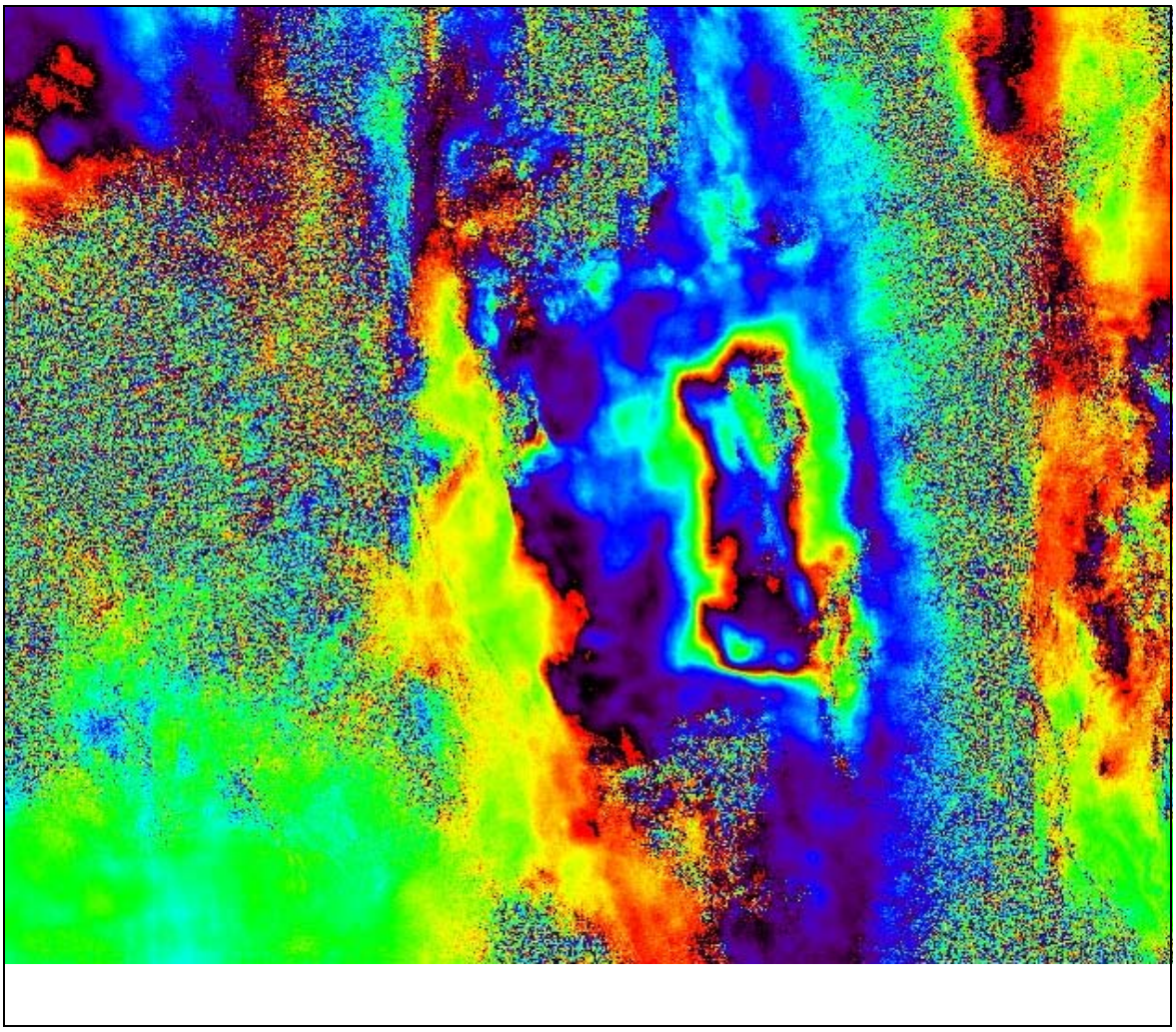

Satellite Type	Master Acquisition Date	Slave Acquisition Date	Perpendicular Baseline (m)
ERS-2	11/27/1999	04/15/2000	112
Unwrapped interferogram			

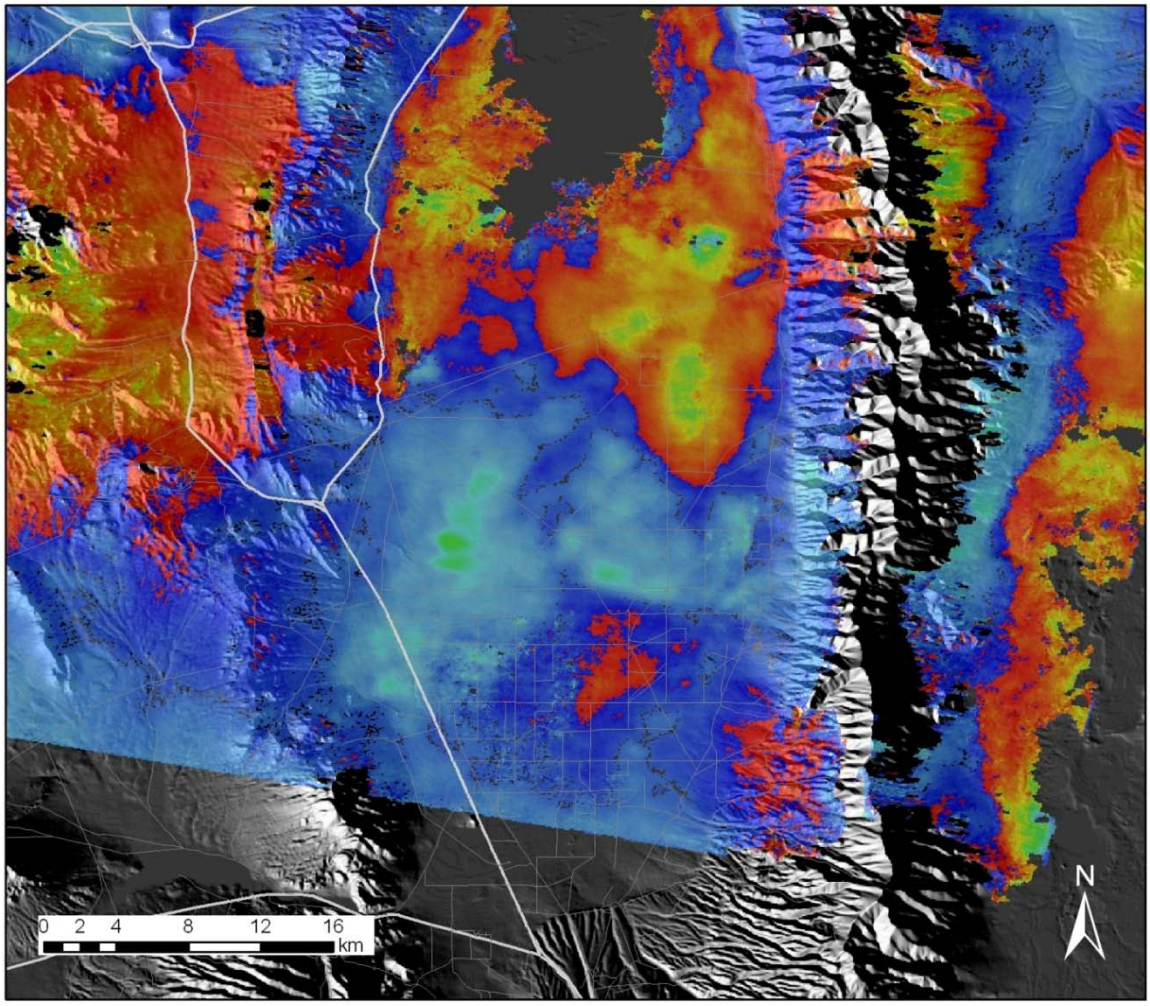

Satellite Type	Master Acquisition Date	Slave Acquisition Date	Perpendicular Baseline (m)
Envisat	09/11/2004	11/05/2005	171
Unwrapped interferogram			

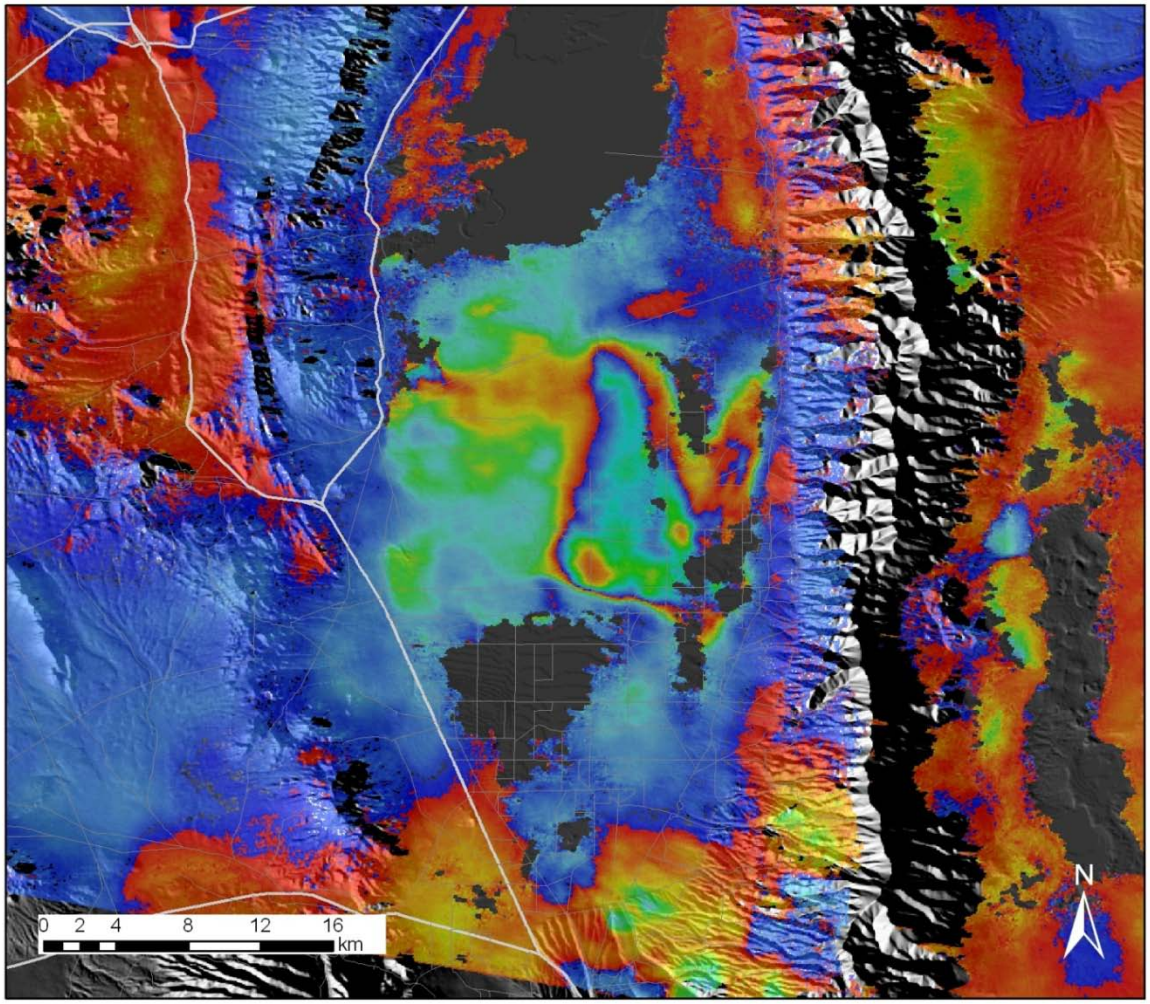

Satellite Type	Master Acquisition Date	Slave Acquisition Date	Perpendicular Baseline (m)
Envisat	09/11/2004	07/08/2006	80
Unwrapped interferogram			

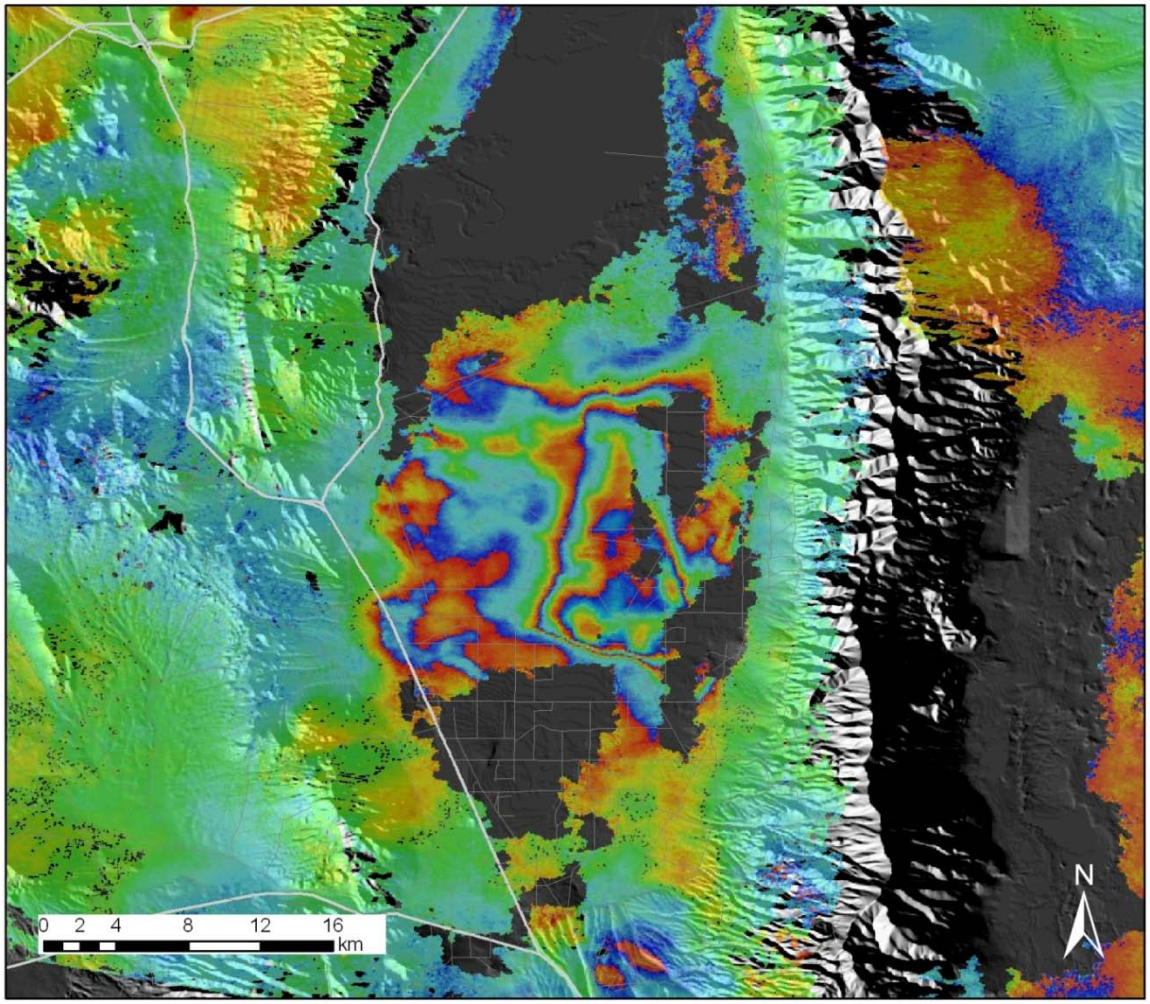

Satellite Type	Master Acquisition Date	Slave Acquisition Date	Perpendicular Baseline (m)
Envisat	09/11/2004	08/12/2006	88
Unwrapped interferogram			

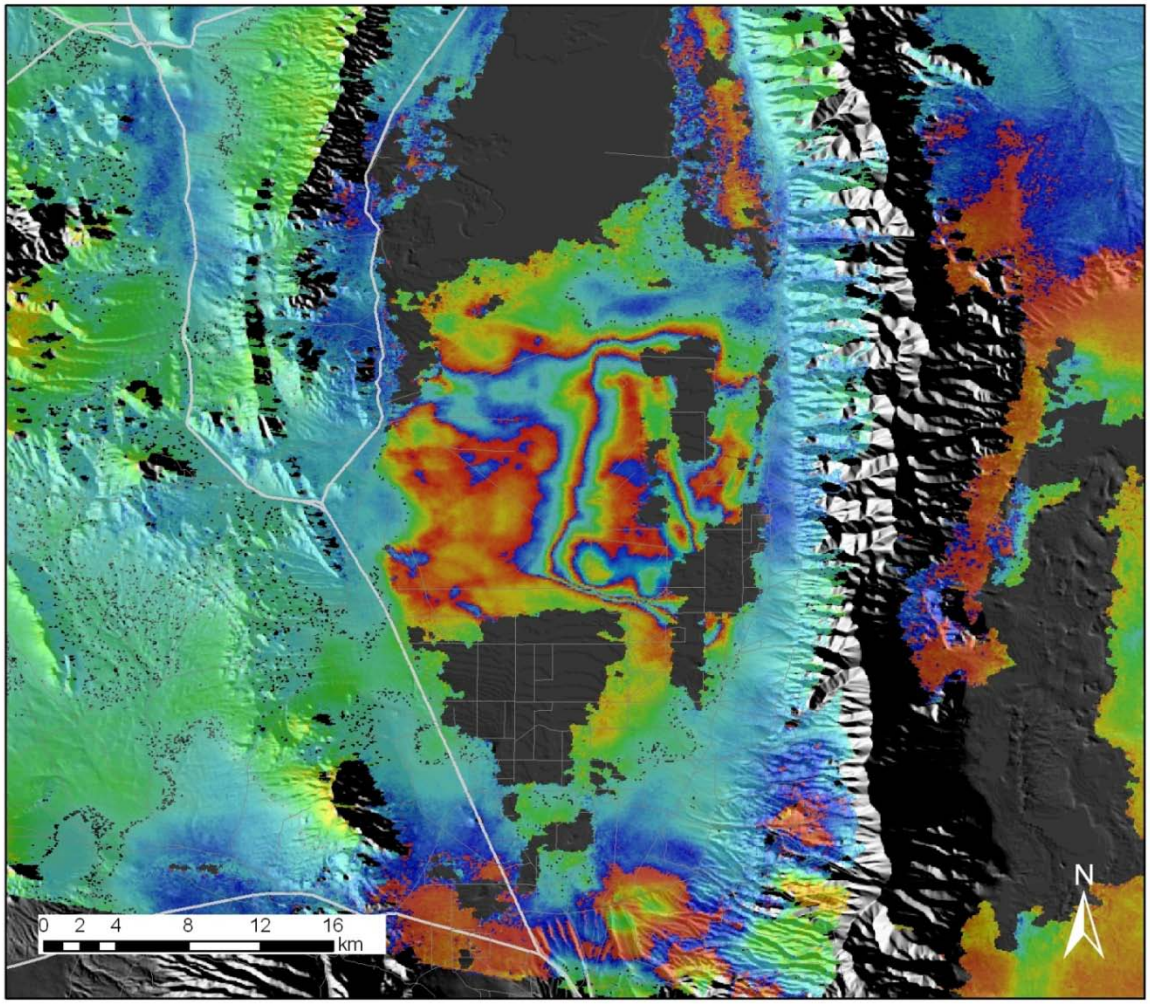

Satellite Type	Master Acquisition Date	Slave Acquisition Date	Perpendicular Baseline (m)
Envisat	10/16/2004	05/14/2005	4
Unwrapped interferogram			

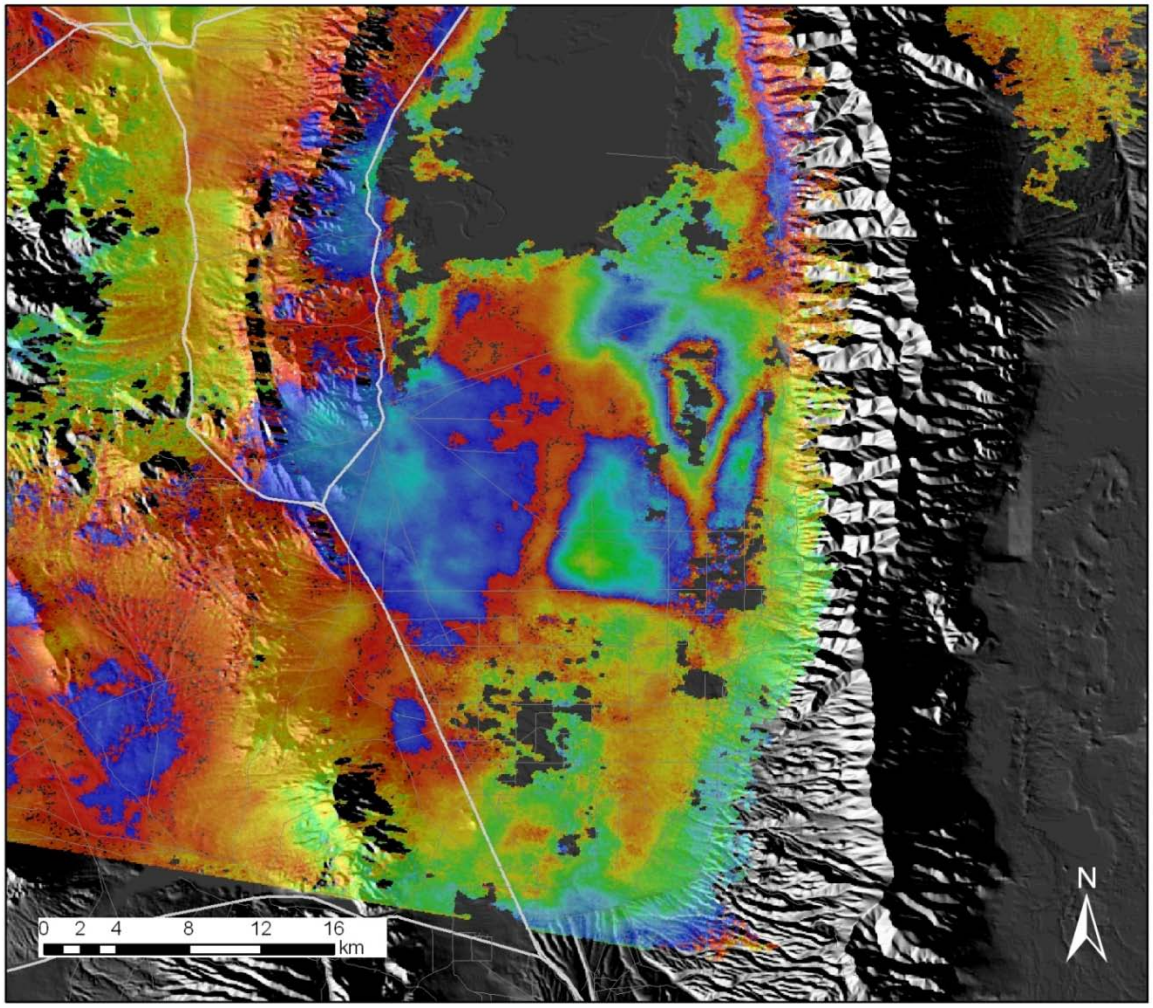

Satellite Type	Master Acquisition Date	Slave Acquisition Date	Perpendicular Baseline (m)
Envisat	10/16/2004	11/05/2005	120
Unwrapped interferogram			

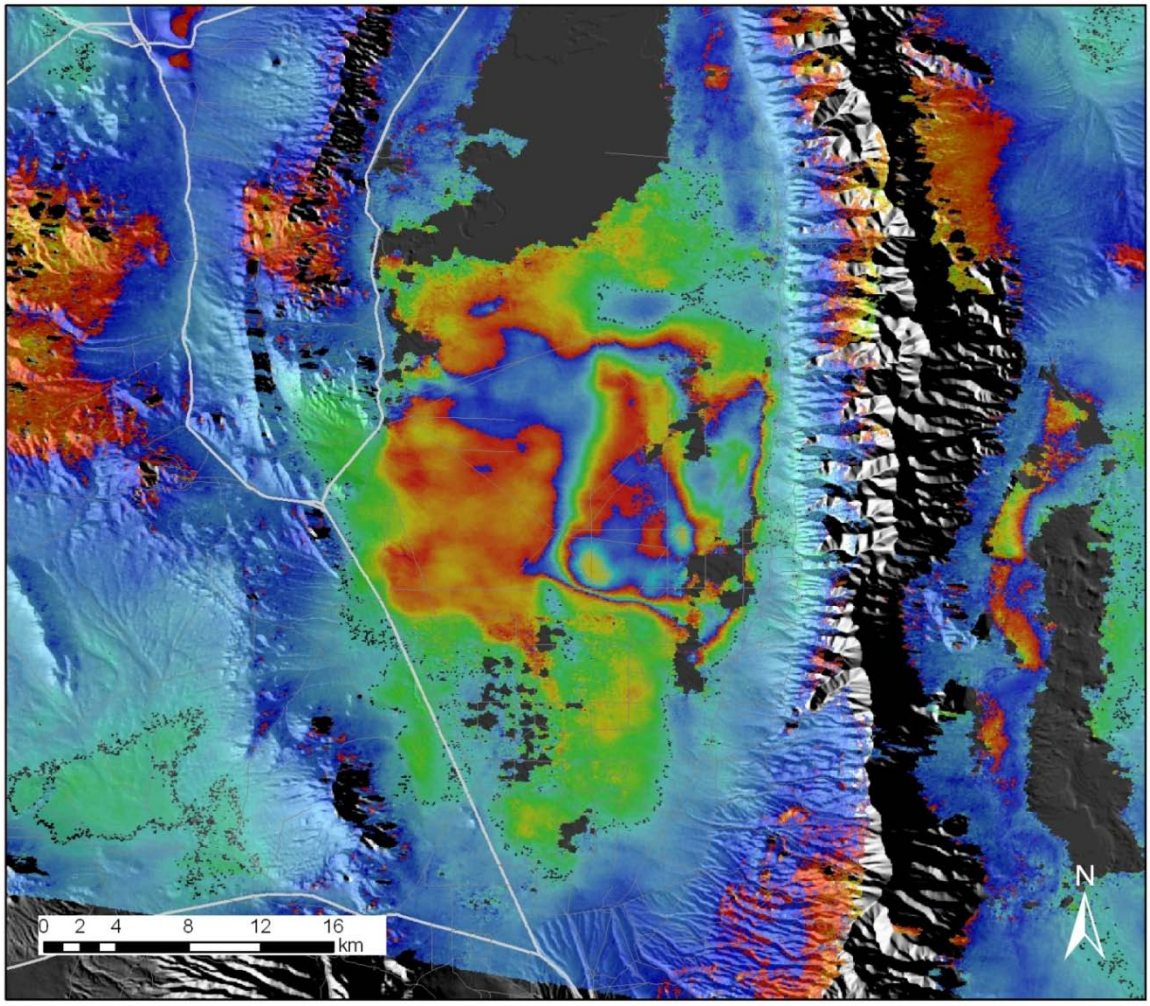

Satellite Type	Master Acquisition Date	Slave Acquisition Date	Perpendicular Baseline (m)
Envisat	10/16/2004	12/30/2006	66
Unwrapped interferogram			

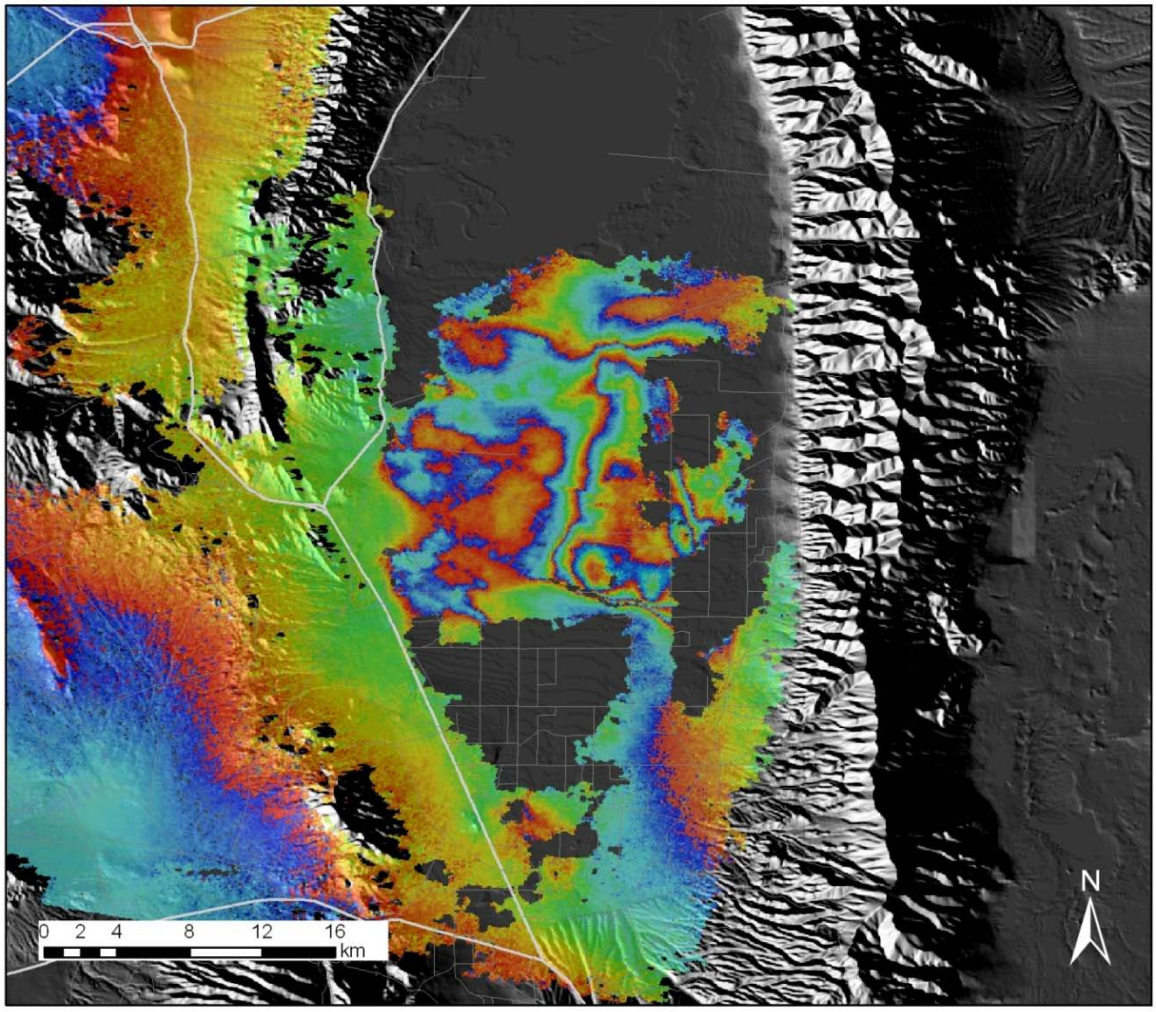

Satellite Type	Master Acquisition Date	Slave Acquisition Date	Perpendicular Baseline (m)
Envisat	10/16/2004	03/10/2007	98
Unwrapped interferogram			

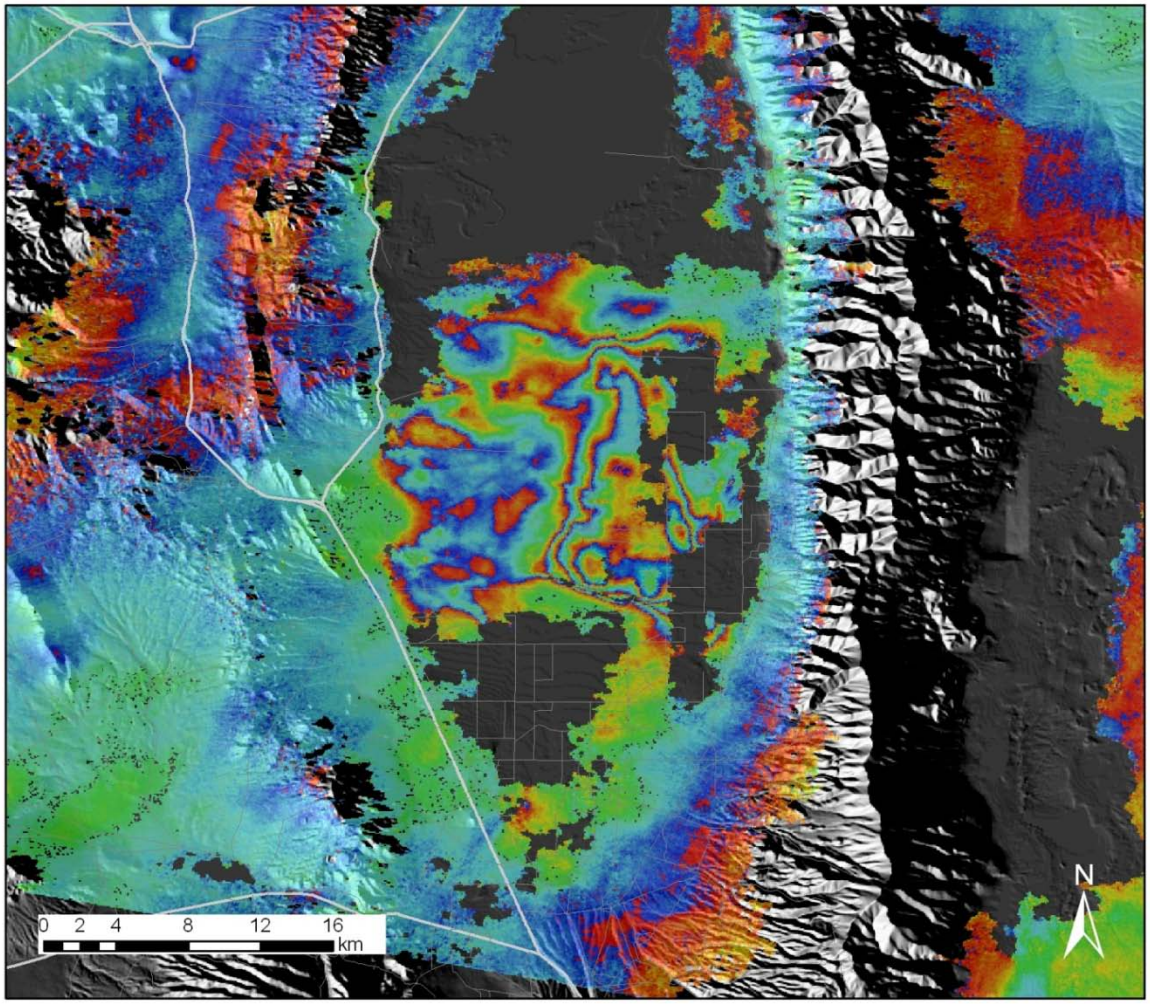

Satellite Type	Master Acquisition Date	Slave Acquisition Date	Perpendicular Baseline (m)
Envisat	01/29/2005	11/25/2006	86
Wrapped interferogram			

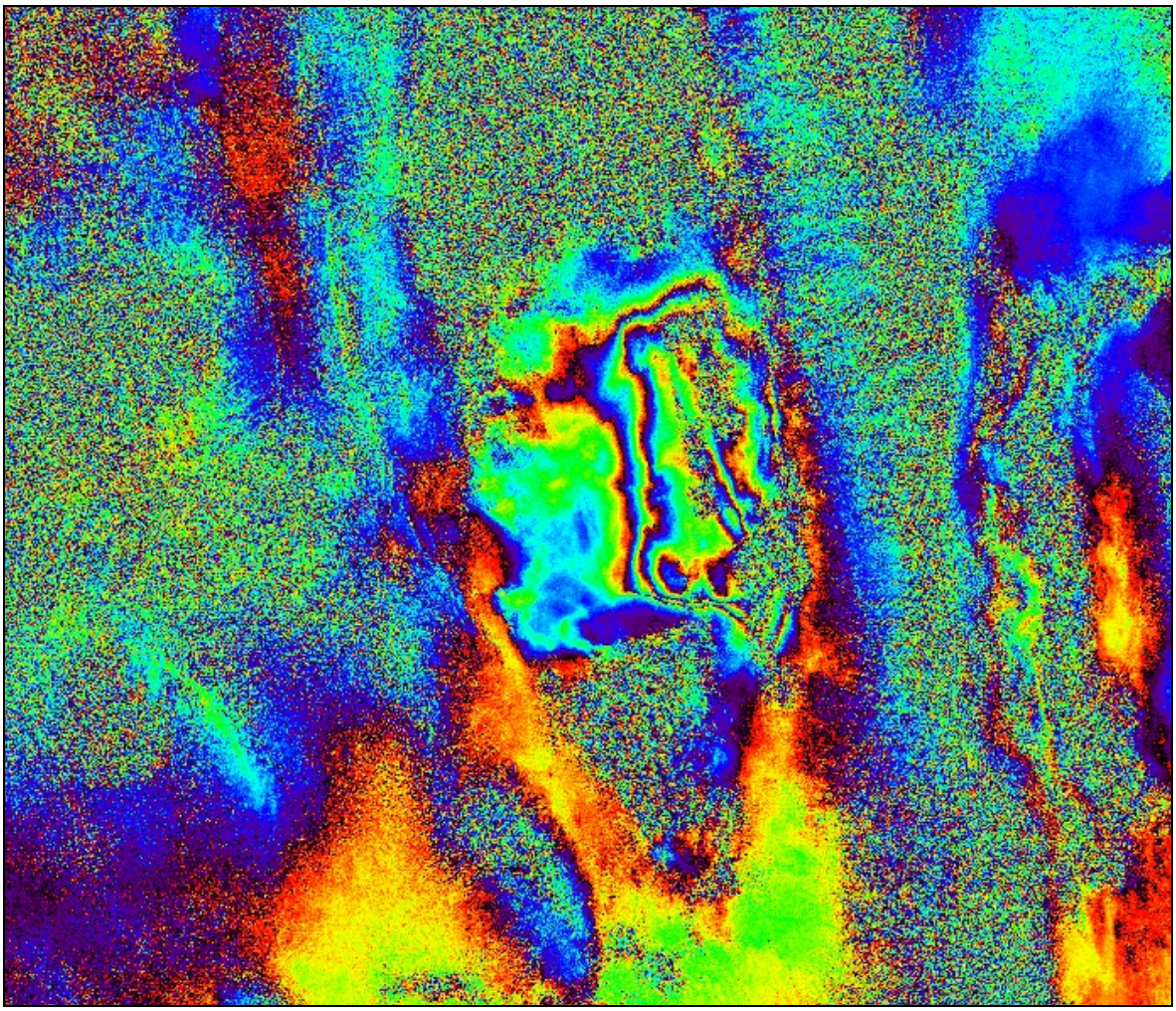

Satellite Type	Master Acquisition Date	Slave Acquisition Date	Perpendicular Baseline (m)
Envisat	05/14/2005	11/05/2005	124
Unwrapped interferogram			

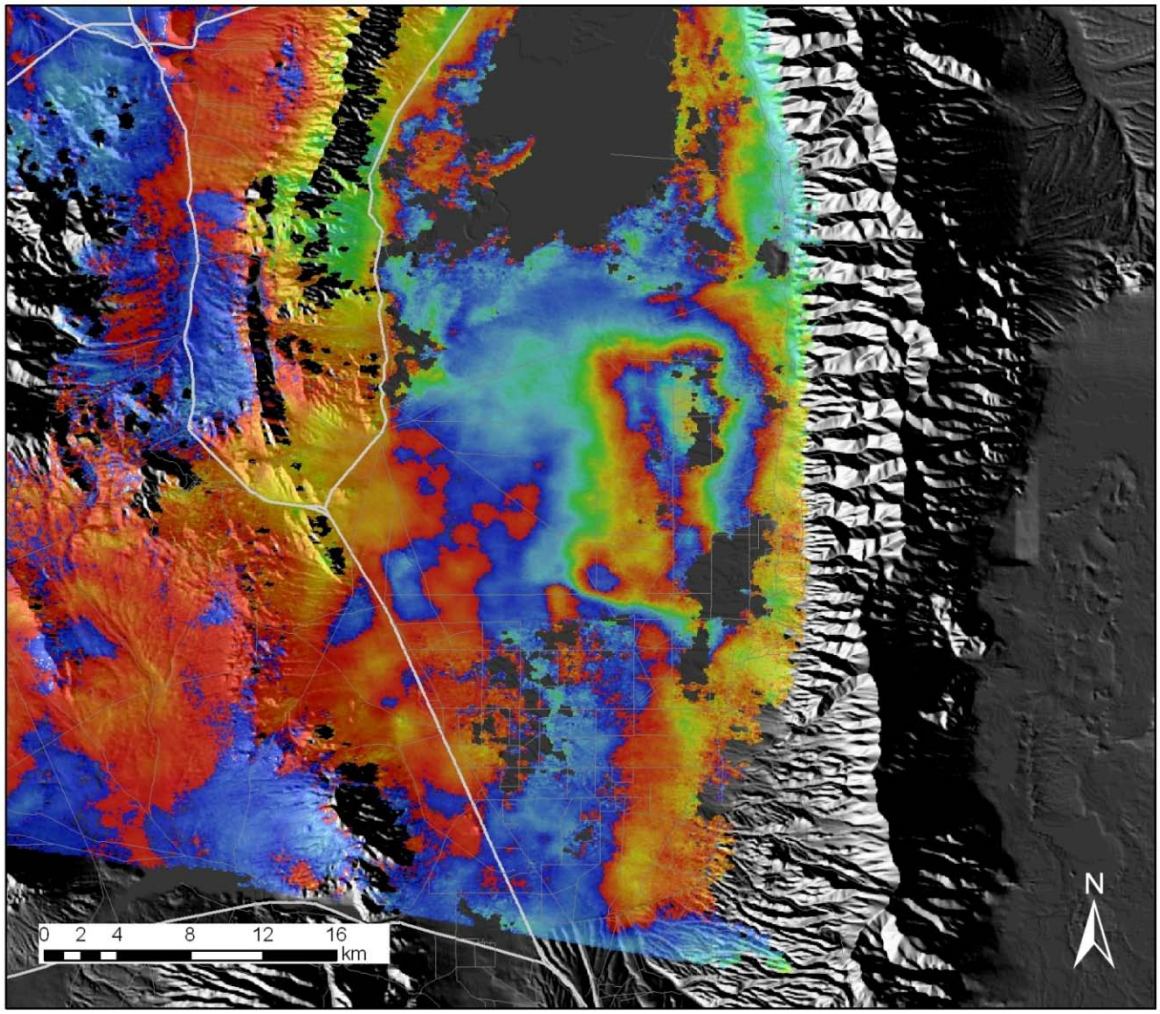

Satellite Type	Master Acquisition Date	Slave Acquisition Date	Perpendicular Baseline (m)
Envisat	05/14/2005	12/30/2006	62
Unwrapped interferogram			

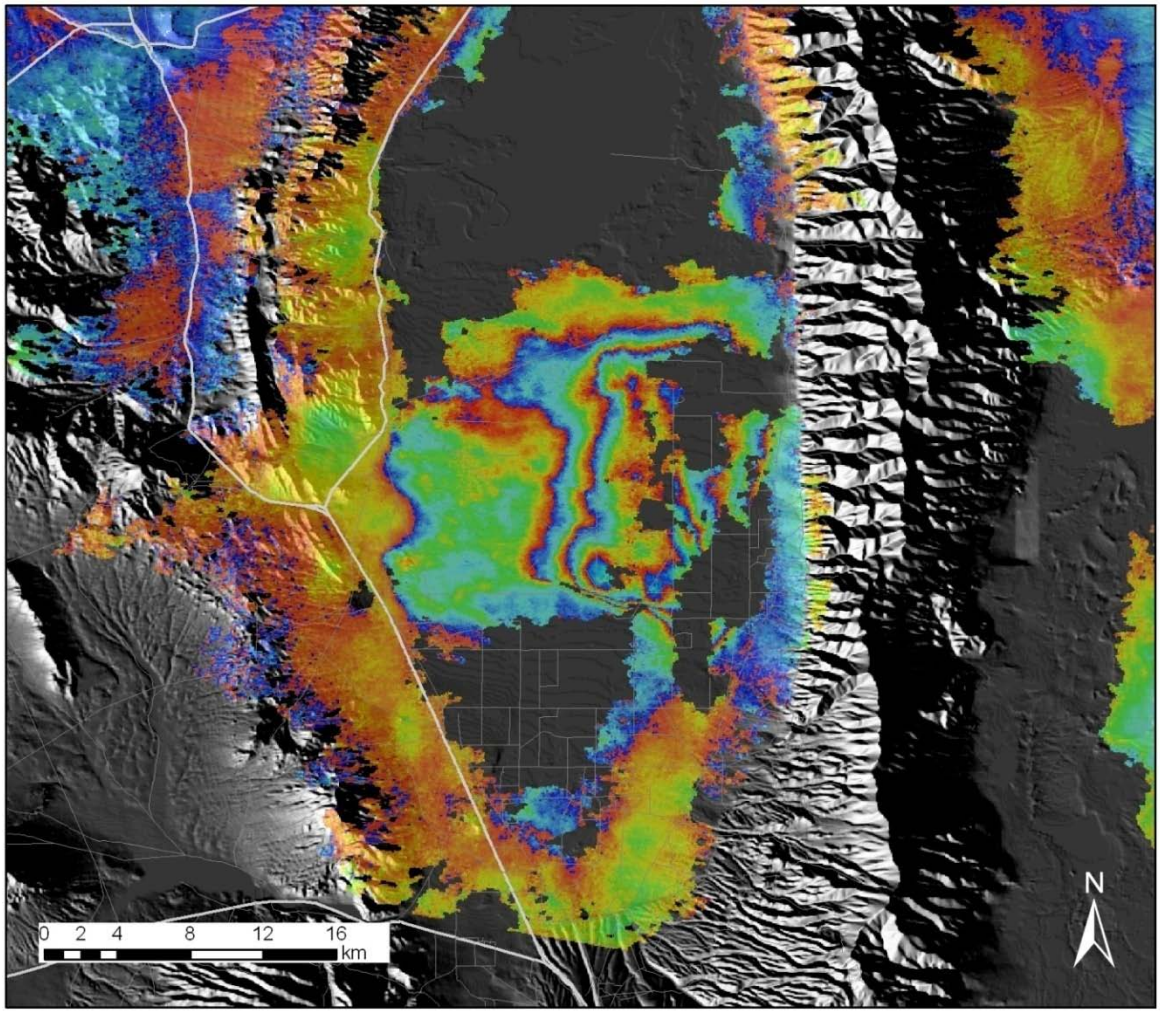

Satellite Type	Master Acquisition Date	Slave Acquisition Date	Perpendicular Baseline (m)
Envisat	05/14/2005	03/10/2007	94
Unwrapped interferogram			

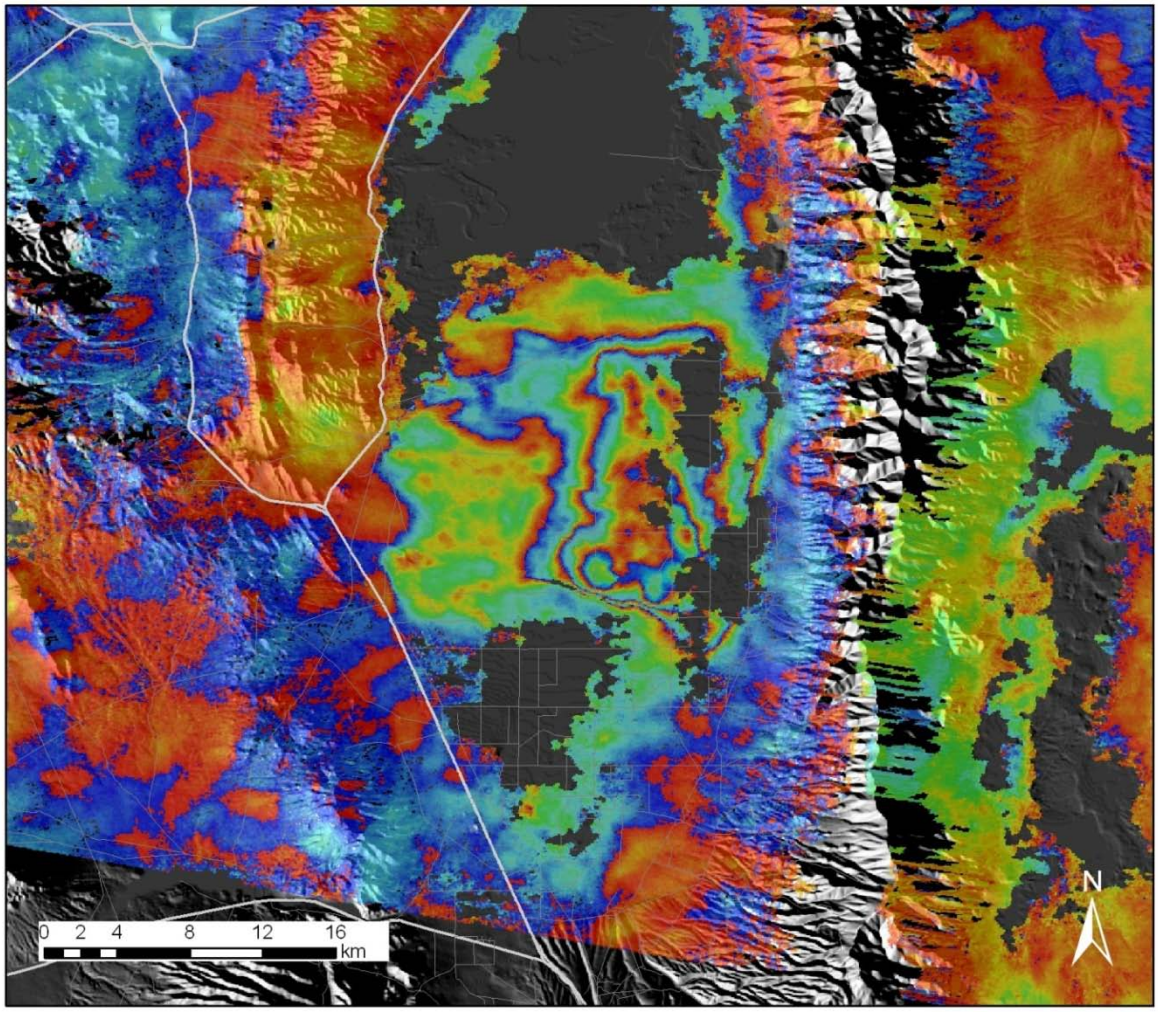

Satellite Type	Master Acquisition Date	Slave Acquisition Date	Perpendicular Baseline (m)
Envisat	11/05/2005	12/30/2006	186
Unwrapped interferogram			

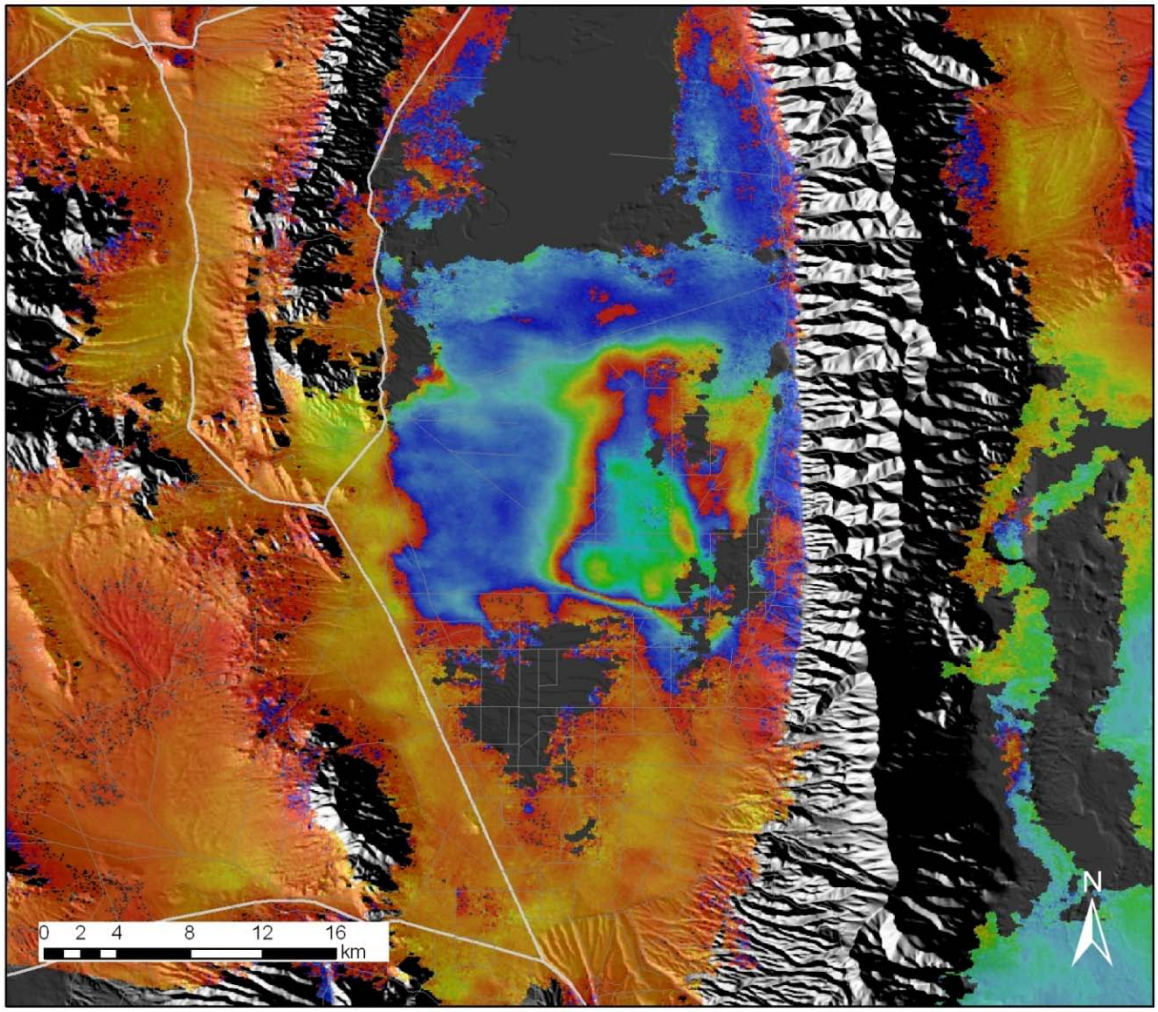

Satellite Type	Master Acquisition Date	Slave Acquisition Date	Perpendicular Baseline (m)
Envisat	09/16/2006	11/25/2006	151
Wrapped interferogram			

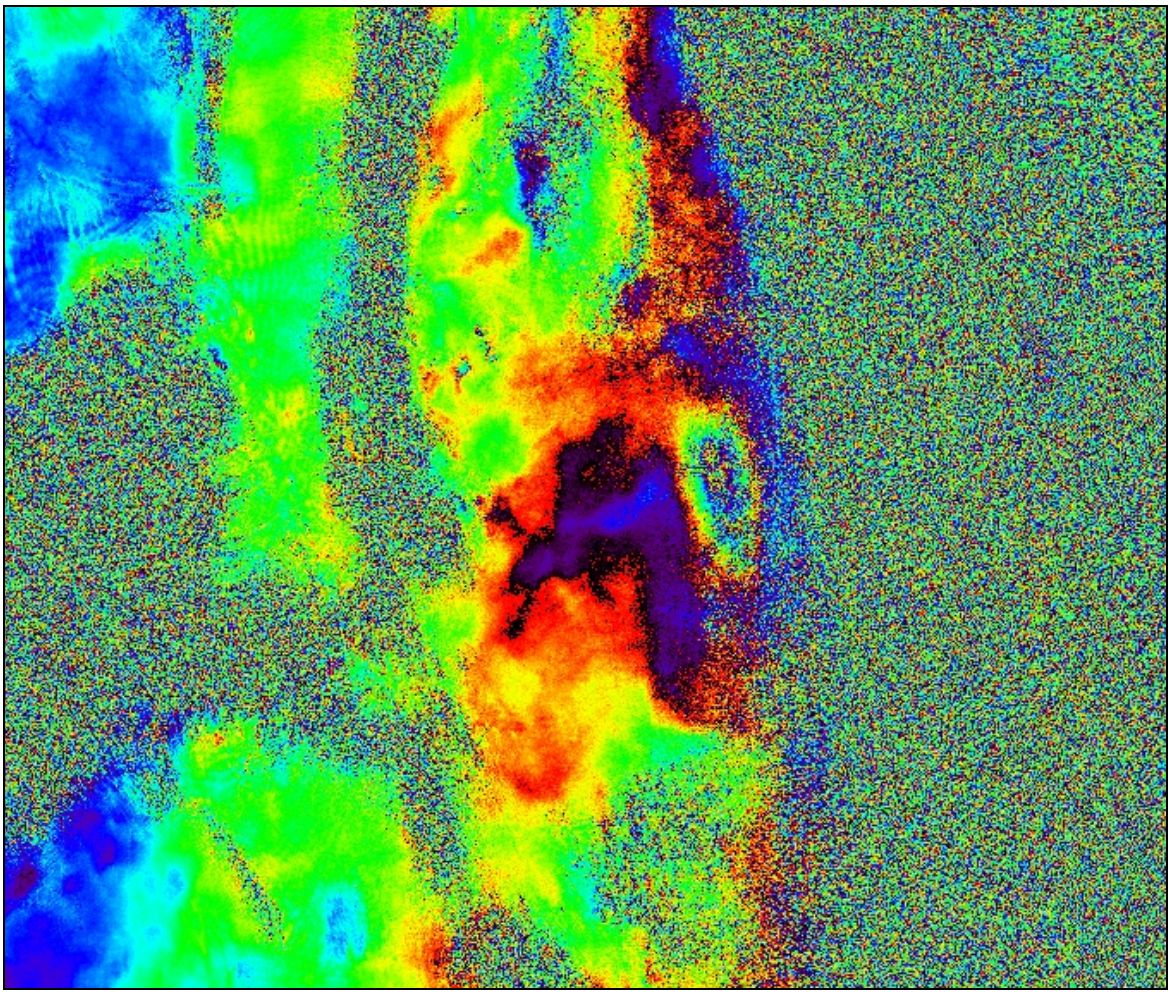

Satellite Type	Master Acquisition Date	Slave Acquisition Date	Perpendicular Baseline (m)
Envisat	11/25/2006	05/19/2007	128
Unwrapped interferogram			

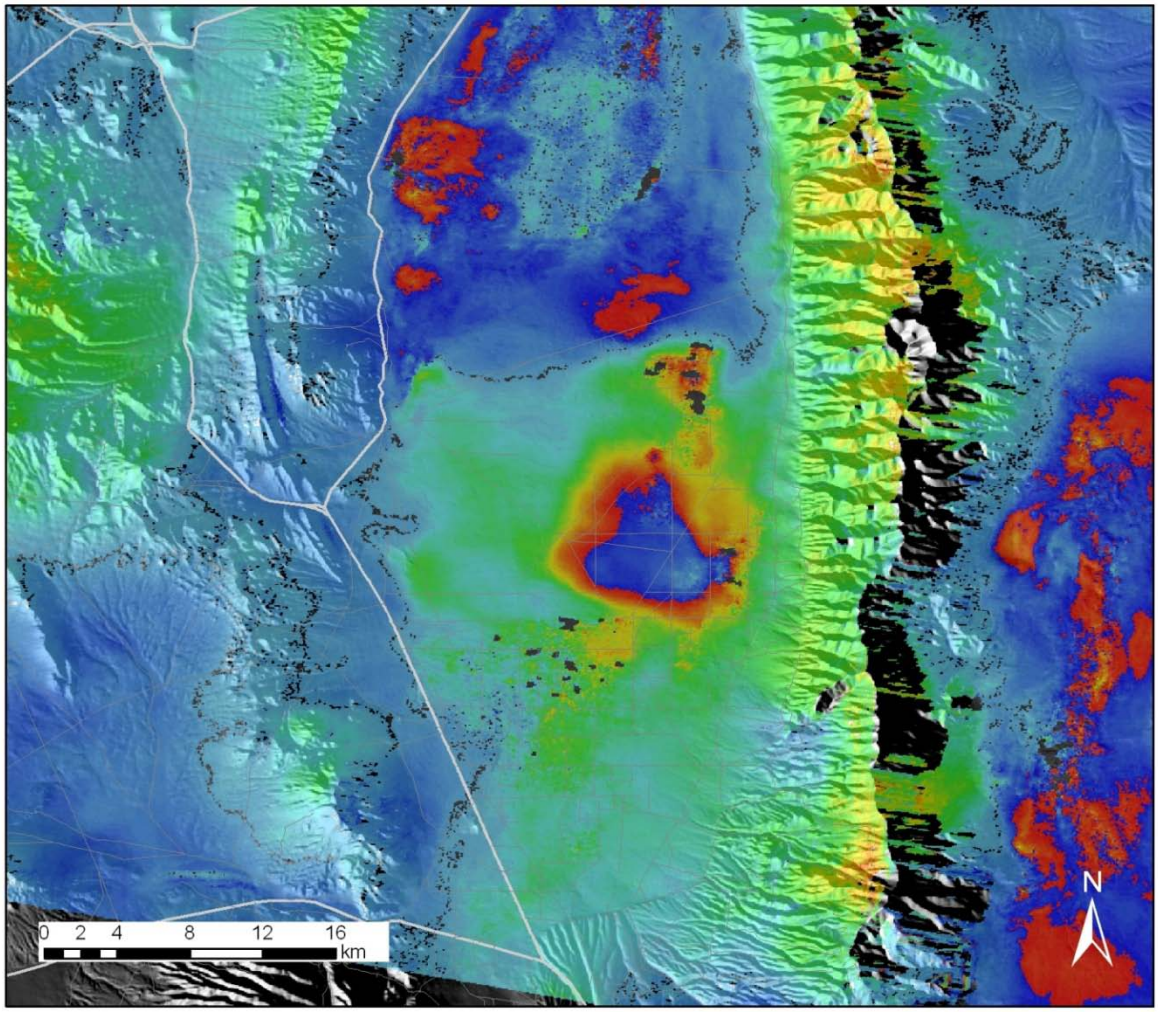

Satellite Type	Master Acquisition Date	Slave Acquisition Date	Perpendicular Baseline (m)
Envisat	11/25/2006	12/15/2007	131
Unwrapped interferogram			

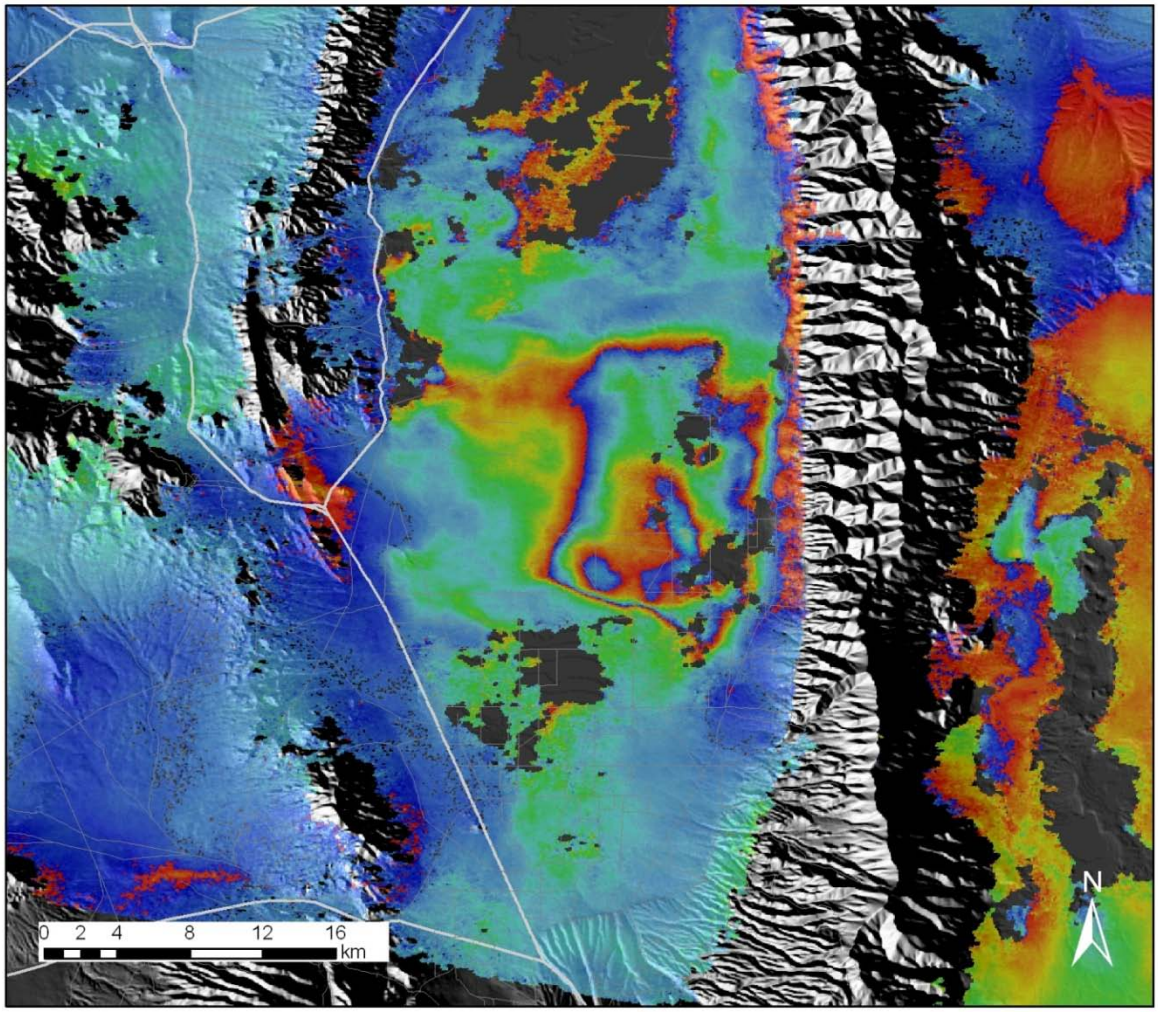

Appendix II

This appendix contains the Microsoft Excel spreadsheet that was used to create the water level elevation plots for seven wells in Chapter 6. Data were recorded in measurement of the depth to the water surface in a well since 1965 or 1966 and the elevation of the water surface was obtained by subtracting the measured length from the elevation of land surface.

Appendix II Selected wells and water level data for Diamond Valley for 1965-2006

Well number	Local well number	Latitude	Longitude	Elevation of land surface (feet)	Date	Depth (feet)	Elevation of water surface (feet)
1	153 N23 E54 29CDDD	39.8383	-115.9120	5820	11/01/65	4.0	5823.0
					11/01/66	4.8	5822.2
					11/01/67	7.7	5819.3
					11/01/68	9.8	5817.2
					11/01/69	7.1	5819.9
					11/01/71	5.7	5821.3
					03/01/77	8.6	5818.4
					11/08/78	15.2	5811.8
					11/01/79	23.4	5803.6
					11/01/80	24.1	5802.9
					11/01/81	31.4	5795.6
					11/09/82	25.5	5801.5
					11/07/83	26.4	5800.6
					11/01/84	28.8	5798.2
					12/03/85	25.6	5801.4
					11/04/86	32.3	5794.7
					11/12/87	33.4	5793.6
					10/17/88	41.5	5785.5
					11/02/89	42.8	5784.2
					03/17/98	30.2	5796.8
					03/08/99	29.6	5797.4
					03/21/00	30.5	5796.5
					03/30/01	31.6	5795.4
					03/28/02	33.4	5793.6
					03/21/03	31.2	5795.8
					03/24/04	36.5	5790.5
					03/16/05	37.5	5789.5
					03/28/06	32.0	5795.0
2	153 N23 E54 30DDDD	39.8238	-115.9117	5827	04/07/66	2.0	5828.0
					04/01/68	5.1	5824.9
					04/23/69	4.9	5825.1
					11/16/71	6.1	5823.9
					11/29/73	5.8	5824.2
					11/03/75	11.1	5818.9
					03/01/76	8.5	5821.5
					03/05/77	10.2	5819.8
					11/08/78	18.4	5811.6
					11/01/79	24.0	5806.0
					11/01/81	36.5	5793.5
					11/09/82	27.7	5802.3
					11/07/83	28.5	5801.5
					11/01/84	20.4	5809.6
					12/03/85	27.0	5803.0
					11/12/87	36.8	5793.2
					10/17/88	45.8	5784.2

Appendix II Selected wells and water level data for Diamond Valley for 1965-2006

Well number	Local well number	Latitude	Longitude	Elevation of land surface (feet)	Date	Depth (feet)	Elevation of water surface (feet)
					11/02/89	43.5	5786.5
					03/27/97	28.0	5802.0
					03/17/98	28.4	5801.6
					03/08/99	27.6	5802.4
					03/21/00	28.2	5801.8
					04/04/01	29.3	5800.7
					03/28/02	31.0	5799.1
					03/21/03	32.2	5797.8
					03/24/04	33.0	5797.0
					03/24/04	33.2	5796.8
					03/16/05	34.0	5796.0
					03/16/05	34.2	5795.8
					03/28/06	32.3	5797.7
3	153 N22 E54 6CCCC	39.8094	-115.9403	5838	04/07/66	8.0	5832.0
					10/01/73	15.0	5825.0
					11/03/75	18.5	5821.5
					11/08/76	20.2	5819.8
					11/14/77	23.1	5816.9
					11/08/78	24.9	5815.1
					11/01/79	33.6	5806.4
					11/04/86	36.9	5803.1
					11/12/87	39.7	5800.3
					10/17/88	47.6	5792.4
					11/03/89	43.9	5796.1
					03/27/97	40.3	5799.7
					03/17/98	40.8	5799.2
					03/08/99	39.0	5801.0
					03/21/00	42.7	5797.3
					04/04/01	43.8	5796.2
					03/28/02	42.1	5797.9
					03/21/03	43.4	5796.6
					03/24/04	44.3	5795.7
					03/16/05	47.0	5793.0
					03/28/06	47.0	5793.1
4	153 N22 E54 18CADD	39.7838	-115.9353	5847	09/23/66	13.0	5834.0
					04/01/68	15.0	5832.0
					04/23/69	14.8	5832.2
					11/16/71	15.2	5831.8
					10/01/73	15.8	5831.2
					11/03/75	24.2	5822.8
					03/01/76	19.4	5827.6
					04/01/77	22.1	5824.9
					04/04/78	24.0	5823.0
					11/01/79	35.8	5811.2

Appendix II Selected wells and water level data for Diamond Valley for 1965-2006

Well number	Local well number	Latitude	Longitude	Elevation of land surface (feet)	Date	Depth (feet)	Elevation of water surface (feet)
					04/17/80	27.8	5819.2
					11/01/81	42.5	5804.5
					11/09/82	38.8	5808.2
					05/01/83	36.8	5810.2
					11/01/84	40.6	5806.4
					12/03/85	39.4	5807.6
					11/04/86	43.5	5803.5
					11/12/87	44.5	5802.5
					10/17/88	54.1	5792.9
					11/03/89	49.5	5797.5
					03/26/97	48.6	5798.4
					03/17/98	49.1	5797.9
					03/08/99	49.0	5798.0
					03/21/00	51.0	5796.0
					03/30/01	51.5	5795.5
					03/28/02	53.3	5793.7
					03/21/03	54.6	5792.4
					03/24/04	56.0	5791.0
					03/24/04	56.2	5790.8
					03/16/05	57.0	5790.0
					03/16/05	57.2	5789.8
					03/28/06	56.9	5790.1
5	153 N22 E54 27CAB	39.7658	-115.8839	5866	09/21/65	17.5	5839.5
					04/07/66	15.5	5841.5
					03/23/67	19.7	5837.3
					03/20/68	21.0	5836.0
					04/22/69	21.3	5835.7
					04/22/70	21.4	5835.6
					04/20/71	22.3	5834.7
					03/03/72	21.0	5836.0
					04/28/73	16.0	5841.0
					05/13/74	23.5	5833.5
					03/14/75	26.2	5830.8
					03/18/76	25.3	5831.7
					03/24/77	29.3	5827.7
					04/12/78	32.7	5824.3
					03/20/79	34.4	5822.7
					03/19/80	37.9	5819.1
					03/20/81	40.1	5817.0
					03/16/82	44.3	5812.7
					03/25/85	39.5	5817.5
					03/27/87	47.6	5809.4
					03/18/88	50.7	5806.3
					05/24/90	57.7	5799.3
					02/25/91	60.1	5796.9

Appendix II Selected wells and water level data for Diamond Valley for 1965-2006

Well number	Local well number	Latitude	Longitude	Elevation of land surface (feet)	Date	Depth (feet)	Elevation of water surface (feet)
					03/20/92	59.7	5797.3
					04/14/93	61.8	5795.2
					04/01/94	63.7	5793.3
					03/29/95	65.8	5791.2
					03/24/97	65.0	5792.0
					03/24/97	65.4	5791.6
					04/13/04	79.0	5778.0
					04/08/05	81.7	5775.3
					03/07/06	83.2	5773.8
6	153 N22 E54 28DCCC	39.7516	-115.8973	5860	04/07/66	14.6	5845.4
					11/01/67	28.7	5831.3
					04/01/68	20.8	5839.2
					09/12/69	22.9	5837.1
					11/15/71	21.8	5838.2
					02/24/72	20.8	5839.2
					11/29/73	24.1	5835.9
					03/13/74	25.6	5834.4
					11/06/75	25.8	5834.2
					04/01/76	24.9	5835.1
					03/05/77	28.8	5831.2
					04/04/78	33.6	5826.4
					11/07/79	44.7	5815.3
					11/21/80	46.3	5813.7
					11/09/82	48.9	5811.1
					04/01/83	45.3	5814.7
					03/26/97	61.2	5798.9
					03/17/98	62.6	5797.4
					03/08/99	58.9	5801.1
					03/21/00	64.1	5795.9
					03/30/01	65.5	5794.5
					03/21/03	73.7	5786.3
					03/24/04	80.9	5779.1
					03/16/05	78.7	5781.3
					03/28/06	76.4	5783.7
7	153 N21H E54 32DCCC	39.7241	-115.9159	5873	04/01/65	23.2	5849.8
					08/27/68	33.2	5839.8
					08/12/69	29.9	5843.1
					03/11/74	35.0	5838.0
					11/06/75	35.7	5837.3
					11/08/76	38.5	5834.5
					11/16/77	46.2	5826.8
					11/14/78	49.2	5823.8
					11/07/79	49.2	5823.8
					11/21/80	49.2	5823.8

Appendix II Selected wells and water level data for Diamond Valley for 1965-2006

Well number	Local well number	Latitude	Longitude	Elevation of land surface (feet)	Date	Depth (feet)	Elevation of water surface (feet)
					11/09/82	56.3	5816.7
					11/07/83	58.0	5815.0
					11/01/84	60.0	5813.0
					03/26/97	75.6	5797.5
					03/17/98	77.0	5796.0
					03/08/99	77.8	5795.2
					03/21/00	80.1	5792.9
					03/30/01	82.3	5790.7
					03/28/02	85.2	5787.9
					03/21/03	87.3	5785.7
					03/18/04	89.0	5784.0
					03/15/05	91.1	5781.9
					03/28/06	91.7	5781.3

Appendix III

This appendix contains the Microsoft Excel spreadsheet that was used to complete the subsurface lithologic distribution model in Chapter 6. A total of 34 driller's logs data were analyzed into three lithologic groups; sand and gravel, clay and a mixture of clay, sand and gravel. The thickness of each material was taken to determine the total volume of a group, and the relative percentages for the whole log were calculated.

Appendix III. Selected driller's logs for wells in Diamond Valley, Nevada.

Log number	Year drilled	Depth (feet)	Material	Thickness (feet)	Depth (feet)
76989	06/01/99	356	top soil	2	2
			sand & gravel	39	41
			clay	9	50
			sand & gravel	11	61
			clay	58	119
			black sand	7	126
			clay	14	140
			sand & gravel	8	148
			clay	4	152
			sand & gravel	4	156
			clay	5	161
			sand & gravel	16	177
			clay	6	183
			sand & gravel	7	190
			clay	42	232
			sand & gravel	16	248
			clay	32	280
			sand & gravel	7	287
			clay & gravel	5	292
			clay	10	302
			clay & some gravel	17	319
			sand & gravel	12	331
			clay	4	335
			sand & gravel	6	341
			clay	4	345
			sand & gravel	3	348
			clay	4	352
			sand & gravel	4	355
			clay	9	365
6376	02/01/62	184	top soil	4	4
			sand & gravel	16	20
			sand & gravel	40	60
			gravel & clay	10	70
			clay	65	135
			clay & coarse sand	8	143
			coarse sand	2	145
			clay & coarse sand	3	148
			coarse sand	10	158
			clay & coarse sand	2	160
			good gravel	15	175
			clay	2	177
			good gravel	6	183
			clay	1	184

Appendix III. Selected driller's logs for wells in Diamond Valley, Nevada.

Log number	Year drilled	Depth (feet)	Material	Thickness (feet)	Depth (feet)
13730	11/10/73	288	top soil	2	2
			sand & gravel	48	50
			clay	32	82
			fine sand	16	98
			sand & gravel	14	112
			fine sand & clay	34	146
			gravel	22	168
			clay & gravel	10	178
			sand	6	184
			clay	10	194
			gravel	3	197
			clay	12	209
			coarse sand	7	216
			sand & clay	8	224
			coarse sand	7	231
			sand & clay	15	246
			gravel	6	252
			clay	8	260
			gravel	3	263
			clay	7	270
			cemented gravel	2	272
			sand & gravel	5	277
			clay & sand	7	284
			cemented gravel	4	288
55917	12/30/95	375	top soil	2	2
			sand & gravel	29	31
			clay	44	75
			sand & gravel	6	81
			clay	9	90
			sand & gravel	29	119
			black clay	14	133
			black sand & gravel	19	152
			clay	1	153
			sand & gravel	19	172
			clay	7	179
			sand & gravel	24	203
			clay	21	224
			sand & gravel	15	239
			clay	3	242
			sand & gravel	4	245
			clay	3	249
			sand & gravel	15	264
			clay	66	330
			sand & gravel	4	334

Appendix III. Selected driller's logs for wells in Diamond Valley, Nevada.

Log number	Year drilled	Depth (feet)	Material	Thickness (feet)	Depth (feet)
			clay	18	352
			sand & gravel	12	364
			clay	11	375
84154	05/26/01	337	sand	10	10
			sand & gravel	9	19
			clay	23	42
			sand & gravel	6	48
			clay	8	56
			sand & gravel	18	74
			clay	6	80
			sand & gravel	16	96
			clay	8	102
			black clay & sand	16	118
			sand & gravel	14	132
			clay with sand & gravel	8	140
			sand & gravel	5	145
			clay	3	148
			sand & gravel	48	196
			clay	2	198
			sand & gravel with clay -----	139	337
16544	06/04/77	412	top soil	2	
			sand & gravel	48	
			clay	50	
			sand & gravel clay layers	96	
			clay	113	
			sand	130	
			clay	134	
			sand	166	
			clay	172	
			fine gray sand	175	
			sand & gravel	183	
			clay	185	
			sand & gravel	187	
			fine brown sand	195	
			fine black sand	201	
			brown sand & gravel	214	
			gravel	226	
			clay	228	
			gravel	243	
			clay	254	
			gravel	260	
			clay	272	
			sand & gravel	285	

Appendix III. Selected driller's logs for wells in Diamond Valley, Nevada.

Log number	Year drilled	Depth (feet)	Material	Thickness (feet)	Depth (feet)
			clay	304	
			gravel	308	
			clay	313	
			cemented clay & gravel	315	
			soft clay	317	
			sand & gravel	334	
			clay	336	
			gravel	343	
			clay	345	
			sand	350	
			clay	360	
			gravel	368	
			clay	370	
			gravel	372	
			clay	381	
			gravel	394	
			clay	398	
			gravel	400	
			clay	405	
			gravel	407	
			clay	412	
93672	07/11/04	400	gravel	65	65
			clay	38	103
			fine black sand	4	107
			clay	15	122
			fine sand	9	131
			clay with sand	1	132
			sand	3	135
			clay	1	136
			fine sand	4	140
			clay	1	141
			gravel	3	144
			brown silt	13	157
			gravel	6	163
			clay	1	164
			fine sand & gravel	9	173
			fine black sand	7	180
			clay	3	183
			fine black sand	11	194
			gray clay	12	206
			gravel	14	220
			clay	2	222
			gravel	10	232
			brown clay	3	235

Appendix III. Selected driller's logs for wells in Diamond Valley, Nevada.

Log number	Year drilled	Depth (feet)	Material	Thickness (feet)	Depth (feet)
			fine brown sand	1	236
			brown clay	24	260
			clay & gravel	1	261
			clay	14	275
			gravel	5	280
			clay with gravel	3	283
			gravel	18	301
			clay	2	303
			clay with gravel	2	305
			clay	16	321
			gravel	4	325
			clay	8	333
			clay with gravel	7	340
			gravel	2	342
			clay with gravel	21	363
			gravel	5	368
			clay	32	400
98067	07/05/05	485	sand & gravel	17	17
			bed rock	3	20
			sand & gravel	16	36
			clay	4	40
			clay & sand	5	45
			gray clay	20	65
			gravel large	3	68
			gray clay	2	70
			gravel	20	90
			gray clay	2	92
			gravel	6	98
			gray gravel & clay	2	100
			brown clay	4	104
			gravel large	36	140
			gravel large	27	167
			brown clay & gravel	4	171
			gravel large	9	180
			gravel & clay	10	190
			gravel	7	197
			brown clay	11	208
			gravel large	10	218
			brown clay	2	220
			gravel	8	228
			clay	8	236
			gravel	4	240
			brown clay	80	320
			brown clay	30	350

Appendix III. Selected driller's logs for wells in Diamond Valley, Nevada.

Log number	Year drilled	Depth (feet)	Material	Thickness (feet)	Depth (feet)
			clay & gravel	4	354
			clay	21	375
			gravel & clay	2	377
			clay & gravel	2	379
			clay	6	385
			gravel	5	390
			clay	8	398
			gravel	2	400
			clay	7	407
			clay & gravel	1	408
			clay	10	418
			gravel	3	421
			clay	9	430
			clay hard	2	432
			clay soft	15	447
			gravel & clay	3	450
			clay	5	455
			clay soft	30	485
94521	07/13/04	285	brown sand	27	27
			gravel	4	31
			brown clay	52	83
			gravel	12	95
			fine gray sand	7	102
			gray clay	15	117
			gravel	23	140
			cemented gravel	145	285
72097	06/03/98	339	top soil	2	2
			sand & gravel	5	7
			clay	43	50
			sand & gravel	10	60
			clay	64	124
			sand & gravel	14	138
			clay	2	140
			sand & gravel	3	143
			clay	14	157
			sand & gravel	7	164
			clay	53	217
			sand & gravel	3	220
			clay	11	231
			sand & gravel	3	234
			clay	1	245
			sand & gravel	1	246
			sand gravel & clay	14	260

Appendix III. Selected driller's logs for wells in Diamond Valley, Nevada.

Log number	Year drilled	Depth (feet)	Material	Thickness (feet)	Depth (feet)
			clay	4	264
			sand & gravel	24	288
			clay & gravel	4	292
			cemented sand & gravel w/ sandstone and clay layers	47	339
7324	07/31/63	240	top soil	4	4
			gravel & clay	11	15
			cobble stones & clay	58	73
			fine gravel	7	80
			boulders	50	130
			solid rock	8	138
			rocks & free gravel	5	143
			clay	1	144
			boulders	12	156
			coarse gravel	17	173
			clay	1	174
			gravel	38	212
			clay	2	214
			boulders	21	235
			clay & gravel	5	240
6635	06/15/62	200	sand & gravel w/ large cobbles	37	37
			clay	3	40
			sand & gravel w/ large cobbles	30	70
			clay with gravel	2	72
			fine gravel	7	79
			clay lenses with smal gravel	11	90
			clay with small gravel	10	100
			small gravel	10	110
			clay	2	112
			gravel& large cobbles	76	188
			clay with cemented gravel	12	200
88354	08/25/02	403	gravel	58	58
			cobble stone	25	83
			clay with gravel	11	94
			cobble stone	13	107
			cobble with clay streaks	13	120
			cobble stone	24	144
			gravel with clay	30	174
			cemented gravel	41	215
			clay with gravel	8	223
			gravel	4	227
			cenmented gravel	20	247
			cemented gravel w/ clay	17	264

Appendix III. Selected driller's logs for wells in Diamond Valley, Nevada.

Log number	Year drilled	Depth (feet)	Material	Thickness (feet)	Depth (feet)
			streaks		
			hard cemented gravel	53	317
			cemented gravel w/ clay streaks	5	322
			brown clay	2	324
			gravel & cobble stone	11	335
			cemented gravel	8	343
			gravel	2	345
			cemented gravel med hard	15	360
			brown clay	7	367
			gravel with clay	13	380
			gravel	12	392
			cemented gravel	11	403
9134	03/30/64	260	top soil	2	2
			sand & gravel	28	30
			black clay	27	57
			black gravel	3	60
			clay	5	65
			clay & gravel	5	70
			clay	44	114
			fine sand	6	120
			clay	8	128
			coarse sand	12	140
			clay & sand	1	141
			coarse sand	4	145
			clay	2	147
			coarse sand	1	148
			clay	2	150
			clay & sand	10	160
			clay	64	224
			clay & gravel	3	227
			clay	13	240
			clay & gravel	2	242
			cemented gravel	3	245
			gravel	3	248
			hard clay & gravel	2	250
			hard clay & gravel	8	258
			cemented gravel	2	260
103695	05/19/07	475	sand	25	25
			sand & rock	5	30
			clay & gravel	6	36
			sand & rock	19	55
			sand & hard rock	15	70
			cemented gravel	50	120

Appendix III. Selected driller's logs for wells in Diamond Valley, Nevada.

Log number	Year drilled	Depth (feet)	Material	Thickness (feet)	Depth (feet)
			w/clay hard rock	18	138
			rock hard	60	198
			gravel & clay	46	244
			gravel & stones	14	258
			rock hard	7	265
			rock hard	7	272
			w/sand cobble large	4	276
			quartzite	26	302
			w/clay rock hard	8	310
			w/clay sand & rock	22	332
			w/clay gravel & sand	6	338
			w/gravel sand & rock	14	352
			w/clay rock hard	22	374
			rock hard	46	420
			rock hard	6	426
			w/clay sand & rock	5	431
			rock hard	17	448
			w/rock sand clay gravel	7	455
			w/rock gravel clay sand	20	475
87979	05/18/02	405	top soil	10	10
			gravel	35	45
			brown clay	18	63
			gravel	6	69
			clay	5	74
			gravel	16	90
			cobble stone & gravel	54	144
			cemented gravel & clay shavings	76	220
			cemented gravel	185	405
103127	01/11/07	455	sand & gravel	22	22
			black sand & clay	4	26
			black clay	98	124
			black sand & clay	2	126
			gray clay	11	137
			w/sand gravel	3	140
			gray clay	40	180
			gray clay	10	190
			w/sand clay	25	215
			sand	7	222
			gray hard clay	13	235
			gray clay	13	248
			brown w/gravel clay	5	253
			brown clay	27	280

Appendix III. Selected driller's logs for wells in Diamond Valley, Nevada.

Log number	Year drilled	Depth (feet)	Material	Thickness (feet)	Depth (feet)
			w/clay gravel	2	282
			gravel large	5	287
			w/ gravel clay	8	295
			gravel large	13	308
			brown w/ gravel clay	4	312
			gravel large	3	315
			brown clay	15	330
			w/gravel clay	4	334
			gravel large	12	346
			brown clay	17	363
			brown gravel & clay	5	368
			gravel large	8	376
			brown w/gravel clay	4	380
			w/clay gravel	13	393
			brown clay	4	397
			gravel large	8	405
			clay & gravel	5	410
			gravel	5	415
			clay & gravel	3	418
			brown clay	37	455
6961	04/07/62	240	sand & gravel	10	10
			sand & gravel	10	20
			clay	70	90
			clay & coase sand	10	100
			clay	32	132
			fine sand	2	134
			clay	2	136
			coarse sand	14	150
			clay	1	151
			coarse sand & clay	4	155
			clay	3	158
			coarse sand & clay	3	161
			coarse sand	10	171
			clay	3	174
			fine sand	5	179
			clay	46	225
			sand	15	240
7975	06/29/64	250	top soil	3	3
			gravel	17	20
			sand & clay	10	30
			clay	25	55
			clay & black gravel	2	57
			black gravel	4	61

Appendix III. Selected driller's logs for wells in Diamond Valley, Nevada.

Log number	Year drilled	Depth (feet)	Material	Thickness (feet)	Depth (feet)
			clay	14	75
			coarse sand	4	79
			clay & gravel layers	7	86
			black gravel	1	87
			clay	1	88
			coarse sand	4	92
			clay	4	96
			clay & gravel	4	100
			clay & gravel layers	3	103
			coarse sand	7	110
			clay & gravel	5	115
			clay	24	139
			coarse sand	6	145
			clay	1	146
			gravel	2	148
			clay & gravel	4	152
			clay & sand	1	153
			sand	8	161
			clay	2	163
			gravel	7	170
			clay	2	172
			sand & gravel	3	175
			clay & gravel	2	177
			clay	1	178
			sand	5	183
			clay & sand	3	186
			clay	2	188
			sand & gravel	4	192
			clay	40	232
			sand	6	238
			clay	2	240
			sand	4	244
			clay	2	246
			sand	4	250
35013	11/07/90	500	brown sand	15	15
			black sand	20	35
			black clay	25	60
			black sand & gray clay	5	65
			grey clay	15	80
			water bearing gravel	5	85
			gray clay	65	150
			water sand & small gravel	20	170
			grey clay & black sand	60	230
			black water sand	10	240

Appendix III. Selected driller's logs for wells in Diamond Valley, Nevada.

Log number	Year drilled	Depth (feet)	Material	Thickness (feet)	Depth (feet)
			grey clay	50	290
			light brown clay	80	370
			small water bearing gravel	30	400
			light brown clay	100	500
18030	03/17/78	380	top soil	4	4
			blue sand	13	17
			fine blue sand	13	30
			black clay	31	61
			black volcanic sand	4	65
			sandy blue clay	15	80
			sandy blue clay & sand	20	100
			sandy blue clay	35	135
			green sand	6	141
			green clay	14	155
			coarse sand	2	157
			green clay	18	175
			sand	5	180
			gray clay	5	185
			coarse sand	12	197
			green clay	33	230
			fine sand	11	241
			gray clay	14	255
			fine sand	5	260
			green clay	20	280
			green and grey clay	30	310
			brown clay	35	345
			brown clay & gravel	5	350
			grey clay	30	380
4433	07/18/58	222	sand & gravel	25	25
			sand & clay	28	53
			sand	9	62
			clay	4	66
			sand & gravel	4	70
			blue clay	25	95
			sandstone (soft)	10	105
			sandy clay	10	115
			sandstone	5	120
			clay	18	138
			sandstone	7	145
			clay	5	150
			sandy clay	16	166
			sand	4	170
			clay	7	177

Appendix III. Selected driller's logs for wells in Diamond Valley, Nevada.

Log number	Year drilled	Depth (feet)	Material	Thickness (feet)	Depth (feet)
			sand	13	190
			clay	27	217
103709	04/05/07	295	sand	30	30
			gray clay	2	32
			black fine sand	8	40
			black clay	15	55
			black sand & clay	20	75
			gravel	3	78
			grayish brown clay	10	88
			black fine sand	15	103
			gray clay	2	105
			sand & gravel	2	107
			clay & gravel	5	112
			sand & clay	13	125
			black silt	9	134
			clay & gravel	4	138
			gravel	8	146
			fine sand	2	148
			sand	12	160
			gray clay	9	169
			fine sand	9	178
			gravel & clay	2	180
			fine sand	10	190
			gray clay & sand	17	207
			fine sand	11	218
			gray clay	2	220
			fine sand	13	233
			sand	27	260
			clay	35	295
91852	05/08/03	285	gravel	10	10
			brown clay	13	23
			gray silt	27	50
			black silty clay	5	55
			black clay	9	64
			gravel	5	69
			gray clay	36	105
			brown clay	7	112
			gray clay & gravel	3	115
			gray clay	30	145
			brown sand	7	152
			gravel	13	165
			gray clay	10	175
			black sand	4	179

Appendix III. Selected driller's logs for wells in Diamond Valley, Nevada.

Log number	Year drilled	Depth (feet)	Material	Thickness (feet)	Depth (feet)
			gray clay	5	184
			brown sand	6	190
			gray clay	21	211
			black sand	4	215
			gray clay	19	234
			black sand	26	260
			brown clay	25	285
14489	12/12/74	310	top soil	3	3
			gravel	5	8
			clay & gravel	1	9
			sand	2	11
			cemented sand & sand	11	22
			black sand & gray clay	26	48
			black clay	12	60
			coarse black sand & clay	11	71
			gray clay	13	84
			brown clay	7	91
			gray clay	35	126
			black coarse sand and clay	5	131
			black coarse sand	3	134
			fine black sand & gray clay	14	148
			coarse black sand & gray clay	4	152
			gray clay and gravel	18	170
			fine black sand	10	180
			black & gray clay	9	189
			gray clay	29	218
			coarse sand & hard clay	3	221
			gray clay	3	224
			clay & gravel	5	229
			coarse sand & fine gravel	5	234
			clay & gravel	25	259
			gravel	2	261
			clay	49	310
7423	10/08/63	250	top soil	2	2
			sand & gravel	18	20
			sand	10	30
			clay	36	66
			clay & gravel	4	70
			clay	18	88
			black sand	2	90
			clay	33	123
			fine sand	2	125
			sand & clay	4	129

Appendix III. Selected driller's logs for wells in Diamond Valley, Nevada.

Log number	Year drilled	Depth (feet)	Material	Thickness (feet)	Depth (feet)
			coarse sand	1	130
			coarse sand	10	140
			fine sand & clay	5	145
			clay	5	150
			clay & gravel	3	153
			coarse sand	1	154
			sand & clay	2	156
			clay	10	166
			coarse sand	2	168
			clay	3	171
			fine sand	6	177
			clay	23	200
			fine sand	2	202
			fine sand & clay	2	204
			fine sand	1	205
			clay	5	210
			fine sand & clay	4	214
			clay	9	223
			sand & clay layers	5	228
			clay	2	230
			gravel	5	235
			clay	15	250
16441	04/01/77	300	top soil	5	5
			sandy clay	15	20
			sandy clay	5	25
			clay & sandy clay	38	63
			hard sand & gravel	3	66
			clay & sand	44	110
			hard sand & gravel	5	115
			sandy clay	17	132
			sandstone	14	146
			sandy clay & clay	28	174
			cemented sand & gravel	4	178
			sand & gravel	7	185
			clay & gravel	25	210
			cemented sand & gravel	5	215
			sand & gravel	5	220
			cemented sand & gravel	5	225
			sand & gravel	5	230
			cemented sand & gravel	40	270
			gravel & clay	15	285
			large gravel	5	290
			cemented sand & gravel	10	300

Appendix III. Selected driller's logs for wells in Diamond Valley, Nevada.

Log number	Year drilled	Depth (feet)	Material	Thickness (feet)	Depth (feet)
15651	04/19/76	299	top soil	4	4
			gravel & sand	9	13
			clay	100	113
			blue sand	4	117
			clay	40	157
			gray sand	2	159
			green clay	2	161
			fine black sand & clay	6	167
			green clay	4	171
			clay	46	217
			gravel & hardpan	4	221
			hardpan	6	227
			gravel	3	230
			gravel & hardpan	6	236
			clay & gravel	4	240
			gravel & cobbles	16	256
			hardpan	2	258
			gravel	8	266
			gravel & hardpan	5	271
			fine gravel	13	284
			hardpan	1	285
			coarse gravel	2	287
			cemented gravel	6	293
			hard brown gravel	6	299
7834	05/06/64	245	top soil	2	2
			hard pan	2	4
			sand & gravel	13	17
			black clay	33	50
			clay	25	75
			coarse sand	1	76
			clay	65	141
			fine sand	9	150
			clay	20	170
			fine sand	2	172
			clay	3	175
			fine sand	2	177
			sand & clay	31	208
			fine sand	22	230
			sand & gravel	15	245
7861	05/21/64	320	silt	1	1
			clay	2	3
			gravel	2	5
			clay	3	8

Appendix III. Selected driller's logs for wells in Diamond Valley, Nevada.

Log number	Year drilled	Depth (feet)	Material	Thickness (feet)	Depth (feet)
			clay & gravel	4	12
			sand & gravel	6	18
			black sand	8	26
			soft black clay	46	72
			gravel	3	75
			blue clay	4	79
			sand & gravel	5	84
			dark shale	4	88
			light shale	22	110
			hard gray shale	8	118
			soft gray shale	27	145
			sand & gravel	6	151
			gray shale	9	160
			sand & gravel	6	166
			coarse sand	12	178
			gray shale	11	189
20620	12/06/79	403	top soil	2	2
			sand & gravel	11	13
			clay	118	131
			fine black sand	7	138
			clay	20	158
			black gravel & fine black sand	8	166
			clay	94	260
			black sand & gravel	6	266
			clay	30	296
			sand & gravel	5	301
			clay	6	307
			gravel & clay traces	9	316
			clay	5	321
			clay & gravel	19	340
			gravel & clay traces	8	348
			clay	10	358
			sand & gravel	13	371
			clay & rocks	4	375
			sand & gravel	7	382
			cemented gravel	3	385
			clay	18	403
77031	04/13/99	440	top soil	2	2
			sand & gravel	9	11
			black clay & sand	136	147
			black fine sand	3	150
			sand & clay layers	35	185
			black fine sand	3	188

Appendix III. Selected driller's logs for wells in Diamond Valley, Nevada.

Log number	Year drilled	Depth (feet)	Material	Thickness (feet)	Depth (feet)
			clay	3	191
			sand	2	193
			clay	23	216
			black sand	6	222
			clay	3	225
			black sand	12	237
			clay	8	245
			sand	11	256
			clay	6	262
			sand	3	265
			sandy clay	80	345
			sand	2	347
			clay	8	355
			sand	6	361
			hard brown sand	17	378
			clay	4	382
			brown sand	12	394
			clay	10	404
			sand & some clay	12	416
			clay	6	422
			sand	14	236
			clay	4	440
27428	06/21/86	480	top soil	2	2
			sand & gravel	13	15
			green clay	2	17
			black silt	7	24
			black silty clay	26	50
			green clay	5	55
			green & black clay	14	69
			green clay with sand stringers	12	81
			green clay	43	124
			fine sand	9	133
			green clay	12	145
			fine sand	8	153
			green clay	4	157
			coarse sand	8	165
			green clay	13	178
			fine sand	12	190
			green clay	23	312
			fine sand	3	216
			green clay	5	221
			fine sand	10	231
			green clay	79	310
			coarse sand	3	313

Appendix III. Selected driller's logs for wells in Diamond Valley, Nevada.

Log number	Year drilled	Depth (feet)	Material	Thickness (feet)	Depth (feet)
			green clay	37	350
			sand with clay	5	355
			brown clay	3	358
			coarse sand	10	368
			brown clay	12	380
			coarse sand	7	387
			brown & white clay	14	401
			coarse sand	10	411
			brown & white clay	6	417
			coarse sand	13	430
			brown & white clay	13	443
			coarse sand	2	445
			brown & white clay	10	455
			coarse sand	3	458
			white clay	10	468
			coarse sand	7	475
			brown & white clay	5	480
29954	03/12/88	503	top soil	4	4
			sand & gravel	17	21
			black clay	49	70
			grey clay	7	77
			green clay	55	132
			green sand	19	151
			green clay	8	159
			sand & gravel	6	165
			clay	13	178
			sand & gravel	5	183
			green clay	39	222
			sand & gravel	14	236
			clay	5	241
			sand & gravel	6	247
			clay	11	258
			sand & gravel	4	262
			clay	47	309
			sand & gravel	7	316
			clay	30	346
			sand & gravel	5	351
			clay	20	371
			sand & gravel	7	378
			clay	8	386
			sand & gravel	8	394
			clay	34	428
			sand & gravel	5	433
			clay	38	471

Appendix III. Selected driller's logs for wells in Diamond Valley, Nevada.

Log number	Year drilled	Depth (feet)	Material	Thickness (feet)	Depth (feet)
			sand & gravel	5	476
			clay	27	503